Stretching and Breaking Symmetry of the Persistent Spin Helix in Quantum Transport

Inauguraldissertation

zur

Erlangung der Würde eines Doktors der Philosophie

vorgelegt der

Philosophisch-Naturwissenschaftlichen Fakultät

der Universität Basel

von

Pirmin Jonas Weigele

aus Deutschland

Basel, 2017

Genehmigt von der Philosophisch-Naturwissenschaftlichen Fakultät auf Antrag von

Prof. Dr. D. M. Zumbühl

Prof. Dr. Th. Schäpers

Prof. Dr. J. Schliemann

Basel, den 14.11.2017

Prof. Dr. M. Spiess

Dekan

The first principle is that you must not fool yourself - and you are the easiest person to fool

Richard Feynman, *Surely You're Joking, Mr. Feynman!*

Contents

Contents **i**

1 Introduction **5**

1.1 Thesis Outline 7

2 Background **9**

2.1 Two-dimensional Electron Gas in GaAs Quantum Wells 9

2.1.1 Transport Properties 12

2.1.2 Scattering Mechanisms 13

2.2 Spin Orbit Interaction 16

2.2.1 Dresselhaus and Rashba Spin Orbit Coupling 18

2.2.2 The Persistent Spin Helix Regime 22

2.2.3 Spin Relaxation and Dephasing 24

2.2.4 Spin Orbit Parameters 26

2.3 Localization and Magnetoconductivity 28

2.3.1 Weak Localization 28

2.3.2 Weak Antilocalization 30

2.4 Magnetoconductivity: The Last 30 Years 33

2.4.1 The Diffusive Approximation $B_{\mathrm{SO}}, B_{\mathrm{z}} \ll B_{\mathrm{tr}}$ 35

2.4.2 Beyond the Diffusive Approximations, $B_{\mathrm{SO}} \gg B_{\mathrm{tr}}$ 40

2.4.3 Summary 44

3 Stretchable Persistent Spin Helices in GaAs Quantum Wells 47

3.1 Abstract . . . 48

3.2 Introduction . . . 49

3.3 Stretchable Persistent Spin Helices . . . 49

3.3.1 Controlling the Rashba Coupling α . . . 52

3.3.2 Linear & Cubic Dresselhaus Terms in 2D . . . 52

3.3.3 Detection Scheme for Matched SO Couplings . . . 55

3.3.4 Continuous Locking $\alpha = \beta$ . . . 55

3.3.5 Dresselhaus Regime . . . 58

3.3.6 Diverging Spin-Orbit Lengths . . . 60

3.4 Final Remarks and Outlook . . . 62

3.4.1 Acknowledgements . . . 63

3.5 Appendix: Materials and Methods . . . 63

3.6 Supplementary Information . . . 65

3.6.1 Wafer Structure: Details . . . 65

3.6.2 Temperature Dependence . . . 67

3.6.3 Numerical Simulations . . . 68

3.6.4 Gate Voltages and Contours of Constant Density . . . 75

3.6.5 Estimate of the Error Bars in the Rashba Coupling due to the Uncertainties in Input Parameters . . . 76

3.6.6 Interface Dresselhaus and Random Rashba SO Couplings . . . 79

3.6.7 Effective Spin-Orbit Magnetic Field . . . 82

3.6.8 Diffusive Spin-Orbit Time and Length . . . 85

3.6.9 Shubnikov-de Haas Oscillations . . . 89

4 Symmetry Breaking of the Persistent Spin Helix in Quantum Transport 93

4.1 Abstract . . . 94

4.2 Introduction . . . 94

4.3 Theory of Quantum Corrections to Conductivity . . . 96

4.4 Experiment . . . 103

4.4.1 Control of Spin Orbit Parameters . . . 103

4.4.2 Evaluation Procedure . . . 105

4.4.3 Determination of the SO Parameters . . . 110

4.5 Conclusion . . . 112

4.5.1 Acknowledgement . . . 113

4.5.2 Author Contributions . . . 114

4.6 Appendix: Materials and Methods . . . 114

4.6.1 Formalism to calculate quantum corrections . . . 114

4.6.2 GaAs quantum well materials . . . 119

4.6.3 Measurement Technique . . . 119

4.6.4 Symmetry Point Determination and Value of B_{SO3} . . . 120

4.6.5 Fit Mask . . . 120

4.7 Supplementary Information . . . 120

4.7.1 Calculation of the Quantum Corrections . . . 120

4.7.2 Quantum Corrections in Presence of a Magnetic Field . . . 124

4.7.3 Full Account of Data . . . 130

4.7.4 Details on evaluating B_{SO-} and B_{SO3} . . . 139

5 Conclusion and Outlook 143

References **147**

Curriculum Vitae **160**

Abstract

As a result of relativistic transformation, electrons moving through an electric field, experience an effective magnetic field, the spin orbit (SO) field, whose direction depends on the momentum and couples to the electron spin. The SO interaction has become a versatile resource in fundamental semiconductor research and is at the heart of semiconductor spintronics. In two dimensional zinc blende structures, the Rashba and Dresselhaus SO field, are the two dominant contributions. While both are linear in momentum, the Dresselhaus SO field also possesses a cubic contribution in momentum.

In this thesis, the persistent spin helix (PSH) state is investigated in transport measurements. The PSH results from balancing the strengths of the two dominant contributions to SO coupling, the Rashba parameter α and the renormalized Dresselhaus parameter β. In this case the SO field is uniaxial and spins are robust against momentum scattering. Quantum corrections to conductivity serve as a convenient tool to detect this symmetry, which exhibits weak localization at the PSH symmetry point and weak antilocalization, if the PSH symmetry is broken.

In the first part of this thesis we use the transition from weak antilocaliztion to weak localization to detect the PSH state. Using a top gate and back gate we demonstrate control of the Rashba SO coupling and, for the first time, tuning of the renormalized linear Dresselhaus term β, independently of each other. This allows us to find the PSH state not just for one particular gate configuration but for a continuous set of gate configurations, where the ratio α/β remains to unity but their overall strength varies. This enables a new concept, the stretchable PSH, where the length for a 2π rotation of the spins becomes tunable. We combine the transport data with numerical self-consistent simulations and can determine all SO coefficients. Stretching of the PSH allows to convey spin polarizations over long distances of up to $25\,\mu$m, before their spin gets randomized by the cubic Dresselhaus term. Furthermore, the stretchable PSH allows to coherently control spin rotations at a fixed position.

In the second part of this thesis, we break the PSH symmetry to extract the SO coefficients purely from transport experiments. We first derive a closed-form expression for the quantum corrections to the conductivity, in the vicinity of the PSH state, which includes the Rashba and linear, as well as the cubic Dresselhaus term. In symmetrically doped wafers with higher density the cubic Dresselhaus term is strong and breaks the PSH symmetry, which is characterized by the reappearance of weak antilocalization. This allows us to determine the cubic Dresselhaus term from fits to the new expression. In the second stage we tune away from the PSH symmetry and are able to extract the linear SO terms by keeping the cubic term fixed. We are thus able to unambiguously determine fundamental band structure parameters that define the Rashba and Dresselhaus SO strength. The obtained results between the two experiments are in very good agreement and compare very well with recent optical studies.

Acknowledgement

Many people have contributed to this work. First of all, I would like to thank Prof. Dominik Zumbühl for being my supervisor during my PhD. I could profit a lot from his vast knowledge in quantum transport, spin orbit interaction and measurement techniques at low temperatures. He guided me through this project and kept me on track, whenever I got lost in details. I am grateful for our numerous discussions, where we step by step uncovered the details in our data and put it in a bigger context. The exchange among scientists is very crucial and I thank him for giving me the opportunity to go to various conferences, which are an excellent platform to share and discuss new ideas.

Secondly, I would like to thank Prof. Carlos Egues, with whom we collaborated intensively for the works presented in this thesis. His frequent visits here in Basel gave me the opportunity for many interesting discussions on the persistent spin helix, spin orbit interaction and beyond and to view the topic from the perspective of a theoretical physicist. His visits were always accompanied by having one, two or three very nice BBQs at the department. I am also happy that we had the chance for a couple of Japanese whiskeys in Kobe, Japan during the PASPS conference in 2016. I would also like to thank Dr. Jiyong Fu, a former post doc from Carlos Egues, for performing the self-consistent simulations presented in this thesis. Thanks to his fast replies and feedback on manuscripts, we could work very efficiently.

I owe big thanks to Prof. Catalina Marinescu, who did the hard mathematical calculations for the quantum corrections and thereby resolved an open issue that prevailed in the community for more than 20 years and made part of this work possible! I am grateful for her patience of walking me through the (tough) mathematical frame work of diagrammatic perturbation theory, filling up my knowledge gaps and breaking down the formalism into more simple terms.

I would like to thank Prof. David Awschalom and Dr. Shawn Mack for providing us with the excellent wafer material, which formed the basis for the experimental part of

this thesis.

In the last 1.5 years of my PhD we also started a collaboration with the group of Prof. Anna Fontcuberta i Morral at EPFL Lausanne on another project, which aimed at growing InAs wires on GaAs nanomembranes. Unfortunately, this project could not make it into this thesis anymore, but first promising results are here now. I would like to thank Prof. Anna Fontcuberta i Morral for the collaboration and her PhD student Martin Friedl, who spent hours on the MBE machine and in the clean room to provide us with an almost unlimited supply of membranes. On this note I would also like to thank Kris Cerveny and Taras Patlatiuk, who will continue to work this project. I wish all of them a lot of success in this promising project.

Experimental physics can be quite tricky, and sometimes just the right switch has to be flipped. If there was some problem with the lock-in or with the electron microscope, help was always around. I want to thank all former and current members of the Zumbühl group for the supportive and helpful atmosphere we have within our group. I would like to thank Florian Dettwiler, who worked on the project before and introduced me to all the finesses of the setup and the measurements. I would also like to thank Mario Palma, with whom I started my PhD at the same day, for being such a good companion over the last years and all the endless and funny discussions we had on Italian (and German) food and how to get rid of the excess calories in the gym. I am grateful for all the time spent outside the lab with the current group members, the occasional trips to the steak house or the adjacent bar at the Rhein. It was a fun time.

Finally, I would like to thank my friends from my studies at ETH for the good times we spent here in Basel or in Zurich or any other place we met. I am very thankful for the always welcoming atmosphere of my friends in my hometown, despite my irregular visits, which always were fun and provided a welcome distraction. I am very thankful to my girlfriend Daniela Pavia Santolamazza for all her encouragement and calming words in times of uncertainty and stress, especially in the last months of writing this thesis. Of course, I want to thank my family for always supporting and encouraging me.

1 Introduction

With the demonstration of the first transistor in 1947 a positive feedback cycle of an application driven research field evolved into the semiconductor and information industry, that shapes our everyday lives today. Fundamental research profited naturally from this positive feedback loop: new semiconductor material systems and device fabrication techniques down to the nanometer scale became available. If such semiconductor micro and nano structures are cooled down to cryogenic temperatures of $\sim 4\,\mathrm{K}$ or even below, the coherence length of the electrons becomes comparable and can even exceed the length of the structures. The coherence length is the length over which an electron maintains its quantum mechanical character. Thus it became possible to investigate quantum mechanical effects in very controllable environments and read them out via electronic transport measurements.

Today this research field is called mesoscopic physics, which has lead to numerous discoveries like the quantum Hall effect [1], conductance quantization [2, 3], Coulomb blockade [4, 5] of single electrons in quantum dots [6] and quantum interference effects such as weak localization [7, 8] and weak antilocalization [9, 10]. As one enters the realm of quantum mechanics another property becomes accessible: the electron spin. The existence of the spin and its quantizing character have been demonstrated in the famous Stern Gerlach experiment already in 1922 [11] and were used to correctly describe the atomic spectra of hydrogen and other atoms. The spin gives rise to other corrections, such as the spin orbit (SO) interaction, which follows from the Dirac equation. Although being a relativistic effect, SO coupling can be explained with classical electrodynamics: the electric field of the nucleus in an atom is seen by electrons as a magnetic field in their rest frame, where it couples to its spin.

One of the first measurements on semiconductors of the III-V group were done in 1953 [12]. This motivated Dresselhaus to review [13] the effects of SO coupling on the electronic band structure in crystals with zinc blende structures. The topic remained without a

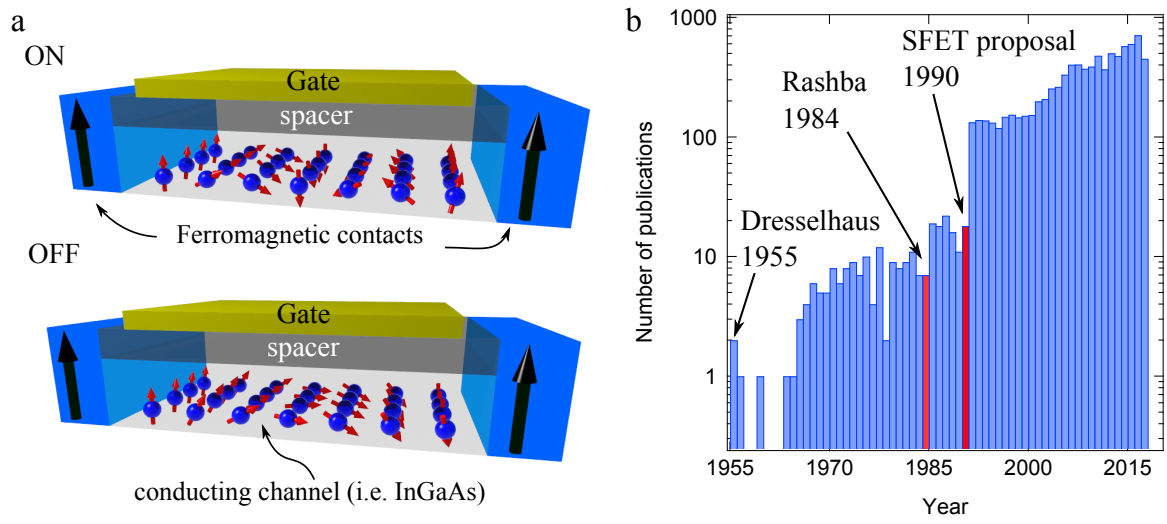

Figure 1.1: a) Working principle of the Datta-Das SFET: A gate controls the electric field in the device, which is seen by electrons as an effective magnetic field and the electron spins precess around it. Their rotation angle is controlled by the gate. If the detector and spin polarization are aligned, a large current (ON state) is measured, misalignment gives a small current (OFF state). These two states can be interpreted as 0 or 1 and could form the basis for a spin logic. Drawing adapted freely from [15]. b) Number of publications in the last decades on the topic of SO coupling in condensed matter physics (data aquired from *Web of Science*, accessed September 3, 2017). After the publications by Bychkov and Rashba [14] and the Datta Das SFET proposal [15] (red colored bars), the number of publications increased by an order of magnitude.

lot of interest in the community for almost three decades. However, it gained increasing interest in the 1980s by the works of Bychkov and Rashba [14] and the proposal of a spin field effect transistor (SFET) by Datta and Das [15]. The proposed SFET device and its working principle are shown in Fig. 1.1 (a). Since then the interest in SO coupling has ever been increasing exponentially, which can be seen by the number of publications shown in in Fig. 1.1 (b).

Today, SO coupling plays a crucial role in all semiconductor systems and is a crucial ingredient for many new effects such as the spin hall effect [16–18], the quantum spin hall effect [19] or Majorana Fermions [20, 21] and motivates new technologically driven research fields such as semiconductor spintronics [22]. Although SO coupling enables control of the electron spin via electric fields, it also causes spin relaxation, which is a limiting factor in experiments. A surprising effect was discovered, when the interplay of the Dresselhaus and Rashba SO fields was investigated. If their strengths are equal, the effective SO field

becomes uniaxial and spin relaxation is suppressed. This high symmetry state is known as the persistent spin helix [23, 24], and its existence was demonstrated quite recently in optical experiments [25, 26]. Due to its unique symmetry property and the suppressed spin relaxation, the PSH offers itself for new applications in spintronics [27, 28] and as a testbench to demonstrate control of all relevant SO parameters.

In this thesis we demonstrate a new concept, the stretchable persistent spin helix, which allows to coherently control the electron spin via electric fields or convey spin information over distances of several micro meters. We achieve this by independently controlling the Rashba and Dresselhaus strengths, to tune into the PSH state and keep their ratio fixed, while also being able to change their overall strength. This provides a powerful tool for future spin based technologies and fundamental research. Quantum interference effects offer themselves as a convenient tool to detect this state [29] and are very sensitive to the SO coupling, thus providing an opportunity to obtain the SO parameters directly from transport measurements. However, this has been a challenging task in the last decades as there is no expression for the magnetoconductivity, including all relevant SO parameters. However, the PSH state introduces a new small parameter, the difference between the Rashba parameter α and the renormalized Dresselhaus parameter β. We use this parameter to derive a new closed-form expression for the quantum corrections in the vicinity of the PSH state, which includes all relevant SO parameters. By employing this new expression, we are able to extract all relevant parameters that make up the SO coupling, which are in agreement with numerical simulations. This new expression thus provides a long anticipated resource to aid in the characterization of SO coupling solely from transport measurements.

1.1 Thesis Outline

This thesis is organized as followed: In chapter 2 background information on relevant topics is given. We summarize the properties of two dimensional electron gas systems (chapter 2.1), give an overview of SO interaction (chapter 2.2), followed by a qualita-

tive description of weak localization and antilocalization (chapter 2.3). We finish the background section with a historical account of the most important theoretical and experimental works over the last three decades on weak localization and antilocalization (chapter 2.4).

In chapter 3 we demonstrate universal control of the SO parameters, where we introduce a new concept, the stretchable persistent spin helix. In chapter 4 we derive a new expression to describe weak localization and weak antilocalization in the PSH regime and demonstrate the validity of the theory in transport experiments, in the broken PSH regime. Chapter 5 summarizes the results and gives an outlook.

2 Background

2.1 Two-dimensional Electron Gas in GaAs Quantum Wells

In this chapter we will briefly summarize the relevant quantities and concepts of the host material system used in this thesis, a GaAs/AlGaAs quantum well (QW). Using the technique of molecular beam epitaxy (MBE), one can grow (almost) perfect crystal layers of a semiconductor material. By using materials with different band gaps and / or doping the material, heterostructures are formed and allow to engineer the band structure along the direction of growth according to the requirements of the device. Today research groups have exquisite control of growing and engineering specific semiconductor heterostructures of various materials (Ga, As, In, Al, Si), with very low surface roughness and defect free material layers. This enables to "grow" devices for electronic and optic applications with specifically tailored properties, such as, density, mobility, spin-orbit interaction and confinement energy.

The binary compound GaAs emerged as one of the most prominent material systems, as it can be grown strain-free with $Al_{0.3}Ga_{0.7}As$ forming very smooth interfaces, which exhibit very little defects. Furthermore, GaAs has a high electron mobility, large Fermi wavelength and large coherence time. By means of modulation doping, the electrically active layer can be separated from the positive donor ions and the charge carriers are confined in two dimensions, where they can move freely and exhibit high mobilities. Due to the semi-insulating character of GaAs (also other semiconductors exhibit this property), electric fields can be applied via gates and also ohmic contacts are possible, making it an excellent candidate for quantum transport measurements.

The crystal structure of GaAs consists of 2 face centered cubic (fcc) lattices, which are displaced by each other by half the diagonal of the fcc cube and form a so-called zinc blende structure, the resulting unit cube of this structure is shown in Fig. 2.1 (a) with the corresponding Miller indices. In the system used in this thesis the materials are grown

along the [001] direction and the two main crystallographic axes, i.e. the natural cleavage directions, are the [110] and [1$\bar{1}$0] directions, which are indicated with the dashed lines in Fig. 2.1 (a), other growth directions are also possible, but the spin orbit coupling (see next chapter), would have different symmetries not suited for the experiments here.

In table 1 the most relevant parameters of GaAs and $Al_{0.3}Ga_{0.7}As$ are shown. Since GaAs has a smaller band gap than $Al_{0.3}Ga_{0.7}As$, there will be a jump in the potential profile at the GaAs/$Al_{0.3}Ga_{0.7}As$ interface and a QW is formed. This is called a type I band interface and heterostructures formed of these two materials allow to confine electrons in a QW.

	GaAs	$Al_{0.3}Ga_{0.7}As$
E_G (300 K) [eV]	1.424	1.798
E_G ($\sim$ 0 K) [eV]	1.519	1.893
lattice constant [Å]	5.65	5.65
dielectric constant	12.9	12.05
effective mass [m_e]	0.067	0.088

Table 1: Basic material properties of GaAs and $Al_{0.3}Ga_{0.7}As$, which are relevant throughout this thesis.

To achieve a conducting channel or layer, doping is necessary. If the dopants are in the active layer itself, a low electron mobility results. The remote modulation doping technique, introduced by Dingle, Störmer, Gossard and Wiegmann [30], allowed to increase the mobility of the charge carriers, which lead to new discoveries, such as the fractional quantum hall effect [31]. Figure 2.1 (b) shows the material profile of a typical modulation doped QW structure and the schematic conduction band diagram on the right: Typical dopants are Si atoms, which are placed in a single layer, also called δ doping layer, which is set back from the GaAs/AlGaAs interface by a few nanometers. In the δ doping layer only a fraction of the dopants will be ionized, while the rest remains bound to the donors. The ionized charges move into the energetically lower conduction band of the QW, formed by the type I band interface, and leave positively charged donors in the δ doping layer,

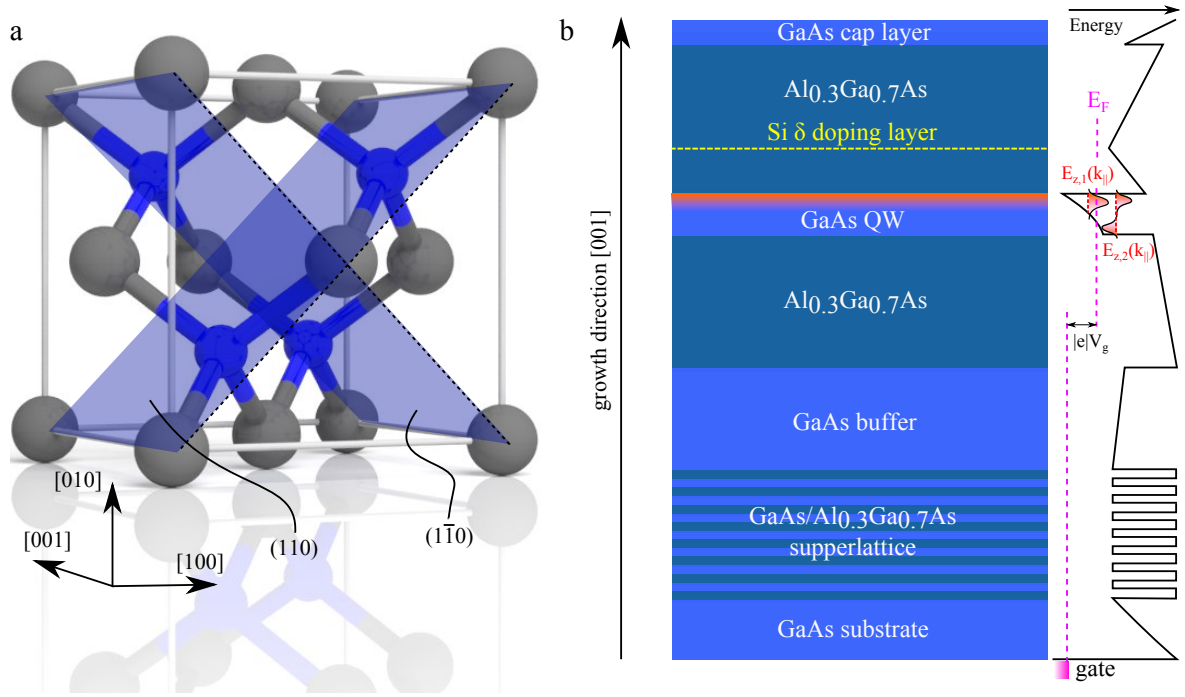

Figure 2.1: a) A GaAs zincblende structure and the respective Miller indices. The main crystallographic directions correspond here to the dashed lines. The gray spheres represent the Ga atoms and the blue ones refer to the As atoms. b) Material profile of a GaAs QW with the schematic conduction band diagram indicated on its right. The superlattice is used to screen the 2DEG from the substrate.

which bind the electrons to the GaAs/AlGaAs interface. This creates a two dimensional electron gas (2DEG), indicated by the red shaded region in Fig. 2.1 (b). As a result of this charge separation between the 2DEG and the positively charged donors, the band structure becomes triangular. A typical heterostructure contains GaAs buffer layers to reduce lattice defects from the GaAs substrate and superlattices of GaAs and AlGaAs alternating, which are used to screen the 2DEG from the substrate. The substrate can act as a back gate, if it is highly doped, which allows to tune the Fermi level E_F with a gate voltage V_g, depicted with the pink line in the band diagram. In the plane of the 2DEG the electrons are described within the single particle picture with parabolic energy dispersion relation. Along the direction of growth the electron energy is quantized due to the confinement potential and forms sub bands, the first two sub bands are indicated in the band structure of Fig. 2.1 (b). The energy of the electrons is given by

$$E_n(k_\parallel) = E_{n,z} + \frac{\hbar^2 k_\parallel^2}{2m^*},$$

with $k_{\parallel} = \sqrt{k_x^2 + k_y^2} \equiv k_F$, the momentum in the plane of the 2DEG, which is equivalent to the Fermi wave vector and $E_{n,z}$ are the quantized energies in z-direction. The quantity m^* is the effective mass, which takes into account the effect of the crystal potential on the band structure. A draw back on QWs is the reduced mobility, since the electron wave function experiences interfaces from both barriers. However, the width of the QW defines the confinement and thus also the extent, to which the electron wave function is spread, which is given its variance $\langle k_z^2 \rangle$. External electric fields allow to tilt the band structure and shift the wave function in a more controlled way as compared to the case of only one barrier. We will see in the next chapter that this also allows to control the strength of the spin orbit coupling.

2.1.1 Transport Properties

The relevant experimental parameters that characterize a 2DEG are the electron density n and the mobility μ, which define the following quantities: The Fermi wavelength $\lambda_F = \frac{2\pi}{k_F}$, Fermi momentum $k_F = \sqrt{2\pi n}$ and Fermi velocity $v_F = \frac{\hbar k_F}{m^*}$, the transport time $\tau_{\mathrm{tr}} = \frac{m^* \mu}{e}$, and the mean free path $l_e = v_F \tau_{\mathrm{tr}}$. If an electric field is applied, electrons start to accelerate along the field lines for the time τ_{tr} until they are scattered. The conductivity σ for such a system can be expressed in various forms with the Drude-Sommerfeld model, which reads

$$\sigma = e^2 \rho_{2D} D \tag{2.1}$$

$$= \frac{n e^2 \tau_{\mathrm{tr}}}{m^*} \tag{2.2}$$

$$= \frac{2e^2}{h} \frac{k_F l_e}{2}. \tag{2.3}$$

where $\rho_{2D} = \frac{m^*}{\pi \hbar^2}$ is the density of states in 2D, which is constant and the diffusion constant in 2D reads $D = \frac{1}{2} v_F^2 \tau_{\mathrm{tr}}$. Equation (2.1) is the so-called Einstein relation and Eq. (2.2) and Eq. (2.3) are simply another way of expressing the Drude condcutivity.

The ratio between the mean free path and the size of the system L distinguishes between a

ballistic ($L < l_e$) or diffusive ($L > l_e$) system. With decreasing temperature another length scale becomes important, the phase coherence l_φ of the electron, being $l_{\varphi,\mathrm{diff}} = \sqrt{D\tau_\varphi}$ in a diffusive system and $l_{\varphi,\mathrm{ball}} = v_F\tau_\varphi$ in a ballistic system. The coherence time τ_φ is the time over which the phase of an electron remains unchanged. In systems with large l_φ, quantum interference effects are possible and lead to weak localization and weak antilocalization in disordered systems (see next chapter) or to universal conductance fluctuations [32–35], which scale as $(L/l_\varphi)^2$ and are thus most pronounced if $l_\varphi > L$. In Eq. (2.3) the value $k_F l_e \sim l_e/\lambda_F$ is an often used measure to describe disorder (Ioffe-Regel criterion): A large value of $k_F l_e$ means that the distance between two scatter sites and the Fermi wavelength is large, so electrons behave quasi classical, this is the case for a typical conductor. If $\lambda_F \sim l_e$, the electrons start to localize, since their wave function spreads over the mean distance between the scatter sites. If $\lambda_F > l_e$, one enters the regime of strong localization, because the potential fluctuations tend to localize the wave functions [36].

In this thesis we investigate diffusive systems in the weakly disordered case i.e. $k_F l_e \gg 1$, and the hierarchy and order of magnitude of the length scales for the systems investigated in this thesis are

$$L > l_\varphi > l_e > \lambda_F$$
$$10^5\,\mathrm{nm} > 10^4\,\mathrm{nm} > 800\,\mathrm{nm} > 40\,\mathrm{nm}.$$

2.1.2 Scattering Mechanisms

The remote modulation doping technique creates ionized donors, which are spatially separated from the 2DEG. This reduces scattering such that the angle between the incoming and scattered electron is typically quite small and is thus called small angle scattering or remote ionized impurity scattering. When the dopants are in the active layer they create short ranged scattering potentials, decreasing the mobility, because now large angle scattering is dominant. There are also other scattering mechanisms, which limit the mobility in GaAs 2DEGs such as scattering from residual charged background impurities, lattice

defects, alloy scattering due to disordered Al atoms in the AlGaAs layer. Furthermore, the confinement energy defines how much the wave function bleeds into the barrier and thus the amount of scattering due to interface roughness. Finally at high temperatures, electron phonon scattering becomes dominant. The effective scattering rate is obtained by summing up the independent scattering rates via Matthiessen's rule:

$$\frac{1}{\tau} = \frac{1}{\tau_{\text{remote}}} + \frac{1}{\tau_{\text{impurity}}} + \frac{1}{\tau_{\text{lattice}}} + \frac{1}{\tau_{\text{alloy}}} + \frac{1}{\tau_{\text{interface}}} + \frac{1}{\tau_{\text{e-ph}}} \cdots . \tag{2.4}$$

Thus, the shortest time scale will dominate the quasi classical transport properties in the Drude model. In the following we will always talk about scattering on long range potentials and the scattering time is called τ_{tr}. This time is different from the so-called quantum lifetime, τ_q for scattering on short range potentials. We note that in the theory part to calculate the weak localization correction, scattering of angles close to π (backscattering) will be considered, because these are the relevant contributions, this backscattering time is denoted with τ_1.

The coherence time defines the quantum mechanical properties of the electrons and thus also the appearance of the aforementioned quantum corrections. The phase coherence is influenced by electron-electron interactions, which can be calculated within Fermi liquid theory [37]. Depending on the temperature, two dominant mechanisms occur. Large energy transfers from electron-electron scattering is present at high temperatures and results in dephasing. This dephasing rate in 2D reads

$$\tau_{ee}^{-1} \approx \frac{\pi}{4} \frac{(k_B T)^2}{\hbar E_{\text{F}}} \ln \frac{E_{\text{F}}}{k_B T}, \tag{2.5}$$

where T is the electron temperature, k_B the Boltzmann constant and E_{F} the Fermi energy. At low temperatures so-called Nyquist dephasing dominates and the Nyquist dephasing rate τ_{N} is given in 2D by

$$\tau_{\text{N}}^{-1} \approx \frac{k_B T}{\hbar} \frac{1}{k_F l_e} \ln \frac{k_F l_e}{2}. \tag{2.6}$$

This process describes, how the electric field fluctuations, due to the movement of the

electrons, causes mutual dephasing. We note that in Eq. (2.6) the disorder term $k_F l_e$ appears again: if the system is strongly disordered, τ_φ is small and vice versa. The effective coherence time τ_φ is given from Eq. (2.6) and Eq. (2.5) by applying the Matthiessen's rule.

2.2 Spin Orbit Interaction

The observations of the fine structure in the spectra of atomic levels could not be explained by the interaction of the electrons with its core, but only via the coupling of the spin with its orbital motion. This coupling is a relativistic effect, which came to be known as spin-orbit (SO) coupling and can be understood by a Lorentz transformation of the atomic cores electric field $\mathbf{E}$, into the rest frame of the electron. There the electric field is seen as a magnetic field, which can couple to its spin. This effective magnetic field reads in the case of $v \ll c$

$$\mathbf{B}_{\mathrm{SO}} = -\frac{1}{c^2}\mathbf{v} \times \mathbf{E} \tag{2.7}$$

where v is the electrons velocity and c the speed of light. Equation (2.7) already indicates that the electron spin can in principle be controlled by an electric field. In a more rigorous quantum mechanical description the SO interaction enters the Hamiltonian by expanding the Dirac equation up to order of $(v/c)^2$ (see for example [38]), which leads to the Pauli term

$$\mathcal{H}_{\mathrm{SO}} = \frac{\hbar}{4m_0^2c^2}\boldsymbol{\sigma} \cdot (\mathbf{p} \times \nabla V), \tag{2.8}$$

where V is the potential acting on the particle, m_0 its mass, p its momentum and $\boldsymbol{\sigma}$ the Pauli spin vector. The SO interaction in atoms comes from the Coulomb potential seen by the electrons and thus splits the electron energy levels, which can be observed in their spectra. In atoms the electric field is radially symmetric and depends only on the distance r, thus $\nabla V = -\frac{\mathrm{d}V}{\mathrm{d}r}\frac{\boldsymbol{r}}{r}$. If this term is plugged into the Pauli term we obtain

$$\mathcal{H}_{\mathrm{SO}} = \frac{\hbar}{4m_0^2c^2}\frac{1}{r}\frac{\mathrm{d}V}{\mathrm{d}r}\boldsymbol{\sigma} \cdot \boldsymbol{L}, \tag{2.9}$$

where $\boldsymbol{L}$ is the orbital momentum. This shows how the SO strength depends on the atomic charge Z of the potential V and the coupling of the orbital momentum $\boldsymbol{L}$ and the electron spin $\boldsymbol{\sigma}$ (i.e. on their quantum number). In fact, the strength of the SO coupling increases with the atomic charge Z to its fourth power, if one approximates r with the

Bohr radius.

In solids such as semiconductors the electrons states are described by bands, which are affected quite substantially by SO coupling. Figure 2.2 shows schematically the band structure of a typical direct band gap semiconductor, using tight binding or $\mathbf{k}\cdot\mathbf{p}$ methods. The conduction band is described by one s-like orbital with orbital quantum number zero

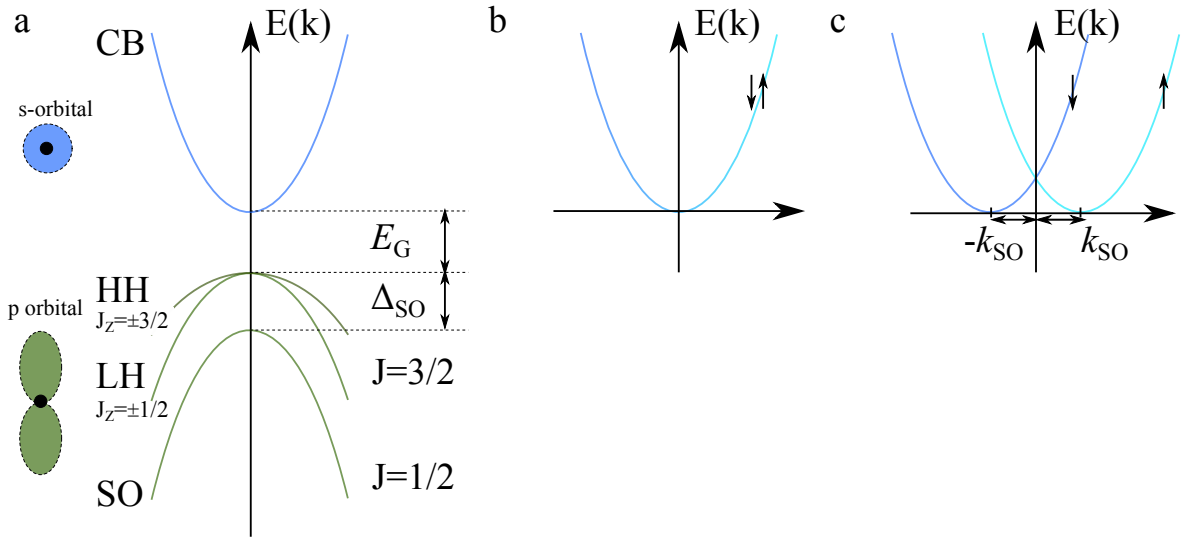

Figure 2.2: a) Band structure for GaAs with the conduction band, formed by the s-orbitals, separated by the band gap E_G and the valence bands formed by p-orbitals, where one band is split off by the energy Δ_{SO} due to the SO coupling. b) Conduction band for a crystalline solid with spatial inversion symmetry. c) Conduction band for crystalline solid with broken spatial inversion symmetry, which results in two parabolas shifted due to the SO coupling.

and total angular momentum $J = 1/2$, thus the SO term has here no direct effect on the electron. On the other hand the valence band is formed by p-like orbitals, which are sixfold degenerate at zero momentum. The p-like orbitals have orbital momentum $L = 1$ and SO coupling has a strong effect on the band structure by lifting the sixfold degeneracy: A band with total angular momentum $J = 1/2$ is separated by the SO gap Δ_{SO}, from the heavy hole (HH) and light hole (LH) band, where $J = 3/2$, which are fourfold degenerate at $k = 0$. In works by Parmenter [39] and Dresselhaus [13] it was found that the crystal symmetry has a profound impact on the Pauli term for the conduction band in zinc blende structures. In fact, there are two symmetry breaking effects that give rise to SO coupling in the conduction band. One arises due to structural inversion

asymmetry (SIA) and the other by bulk inversion asymmetry (BIA), which is present in zinc blende structures. The influence of structural asymmetries can be understood by Kramer's theorem, which states, that every quantum mechanical system with half integer spin obeying time reversal symmetry has a degenerate energy level. For electrons this means, that the following relation holds

$$E_{\uparrow}(\mathbf{k}) = E_{\downarrow}(\mathbf{k}), \tag{2.10}$$

which is depicted schematically in Fig. 2.2 b). However, if BIA or SIA is present, this relation is broken, but Kramer's theorem requires, that time reversal symmetry holds such that

$$E_{\uparrow}(\mathbf{k}) = E_{\downarrow}(-\mathbf{k}), \tag{2.11}$$

which corresponds to a shift in momentum $\mathbf{k}$ of the two parabolas, shown in Fig. 2.2 c). Thus for each given $\mathbf{k}$, spin up and down states have different energy. The parabolas cross at zero momentum, which defines the spin orbit energy E_{SO}, and the minima of the parabolas define the SO momentum k_{SO}, both are related to the actual SO coupling strength.

2.2.1 Dresselhaus and Rashba Spin Orbit Coupling

In this section we describe the two most common inversion asymmetries and their relevant properties in 2D system. The effect on SO coupling due to breaking of the bulk inversion symmetry was first formulated by Dresselhaus in 1955 [13], who calculated the Hamiltonian in a zinc blende structure (i.e. materials with a two atomic basis, such as GaAs or InAs) grown along the $\hat{z}\|[001]$ direction. Then the Hamiltonian in 3D reads

$$\mathcal{H}_{\mathrm{D}} = \gamma[\sigma_x k_x(k_y^2 - k_z^2) + \sigma_y k_y(k_z^2 - k_x^2) + \sigma_z k_z(k_x^2 - k_y^2)], \tag{2.12}$$

which is cubic in electron momentum $\mathbf{k}$. The parameter γ is the material dependent bulk Dresselhaus coefficient. In this thesis we are interested in 2D systems grown along the [001] direction, where the [110] and $[1\bar{1}0]$ direction are the main crystallographic directions. Thus perform a rotation of the coordinate system by $\pi/4$ an then we calculate the expectation value of $\mathcal{H}_{\mathrm{D}}$ by taking $\langle k_z \rangle = 0$ and $k_z^2 \to \langle k_z^2 \rangle$. This gives

$$\begin{aligned} \mathcal{H}_{\mathrm{D}}^{\mathrm{2D}} =& \beta_1(k_-\sigma_+ + k_+\sigma_-) \\ &+ 2\beta_3 \frac{k_+^2 - k_-^2}{k_F^2}(k_-\sigma_+ - k_+\sigma_-), \end{aligned} \tag{2.13}$$

where we have introduced $\beta_1 = \gamma\langle k_z^2 \rangle$, which depends on the width of the QW Further, $\beta_3 = \frac{1}{4}\gamma k_{\mathrm{F}}^2$ defines the strength of the cubic contribution of the Dresselhaus term. In the rotated coordinate system we define $\hat{x}_+ \| [110]$ and $\hat{x}_- \| [1\bar{1}0]$. From Eq. (2.13) we can see that the Dresselhaus Hamiltonian splits up in a linear-in-momentum part and a cubic-in-momentum part. The cubic contribution can play a crucial role in transport measurements [29] and influences spin dynamics [25, 40]. In this thesis the cubic term is considered, which allows in-situ control of the Dresselhaus SO term, via the Fermi momentum k_F enabling new possibilities in spin dynamics (see chapter 3) and transport experiments (see chapter 4).

In transport experiments conduction is defined by electrons at the Fermi level, and one can write Eq. (2.13) in polar coordinates by introducing $(k_+, k_-) = k_F(\cos\varphi, \sin\varphi)$, where φ is the angle between the momentum k_{F} and the [110] axis. This gives

$$\mathcal{H}_{\mathrm{D}}^{\mathrm{2D}} = k_F\beta(\sigma_+ \sin\varphi + \cos\varphi\sigma_-) + k_F\beta_3(\sigma_+ \sin 3\varphi - \sigma_- \cos 3\varphi), \tag{2.14}$$

where $\beta = \beta_1 - \beta_3$, the renormalized linear Dresselhaus term, which reduces β_1 by β_3. The first term with the first harmonic of the polar angle φ maintains the same symmetry as the linear terms in Eq. (2.13) but with a different prefactor β. Since $\beta_3 \propto k_F^2$, and $k_F = \sqrt{2\pi n}$, where n is the electron density in the 2DEG, the renormalized linear Dresselhaus becomes in-situ tunable. Furthermore, the term with the third harmonic of the polar

angle has a different symmetry, and its strength depends on β_3, thus being also tunable with density. The possibility to control also the Dresselhaus term adds an additional knob in experiments and is of crucial importance for the experiments in this thesis.

With advanced control of growing heterostructures and superlattices, as described in the previous chapter, and more finesse and micro- and nano fabrication techniques, it became possible to control the structure inversion asymmetry, known as the Rashba effect [14]. The corresponding Hamiltonian follows directly from Eq. (2.8), where the symmetry breaking electric field points along $\hat{z}\|[001]$ and thus reads

$$\mathcal{H}_{\mathrm{R}}^{\mathrm{2D}} = \alpha(\sigma_- k_+ - \sigma_+ k_-), \tag{2.15}$$

where we have used the same coordinates as in Eq. (2.13) and α is the Rashba parameter. This parameter defines the strength that arises from all internal electric fields such as doping, band structure, due to the growth profile, the Hartree term and also external fields, which can be applied via gate electrodes. There has been some controversy, if the Rashba term plays a role at all [41, 42]: The Ehrenfest theorem states that the force on electrons in a bound state is zero, and thus the average electric field should be zero, and the Rashba effect should vanish. In a qualitative way this can be understood as followed [43]: In a QW the electron wave function is spread across the entire well and also penetrates into the barriers. The electric field originates from the potential drop of the band structure at the barriers (see band structure in Fig. 2.1 (b)). The experienced electric field has to be weighted with the probability of the wave function, which is large at the barrier with the δ doping layer and small at the other barrier, if it is not doped. By using Ehrenfest's relation one can show (see e.g. reference [44]), that the average electric field is zero, if the different effective masses between barrier and QW are ignored [45]. If the effective mass discontinuity is considered, a small finite electric field remains. But this effect alone gives a too small value for α compared to experimental findings. Detailed $\mathbf{k}\cdot\mathbf{p}$ band structure calculations [46] for heterostructures revealed, that the main contribution comes from the valence band offsets to the barrier,making the Rashba effect a considerable

contribution to SO coupling.

Using $\mathcal{H} = \frac{1}{2} g \mu_B \boldsymbol{\sigma} \mathbf{B}_{\mathrm{SO}}$, we can sketch the effective SO field $\mathbf{B}_{\mathrm{SO}}$ by the electrons depending on their momentum. In Fig. 2.3 we show the effective SO field defined by Eq. (2.13) and Eq. (2.15). In Fig. 2.3 (a) only the linear Dresselhaus SO field is drawn, which aligns

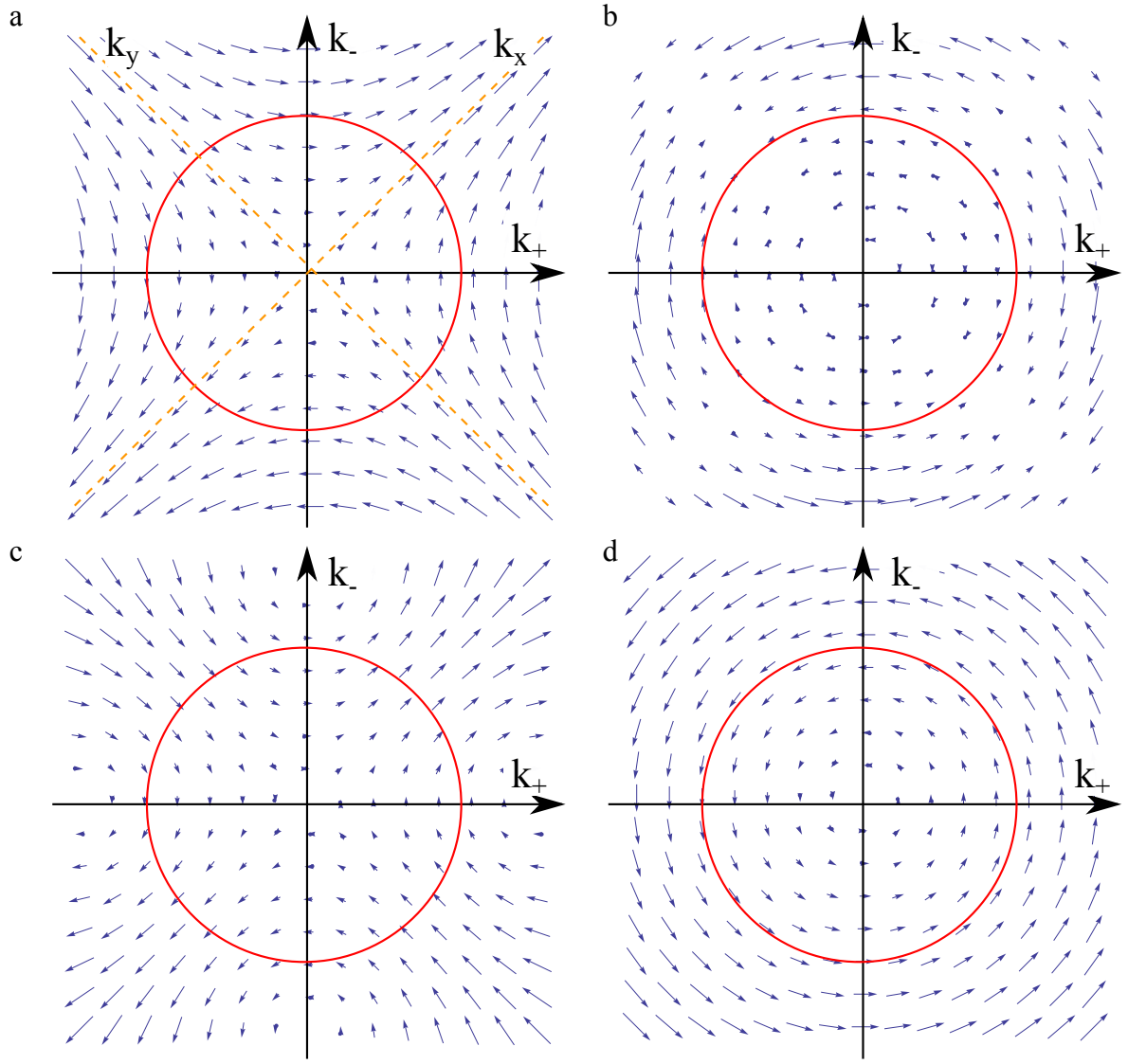

Figure 2.3: SO fields for a) only linear Dresselhaus term β_1, b) only cubic term β_3, c) β_1 & β_3 combined, d) Rashba term α. The red circle depicts to the Fermi surface in 2D.

with the momentum direction along the k_x and k_y direction (dashed orange lines). Panel (b) shows only the cubic Dresselhaus term, where the SO field along the k_x and k_y direction vanishes. Panel (c) depicts the linear and cubic Dresselhaus fields. The Rashba SO field is shown in panel (d). It has rotational symmetry and the SO field is always

perpendicular to the momentum, as is for the cubic Dresselhaus term.

Other contributions to SO coupling. All mechanisms that break the spatial symmetry give rise to SO coupling. For instance, if strain is present, it will deform the crystal lattice. Strain induced SO coupling has the same symmetry as the Rashba term. Another contribution arises at the interface: different atoms at each side of the interface can appear and different bond angles can be shared, which changes the symmetry from D_{2d} to D_{2c} and gives rise to interface inversion asymmetry [44, 47]. In a later chapter we address this topic quantitatively. The statistical distribution of the donors in the delta doping layer gives rise to a locally varying electric field, which adds to the Rashba effect such that $\alpha = \alpha_{\text{norm}} + \alpha(\mathbf{r})$. This term becomes observable in symmetric QW ($\alpha_{\text{norm}} = 0$) and is known as random Rashba SO coupling [48] and was recently observed in InSb 2DEG [49].

2.2.2 The Persistent Spin Helix Regime

In real systems the Rashba and Dresselhaus SO coupling are always present and have to be treated as a sum. The effective SO field is shown in panel a) of Fig. 2.4. Electrons traveling on random paths from point A to B, experience a different SO field, whenever their momentum changes and their spin orientation effectively becomes randomized at point B, which is shown in the lower panel of Fig. 2.4 (a). If we neglect the cubic Dresselhaus term for a moment, we can write the combined SO Hamiltonian from Eq. (2.13) and Eq. (2.15) in the following form:

$$\mathcal{H}_{\text{SO}} = (-\alpha + \beta)\sigma_+ k_- + (\alpha + \beta)\sigma_- k_+. \tag{2.16}$$

In this form one sees that in the case of $\pm\alpha = \beta$ the SO coupling along either k_- or k_+ vanishes. This is the so-called persistent spin helix (PSH) regime [23, 24]. In this case the SO field becomes uniaxial, which is depicted in Fig. 2.4 (b). In the PSH regime the spin dynamics change drastically: scattering does not affect the direction of the SO field anymore and the spin will precess around a fixed axis, and the precession angle is defined

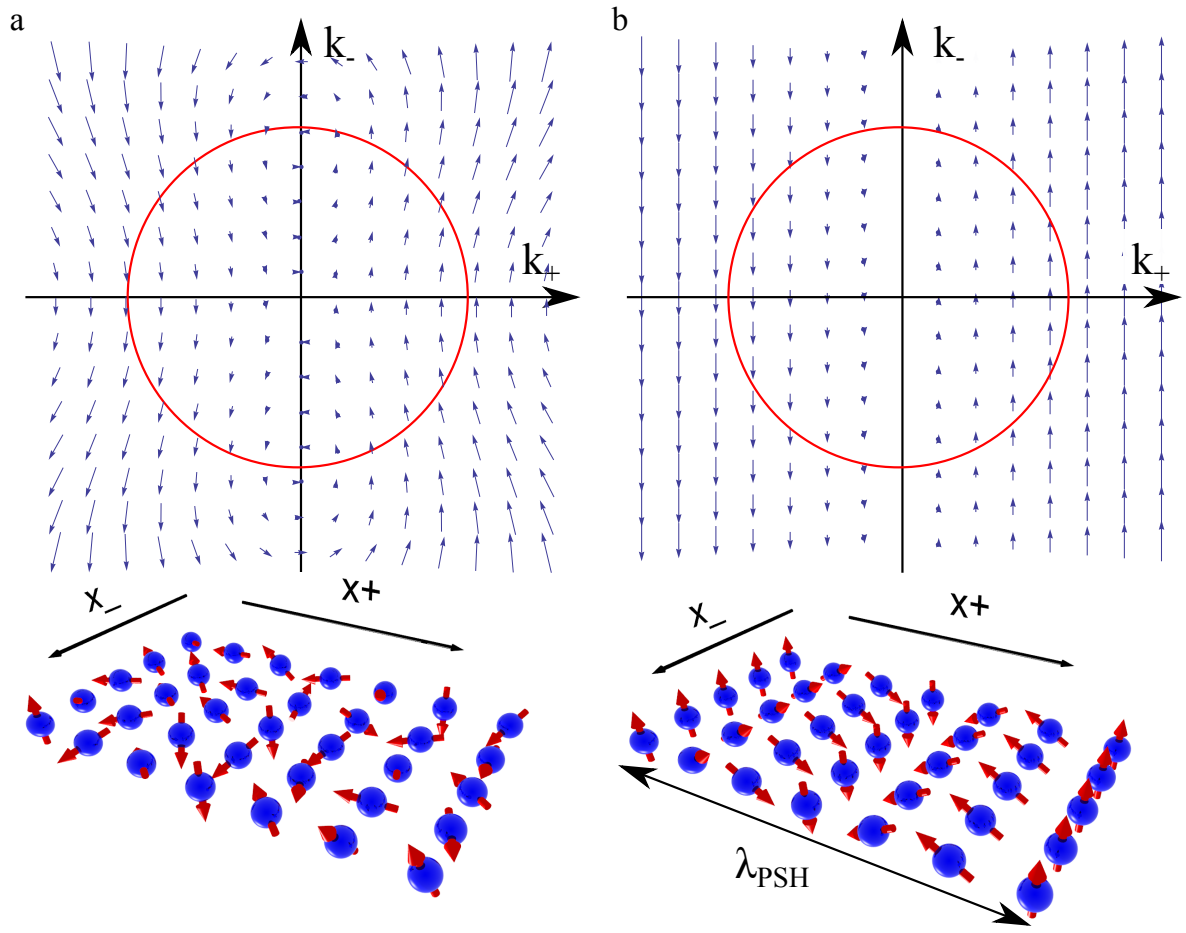

Figure 2.4: a) $\alpha \neq \beta$, the SO field is no longer uniaxial and the electron spin becomes randomized, when diffusing randomly through the sample. b) $\alpha = \beta$, the SO field is uniaxial and the spins describe along the x_+ direction a helical pattern, no spin precession occurs along the x_- direction.

by the distance traveled along x_+. As a result the spins will describe a helical pattern as they travel from point A to B, giving the phenomenon its name. We introduce a new quantity, the SO wavelength λ_{PSH}, the distance to displace an electron to obtain a full 2π rotation in the PSH state. With the Lamor frequency defined by the SO field one directly gets

$$\lambda_{\mathrm{PSH}} = \frac{\hbar^2 \pi}{2m^* \alpha}. \tag{2.17}$$

The pecularity of this symmetry was already recognized in 1995 by Pikus and Pikus [50], when the quantum corrections to conductivity were calculated in the presence of Rashba and Dresselhaus coupling (see next chapter). However, its effect on the spin dynamics was theoretically worked out and put in greater context by Schliemann [23], who proposed a so-called nonballistic SFET. Later on, Bernevig [24] coined the phrase of the persistent spin helix, which is due to the induced SU(2) symmetry for the spins in this case. These considerations are correct only if the cubic Dresselhaus term is neglected. However, if the cubic term becomes significant, it can break the PSH symmetry, and the SO field will be similar to that in Fig. 2.4. In this thesis universal control of the PSH is demonstrated. Furthermore the existence of the PSH symmetry allowed to derive new closed form expressions for the quantum corrections to conductivity around the PSH symmetry, which include all SO terms (α,β_1 and β_3) from Eq. (2.13) and Eq. (2.15). This has been a long standing open topic in the field of quantum transport for more than 20 years. Applying this new theory to a GaAs QW allows to fully determine all relevant SO parameters.

2.2.3 Spin Relaxation and Dephasing

As we just discussed, the effective SO field has a strong influence on the dynamics of spins. To understand the respective contributions of the Rashba and Dresselhaus coupling, a good understanding of the respective relaxation mechanisms is needed. Optical experiments offer the possibility to directly monitor the spin polarization and relate measured relaxation times to theoretical models. The same relaxation and dephasing mechanisms also manifest themselves in transport experiments. Thus a good understanding of those

mechanisms is important to develop theories for transport theories, which has motivated new transprt experiments [51, 52].

The two mechanisms, which govern the spin dynamics in presence of SO coupling [53] are the Elliott-Yafet (EY) mechanism [54, 55] and the D'yakonov-Perel (DP) mechanism [56].

In the EY mechanism scattering at phonons or at impurities (at low temperatures) causes spin relaxation, as the SO coupling mixes the bands with different spins enabling spin flips upon scattering. This type of spin relaxation is present in metals and semiconductors with inversion symmetry (note not asymmetry!) and also materials with strong SO coupling like InSb or InAs/GaSb QW [57, 58]. The EY relaxation rate is proportional to the scattering rate. A common expression for the inverse EY relaxation time reads [53]

$$\frac{1}{\tau_{\mathrm{EY}}} \approx \left(\frac{\Delta_{\mathrm{SO}}}{\Delta_{\mathrm{SO}} + E_{\mathrm{G}}}\right)^2 \left(\frac{E_{\mathrm{F}}}{E_{\mathrm{G}}}\right)^2 \frac{1}{\tau_{\mathrm{tr}}}. \tag{2.18}$$

For typical values in our samples we get τ_{EY} of the order of micro seconds, which is a large time scale compared to the scattering time normally being of the order of pico seconds.

The DP process can be easily understood as follows: In a two dimensional system electrons are being scattered i.e. by impurities and remote doping potentials. The mean time between two scattering events is the transport time τ_{tr}. Between two scattering events the spin precesses for the time τ_{tr} around a magnetic field with the Larmor frequency Ω_{SO}. Upon scattering, the momentum $\mathbf{k}$ and thus the direction of $\mathbf{B}$ is changed, and the spin precesses around a different axis. In the limit for many scattering events these random changes of $\mathbf{B}(\mathbf{k})$ effectively randomize the spin orientation. There are two cases to be distinguished:

i) weak SO coupling: $\Omega_{\mathrm{SO}}\tau_{\mathrm{tr}} \ll 1$

ii) strong SO coupling: $\Omega_{\mathrm{SO}}\tau_{\mathrm{tr}} \gg 1$

Case i) is known usually as the DP mechanism: The spin precesses only a little bit between two events, before it starts to precess around a different axis, and the spin slowly follows

these tiny changes. In this case, the spin performs a random walk on the Bloch sphere and one finds (see also chapter 3.6.8) for the spin relaxation time $\tau_{\mathrm{DP}}^{-1} = \Omega_{\mathrm{SO}}^2 \tau_{\mathrm{tr}}$, which is also known as motional narrowing. If the SO coupling is strong (i.e. case ii)), the spin rotates very fast, as if it has flipped before being scattered at all. Upon scattering the direction of the SO field changes, and same process starts with a completely different spin orientation, and the spin orientation is completely lost. More detailed calculations [59, 60] involving the Rashba and Dresselhaus terms show that the spin relaxation times are anisotropic in the plane of a 2DEG and are of the form

$$\frac{1}{\tau_{\pm}^{\mathrm{DP}}} \propto (\alpha \pm \beta_1)^2, \qquad \frac{1}{\tau_{z}^{\mathrm{DP}}} \propto (\alpha^2 + \beta_1^2), \tag{2.19}$$

where $\pm$ stands for the coordinates along the [110] and [1$\bar{1}$0] direction. In chapter 3.6.8 we will give explicit expressions for these times and apply them to a GaAs 2DEG.

Other relaxation mechanisms. There are two further mechanisms, which are not related to the spin orbit coupling. First, the Bir-Aronov-Pikus mechanism [61], which causes spin relaxation due to exchange and relaxation of electrons-hole pairs, which is dominant in hole systems. Second, in semiconductors with nuclear magnetic moment the hyperfine interaction of the electron spins with the nuclear environment causes spin relaxation [62], this effect becomes important in quantum dots or other systems with strong confinement.

2.2.4 Spin Orbit Parameters

In this chapter we have introduced the Rashba and Dresselhaus SO coupling, which are defined by the parameters α and γ. In this thesis these two parameters are independently determined and compared to their theoretical values, which are usually obtained from multi-band $\mathbf{k}\cdot\mathbf{p}$ calculations. In literature the Dresselhaus coefficient γ is often denoted with b_{41}^{6c6c}, and its value in GaAs is often given as 27 eVÅ^3 [43]. However, depending on the method of calculation, its value varies from 7-36 eVÅ^3, an ample overview in theory

and experiment is given in the supplementary of reference [63]. Recent studies and more detailed calculations find that the value tends to be in the range of $10\,\mathrm{eV\AA^3}$, the results presented in this thesis are $\sim 11\,\mathrm{eV\AA^3}$.

As we have discussed previously, the Rashba effect arises from the structure inversion asymmetry. Thus there are internal electric fields due the asymmetry in the bandstructure and static contributions. An externally applied electric field will also change the band structure. The Rashba parameter can be written as $\alpha = rE_{\mathrm{static}} + r_{41}^{6c6c}E_{\mathrm{z}}$, where the first term is a constant that depends on the sample itself, and the second term describes, how the band structure is changed by an external electric field. In chapter 3.3.4 the different contributions to the Rashba parameter will be discussed. The parameter r_{41}^{6c6c} is also calculated from multi-band $\mathbf{k}\cdot\mathbf{p}$ calculations and is given in units of $\mathrm{e\AA^2}$. Since electric fields can be conveniently applied via gates, the value of r_{41}^{6c6c} could be determined quite reliably in transport experiments [64–66]. From simulations one obtains a value of $r_{41}^{6c6c} = 5.206\,\mathrm{e\AA^2}$ [43]. However, in a QW this value changes almost by a factor 2 [67]. In this thesis we obtain a value of $r_{41}^{6c6c} \sim 10\,\mathrm{e\AA^2}$, which is in good agreement with theory.

The question remains how these two parameters can be determined experimentally. As already mentioned, optical experiments are the most convenient method, which allows to measure the effect of Rashba and Dresselhaus SO coupling on the electron spin [18, 68–70]. Transport measurements on the other hand are more complicated since the spins can not directly be observed, and the details of the underlying SO mechanisms have to be built in a theory for the conductivity. There are two popular types of transport measurements known to allow determination of the SO parameters: beating patterns in Shubnikov de-Haas oscillations have been widely used to measure the SO induced spin splitting in the single sub-band regime. However, only the Rashba term could be reliably determined. Quantum corrections to the magnetoconductivity are the other method, which is the main topic of this thesis and will be discussed in detail in the next chapter.

2.3 Localization and Magnetoconductivity

In their seminal work, published in 1979, Elihu Abrahams, Philip Anderson, Donald Licciardello and Tiruppattur Ramakrishnan [71] introduced the concept of localization based on a scaling argument for the first time. This motivated the development of genuine microscopic theories for the localization on the conductivity in low-dimensional systems. The first result in this direction was put forward by Gorkov [7], who calculated the quantum corrections to conductivity using the diagrammatic perturbation theory. Abrahams and Gorkov both found a logarithmic decrease of the conductivity, which depends on ratio of the mean free path l_e and the coherence length l_φ. This effect came to be known as weak localization (WL) and is a precursor for strong localization predicted by Anderson in 1958 [36]. In this chapter, we provide an intuitive description of weak localization and weak antilocalization (WAL), which counteracts the WL effect due to SO coupling. Finally, we will discuss the most prominent theoretical and experimental works, that led successively to a more complete picture of mangetoconductivity, accounting for the effect of SO interaction. In the following, we always consider 2D systems with the coordinates x and y in the plane, where the magnetic field is applied perpendicular to the $x-y$ plane in the z-direction and is denoted by B_z.

2.3.1 Weak Localization

In a normal conductor with diffusive transport the conductivity is given by the classical Drude formula (see Eq. (2.2)). The WL effect is observed at very low temperatures, where the coherence time τ_φ can exceed the transport time by several orders of magnitude and the Drude conductivity is reduced by the term

$$\Delta\sigma(0) = \frac{e^2}{2\pi^2\hbar} \ln \frac{\tau_\varphi}{\tau_\mathrm{tr}}. \tag{2.20}$$

An intuitive picture for describing WL was developed by Bergmann [72], which is based on the interference of coherently backscattered paths. For backscattered paths, the electron

wave splits into two partial waves, which travel the path in the clockwise (cw,+) and counter-clockwise (ccw,-) direction with equal probability $T^{\pm}$ (see the dashed (+) and solid lines (-) in Fig. 2.5 a)). The total quantum mechanical return probability $P_{\mathrm{ret}}^{\mathrm{qm}}$ is then given by the squared sum of the transmission amplitudes $T^{\pm}$ of the two partial waves:

$$P_{\mathrm{ret}}^{\mathrm{qm}} = |T^{+} + T^{-}|^2 = |T^{+}|^2 + |T^{-}|^2 + T^{+}T^{-^*} + T^{+^*}T^{-}. \tag{2.21}$$

Here, the first two terms correspond to classical backscattering of one path only in each travel direction and the last two terms to their self-interference. If time reversal symmetry holds, $T^{+} = T^{-} = T$, the self-interference terms double the classical return probability, as the partial waves interfere constructively at their origin. This effectively increases the resistance and thereby decreases the conductivity. All paths within areas of the order l_{φ}^2 contribute to this quantum correction. In presence of an externally applied magnetic field B_{z}, the electrons traveling along the backscattered paths enclose an area A and attain a magnetic flux $\Phi = B_z A$, which adds an Aharonov-Bohm (AB) phase $\delta = 2\pi B_z A/(h/e)$, where h is the Planck constant. Thus, there is an additional phase factor to the transmission amplitudes, which depends on the magnetic field: $T^{\pm} = T\mathrm{e}^{\pm i\delta}$. The return probability thus becomes

$$P_{\mathrm{ret}}^{\mathrm{qm}} = 2|T|^2 \left(1 + \cos\left(2\pi \frac{\Phi}{\Phi_0}\right)\right), \tag{2.22}$$

where $\Phi_0 = h/(2e)$ is the magnetic flux quantum. The first term corresponds to the "incoherent" addition of two scattered waves of equal amplitude. The second term is the "quantum interference" term, due to coherent corrections, and oscillates depending on the flux Φ. If this term is positive, conductivity is either suppressed compared to the incoherent term, due to constructive interference, or enhanced, due to destructive interference of the second term. This second term is the "quantum correction" (QC) to conductivity. In a disordered sample there are many paths of different areas. The oscillatory behavior of those paths will average out, and only paths of area l_{φ}^2 will contribute. Via the AB effect,

the external magnetic field will *remove* these paths from contributing to the QC: a closed path with area $A < l_\varphi^2$ is threaded by one flux quantum, which results in a phase difference of one radian between the partial waves, which thus interfere destructively and no longer contribute to WL. The magnetoconductivity attains a V shaped curve, as shown in Fig. 2.5 b), with a minimum in conductivity at $B_z = 0$. The QC can be calculated within the framework of the diagrammatic perturbation formalism [7, 73]. The magnetoconductivity (MC) $\Delta\sigma(B)$ was first calculated by Hikami, Larkin and Nagaoka [9] and reads, in the case without SO coupling,

$$\Delta\sigma(B_z) - \Delta\sigma(0) = \frac{e^2}{2\pi^2\hbar}\left[\Psi\left(\frac{1}{2}+\frac{B_\varphi}{B_z}\right) - \Psi\left(\frac{1}{2}+\frac{B_{tr}}{B_z}\right) + \ln\frac{\tau_\varphi}{\tau_{tr}}\right], \tag{2.23}$$

where Ψ is the digamma function, and B_φ and B_{tr} is the coherence field and transport field respectively, which is the field needed to dephase the electron wave function by 1 radian in the time τ_φ and τ_{tr} respectively. Equation (2.23) shows the difference of the QC to the magnetoconductivity $\Delta\sigma(B_z)$ and the QC at zero magnetic field, $\Delta\sigma(0)$ (see Eq. (2.2)). The ratio $r_\varphi = B_\varphi/B_z$ is a measure for how many of the coherently backscattered paths contribute to the $\Delta\sigma(B_z)$. For $r_\varphi = 1$ all paths with areas l_φ^2 contribute, and for $r_\varphi \to 0$ all paths are dephased and no longer contribute. This is shown by the color scale in Fig. 2.5 a): The color indicates which of the paths have become dephased as a function of the magnetic field and no longer contribute to the WL curve in Fig. 2.5 b), which has the same color coding.

2.3.2 Weak Antilocalization

If SO interaction is considered, the conductivity has no longer a minimum at $B_z = 0$, but exhibits a local maximum. This effect is called weak antilocalization (WAL), which is proportional to the SO strength and can completely suppress the weak localization effect, even flipping the sign of the QC. This effect can be explained within the D'yakonov Perel picture (see chapter 2.2.3): In the presence of SO interaction the electron spin precesses around an effective SO field between two collisions, which is perpendicular to its

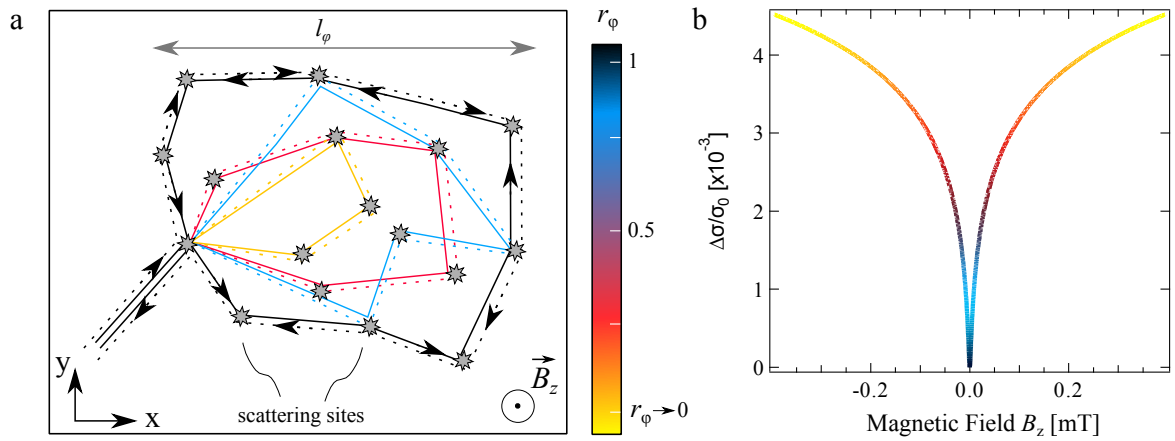

Figure 2.5: a) Coherently back-scattered paths, in clockwise (dashed lines) and counter clockwise direction (solid lines). The color of each path corresponds to the color scale on the right and indicates how an increasing magnetic field B_z reduces the ratio $r_\varphi = B_\varphi/B_z$. b) Typical WL curve, normalized by the Drude conductivity σ_0 and $\Delta\sigma$ is given by Eq. (2.23). The color scaling is chosen to be the same as in a): For $r_\varphi = 1$ all paths with areas l_φ^2 contribute and for decreasing r_φ fewer paths contribute to the QC, and the classical Drude conductivity is restored.

momentum $\mathbf{k}$ and lies in the plane of the 2D system. After each collision the momentum direction changes and the spin precesses around a different axis, and after many scattering events its orientation becomes randomized. We denote the initial spin state with $|i\rangle$, which experiences a consecutive series of small rotations R_j resulting in the final state $|f^+\rangle = R_n \cdot \cdots R_2 \cdot R_1|i\rangle = R|i\rangle$. For the spin that has traveled the path in counter clockwise direction, rotations occur in the reversed order, and the rotation angles are also reversed such that the final state reads $|f^-\rangle = R_1^{-1} \cdot R_2^{-1} \cdot \cdots \cdot R_N^{-1}|i\rangle = R^{-1}|i\rangle$. The rotation matrix R is unitary, which means that $R^{-1} = R^\dagger$. Following the argumentation of Bergmann [72] the return probability under the influence of SO interaction can be calculated as in section 2.3.1:

$$P^{\mathrm{qm}}_{\mathrm{SO,ret}} = (\langle f^+| + \langle f^-|)(|f^+\rangle + |f^-\rangle) = 2 + \langle f^+|f^-\rangle + \langle f^-|f^+\rangle. \tag{2.24}$$

With the unitary property of R we can rewrite the interference terms as

$$\langle f^-|f^+\rangle = \langle f^+|f^-\rangle = \langle i|R^2|i\rangle. \tag{2.25}$$

For no SO interaction R corresponds to the unitary matrix, and we recover the case of WL, where $\langle f^+|f^-\rangle = 1$. In the limit of strong SO interaction, upon return to the origin, the spin is completely randomized and is likely to point in one direction as in any other direction. It can be shown [72] that after averaging over all randomly rotated angles, the terms for the QC in Eq. (2.25) give $\langle f^+|f^-\rangle = -1/2$, thereby reducing the backscattering amplitude by a factor of 2 compared to WL. This can be interpreted that the relative spin orientation is 2π, which gives destructive interference, since electrons are fermions and require a 4π rotation to obtain its original wave functions.

Figure 2.6 b) shows a typical WAL trace: at zero magnetic field a local maximum of the conductivity appears, which rapidly decreases before increasing again, showing WL behavior. To understand the effect of the magnetic field qualitatively we introduce l_{SO}

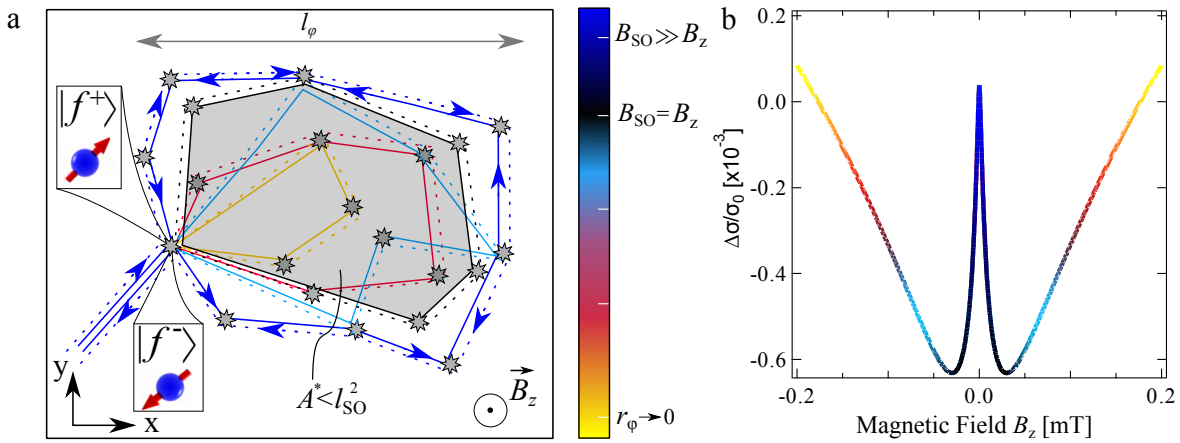

Figure 2.6: a) SO interaction causes the relative spin orientation for the clockwise traveled state $|f^+\rangle$ and counter clockwise traveled state $|f^-\rangle$ to be closer to 2π, thereby causing destructive interference (dark blue path) and cause a local maximum at zero magnetic field, see panel b). Increasing the magnetic field decreases conductivity up to $B_z = B_{\mathrm{SO}}$, corresponding to the black colored path. Here, the WAL curve in panel b) shows a minimum, and from thereon WL takes over, corresponding to the paths in the gray shaded area with $A < l_{\mathrm{SO}}^2$ a). The color scale corresponds to the paths that have been dephased in panel a) and the value of the conductivity with increasing B_z.

as an additional length scale, which corresponds to the distance traveled by the electron, until the spin has rotated by 1 radian due to SO interaction, which we express as an effective magnetic field $B_{\mathrm{SO}} = \frac{\hbar}{2el_{\mathrm{SO}}^2}$. Thus all paths encompassing areas A, which obey $l_\varphi^2 \leq A \leq l_{\mathrm{SO}}^2$ reduce the backscattering amplitude due to SO interaction. At zero magnetic

field, this is indicated with the dark blue path in Fig. 2.6 a) and the local maximum in Fig. 2.6 b). An increasing magnetic field gradually dephases these paths completely, which can no longer contribute to WAL. This happens until $B_z = B_{SO}$, which corresponds to the minima in the WAL curve Fig. 2.6 b). All "large" paths have been dephased and only paths where the SO interaction does not cause any significant spin rotations remain (i.e. R is the identity matrix in Eq. (2.25)), these paths are within the gray shaded area in Fig. 2.6 a), which corresponds to $A^* < l_{SO}^2$. From hereon all paths within the gray shaded area are dephased with increasing magnetic field and we observe the WL effect as in Fig. 2.5.

Finding a closed form of the quantum corrections to conductivity in the presence of all SO terms, has proven to be a challenging task. Part of this thesis was done in close collaboration with Catalina Marinescu, who derived a closed form expression in the case of the Rashba and linear as well as cubic Dresselhaus SO terms, the detailed calculations are shown in chapter 4. The resulting expression reads

$$\begin{aligned}\Delta\sigma(B_z) = -\frac{e^2}{4\pi^2\hbar}\Bigg[&\Psi\left(\frac{1}{2}+\frac{B_\varphi}{B_z}\right) - 2\Psi\left(\frac{1}{2}+\frac{B_\varphi}{B_z}+\frac{B_{SO-}+3B_{SO3}}{2B_z}\right)\\ &-\Psi\left(\frac{1}{2}+\frac{B_\varphi}{B}+\frac{B_{SO-}+B_{SO3}}{B_z}\right)+2\ln\frac{B_{tr}}{B_z}\Bigg],\end{aligned} \tag{2.26}$$

where $B_{SO-} \propto (\alpha-\beta)^2$ and $B_{SO3} \propto \beta_3^2$ and B_{tr} is the transport field. In chapter 4 of this thesis we will discuss the details of this expression and its derivation and apply it to an experimental situation to determine SO parameters in GaAs QW.

2.4 Magnetoconductivity: The Last 30 Years

The first observation of the WL effect was in thin metal films by Gerald Dolan and Douglas Osheroff [74] and shortly after by David Bishop, Daniel Tsui and Robert Dynes [75] in inversion layers of Si MOSFETs. This was followed by observations of the WAL effect in thin metal films [10], InP MOSFETs [76] and GaAs heterostructures [77]. To adequately describe the WAL signature, a theory for the quantum corrections has to include the

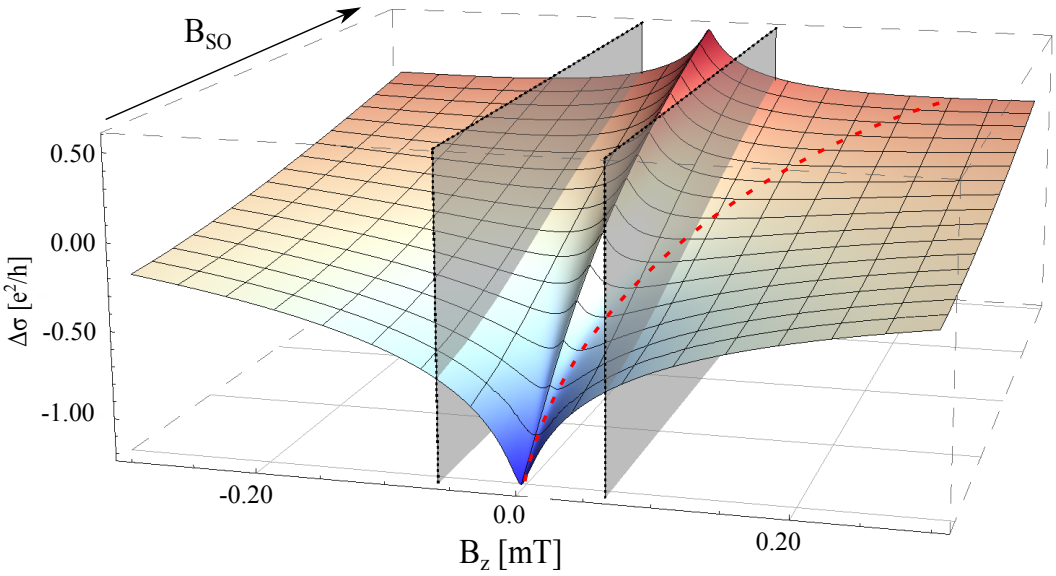

Figure 2.7: Quantum corrections as described by Eq. (2.26) for varying SO strength B_{SO} via the parameter $B_{\mathrm{SO}-}$ in Eq. (2.26), which defines the minima of the WAL curve, which is indicated with the red dashed curve, which approaches $B_{\mathrm{z}} = 0$ as the SO coupling strength becomes very small. The transport field B_{tr} is indicated by the gray planes.

dominant SO relaxation mechanism, which are the Elliott-Yafet process (EY) or the D'yakonov Perel (DP) process. The EY process dominates in thin metal films, inversion layers of MOSFETs and materials with large SO splitting of the valence band (i.e. InSb or GaSb) [57, 78]. The DP process is most pronounced in modulation doped semiconductor heterostructures and depends on the details of the effective SO field, defined by the bulk and structure inversion asymmetry, as discussed in chapter 2.2.1.

Furthermore a theory has to describe the WAL peak and the minima of the magneto-conductivity, which occur symmetrically around $B_{\mathrm{z}} = 0$ at a specific field, denoted with B_{SO}. Most theories are developed in the so-called diffusive approximation, which is valid for $B_{\mathrm{z}} \ll B_{\mathrm{tr}}$, but also have to satisfy $B_{\mathrm{SO}} \ll B_{\mathrm{tr}}$, to be able to describe WAL correctly. In Fig. 2.7 we show the quantum corrections to conductivity with increasing SO strength, denoted by B_{SO} and out of plane field B_{z}. The gray shaded planes indicate the transport field. At very small B_{SO}, WL is observed and with increasing B_{SO} WAL appears. With increasing SO strength the WAL minima, indicated by the red dashed curve, occur outside of the gray planes, and a theory in the diffusive approximation can no longer determine meaningful SO parameters. The D'yakonov Perel' process describes how the spin between

two collisions rotates around the effective SO field with the Larmor frequency Ω_{SO} (see chapter 2.2.3). The angle θ between two scattering events is thus given by $\theta = \Omega_{\mathrm{SO}}\tau_{\mathrm{tr}}$. In the diffusive regime $\theta \ll 1$, and one can express the validity of the diffusive regime in terms of magnetic fields by $B_{\mathrm{SO}} \ll B_{\mathrm{tr}}$. In materials with high mobility $\theta \geq 1$ and $B_{\mathrm{SO}} \geq B_{\mathrm{tr}}$, which means that a theory developed in the diffusive approximation will no longer work. However, nowadays the interest is towards materials with strong SO interaction (such as InAs, InSb) and with high mobilities. This makes it necessary to develop theories that are valid beyond the diffusive approximation. In the last decades various theories in these two regimes have been developed considering various spin relaxation mechanisms. In the following paragraphs we will give an overview of the most common theories in these two different regimes and compare them with each other. First we will look at the theories in the diffusive approximation and then at the works beyond the diffusive approximation.

2.4.1 The Diffusive Approximation $B_{\mathrm{SO}}, B_{\mathrm{z}} \ll B_{\mathrm{tr}}$

Hikami, Larkin and Nagaoka [9]. This is the first work to describe the QC in presence of a magnetic field B_{z} and SO interaction and spin scattering due to magnetic impurities. The spin relaxation due to SO coupling is considered to be isotropic such that the the spin relaxation times τ^x_{SO} and τ^y_{SO} in the plane are equal. The spin relaxation time due to magnetic impurities is denoted by τ^z_{S}. In this description the spin relaxation rates due to SO interaction and magnetic scattering are added. The resulting QC are described by the following analytical expression:

$$\begin{aligned}\Delta\sigma(B_{\mathrm{z}}) = -\frac{e^2}{2\pi^2\hbar}\Bigg[&\Psi\left(\frac{1}{2}+\frac{B_{\mathrm{tr}}}{B_{\mathrm{z}}}\right) - \Psi\left(\frac{1}{2}+\frac{B_1}{B_{\mathrm{z}}}\right)\\ &+\frac{1}{2}\Psi\left(\frac{1}{2}+\frac{B_2}{B_{\mathrm{z}}}\right) - \frac{1}{2}\Psi\left(\frac{1}{2}+\frac{B_3}{B_{\mathrm{z}}}\right)\Bigg],\end{aligned} \tag{2.27}$$

with the characteristic fields

$$B_1 = B^z_{\mathrm{SO}} + 2B^x_{\mathrm{SO}} + 2B^x_{\mathrm{S}} + B_\varphi,$$
$$B_2 = 2B^z_{\mathrm{S}} + 4B^x_{\mathrm{S}} + B_\varphi,$$
$$B_3 = 2B^z_{\mathrm{S}} + 4B^x_{\mathrm{SO}} + B_\varphi,$$

where the fields B^j_i contain the relaxation times τ^j_i via the expression $B^j_{\mathrm{i}} = \frac{\hbar}{4eD\tau^j_{\mathrm{i}}}$, where D is the diffusion constant in 2D. The indices correspond to $i = \mathrm{SO}, \mathrm{S}$ and $j = x, y, z$. In this description the SO relaxation $\tau^{x,y}_{\mathrm{SO}}$ times vanish in a strictly 2D system and only τ^z_{SO} remains. Equation (2.27) does not give any information about the origin of the SO interaction, but only allows to quantify it.

Al'tshuler, Aronov, Larkin, Khmel'nitskii [79]. The authors elaborate on the formalism to calculate the QC in two- and three- dimensional semiconductor systems. The authors also investigate how electron-electron interaction and SO coupling due to bulk inversion asymmetry enters the formalism and gives rise to WAL. This work thus paved the way for later more detailed descriptions of the QC.

Iordanskii, Lyanda-Geller and Pikus [80]. As pointed out in the previous work by Al'tshuler SO interaction due to bulk inversion asymmetry gives rise to WAL. In this work the QC are calculated explicitly by including the full Dresselhaus Hamiltonian for a QW grown in the [001] direction. Since transport happens with states at the Fermi surface, it was recognized here for the first time that the linear Dresselhaus term in a 2D system becomes renormalized by the cubic term and attains a density dependence (see also chapter 2.2.1). This opens the door for in-situ control of the Dresselhaus SO coupling (see also chapter 3). Expressions for zero and finite magnetic field B_z are found. Terms

that describe the SO coupling are

$$B'_{\mathrm{SO}} = \frac{\hbar}{4e}\left(\frac{2m^*}{\hbar^2}\beta\right)^2, \tag{2.28}$$

$$B^{\mathrm{D}}_{\mathrm{SO}} = B'_{\mathrm{SO}} + B_{\mathrm{SO3}}, \tag{2.29}$$

$$\text{with} \quad B_{\mathrm{SO3}} = \frac{\hbar}{4e}\left(\frac{2m^*}{\hbar^2}\beta_3\sqrt{\frac{\tau_1}{\tau_3}}\right)^2, \tag{2.30}$$

where τ_1 is the backscattering time (equivalent to the transport time τ_{tr}) and τ_3 its third harmonic. Here, β is the renormalized linear Dresselhaus term, which has been introduced in chapter 2.2.1. Interestingly, if all terms of the order of B'_{SO} are omitted, one gets the expression derived by Hikami, where $B^x_{\mathrm{SO}} \equiv B^{\mathrm{D}}_{\mathrm{SO}}$.

Pikus and Pikus [50]. Here, the previous model by Iordanskii, Lyanda-Geller and Pikus was extended even further to include also Rashba type SO interaction, denoted by α. One of the remarkable discoveries by including the Rashba SO interaction was that at $\alpha = \beta$ and $\beta_3 = 0$, the QC to conductivity behave as if there is no spin relaxation, because the spin rotations along the backscattered paths turn out to be zero and the QC show WL. The full extend of this state and its modern interpretation was later given by Schliemann [23] and Bernevig [24] and is now known as the persistent spin helix regime (see chapter 2.2.2).

The QC with Rashba and linear and cubic Dresselhaus type SO couplings cannot be calculated analytically for arbitrary ratios of α/β and $\beta_3 > 0$ and thus have to be calculated numerically. However, in the case of $\beta = \pm\alpha$ and $\beta_3 > 0$, the equations can be solved analytically, and one gets the same expression as in the previous model, where B'_{SO} is ignored. The Rashba SO field as a function of α is given as

$$B^{\mathrm{R}}_{\mathrm{SO}} = \frac{\hbar}{4e}\left(\frac{2m^*}{\hbar^2}\alpha\right)^2. \tag{2.31}$$

Other theories. Without any claim of completeness, we mention three further theories, which are only slight modifications of the above ones: The first one is the theory by

Maekawa and Fukuyama [81], which extends the Hikami model by including Zeeman splitting. The introduction of a Zeeman field was motivated from the observation of a WAL behavior in granular Cu films, when only an in-plane field was applied [82]. The QC in p-type QW with one or two sub bands, where SO coupling is strong, was calculated in a series of papers by Averkiev, Golub and Pikus [83–85] finding that the spin relaxation times can be tuned with the QW confinement and a closed form expression for the QC. Another analytical expression was derived by Punnoose [86], which is equivalent to the Iordanskii model, but explicitly considers only Rashba type SO coupling and no Dresselhaus type SO coupling.

Experiments in the diffusive approximation. The Hikami model was published back-to-back with an experimental paper by Kawaguchi and Kawaji [8], who observed weak localization in Si MOSFET inversion layers, where no SO effects were present. The theory was successfully applied to determine the coherence time between 4 and 12 K, finding a T^{-2} dependence. In an experiment by Bergmann [10] a Mg film was systematically covered by a thin layer of Au adatoms, which posseses strong SO interaction. By gradually increasing the Au concentration, the SO coupling strength was increased, which resulted in the appearance of WAL. Choi [87] and co-workers used the HLN model to determine systematically the coherence time as a function of the width of a 2DEG for temperatures from 0.3 K to 4 K, finding good agreement with the Fermi liquid theory.

The simple closed form of the Hikami model makes it still a very convenient tool to extract coherence times and finds recently a growing interest in the extraction of SO strength in topological insulators such as InAs/GaSb QW [58] or thin SnTe films [88].

The first observation of WAL in GaAs heterostructures was made by Kawaji in 1984 [77], using the theory from Kawabata (a theory from the ballistic limit) and Maekawa & Fukuyama, the SO relaxation times could be extracted.

Almost a decade later two works [89, 90] attempted to systematically investigate the origin of the SO interaction in GaAs 2DEGs by using an electrostatic gate to control

the density in the sample. In the first work Dresselhaus [89] found no dependence of B_{SO} on mobility and thus ruled out the EY mechanism, concluding that the SO field is due to inversion asymmetries, where the bulk inversion asymmetry dominates over the structure inversion asymmetry. From the density dependence of the SO energy splitting the Dresselhaus coefficient γ could be obtained. In a similar work by Hansen [90], high densities were reached, from which they concluded that SO scattering becomes isotropic and the EY mechanism is dominating. These two works showed that a more detailed model for quantum interference is needed to correctly describe SO effects from quantum transport.

The Iordanskii and Pikus models allowed a more systematic and detailed investigation of the QC. The Pikus model was slightly modified for a QW, grown along the [110] direction, in a work by Hassenkam [91], where fits to the QC allowed to extract values for Eq. (2.29) and Eq. (2.31), which allowed to obtain the SO parameters α and γ.

In In-based heterostructures the Rashba coupling strength is quite large compared to the Dresselhaus coupling strength, and the Iordanskii model can be applied by replacing the Dresselhaus with Rashba SO coupling. This was done systematically in the work by Koga [92], where electrostatic gates were used to systematically tune the Rashba strength and obtain its value as a function of the effective electric field, finding linear behavior of the Rashba strength on the electric field. The proportionality factor is a fundamental band structure parameter, often denoted by r_{41}^{6c6c} [43], and can be compared to literature values.

In a review and experimental paper by Knap [93] the Hikami, Iordanskii and Pikus models are tested against each other in $In_{0.15}Ga_{0.85}As$ based QWs. The extracted SO fields given by Eq. (2.28), Eq. (2.29) and Eq. (2.31), that are obtained from fits with the Pikus model, are then plotted as a function of density finding general agreement. However, the agreement is achieved by plugging in theoretically expected values and parameters from self-consistent simulations, whereas no fit as a function of the density is done, which could give less biased results.

In a work by Pedersen [94] p-type GaAs QWs were investigated and the model by Averkiev was applied, but the fits just barely capture the WAL minima, which is the case because of the strong SO coupling and the non-applicability of the theory in this case, as the authors also state.

2.4.2 Beyond the Diffusive Approximations, $B_{\mathrm{SO}} \gg B_{\mathrm{tr}}$

In this section we describe the theories, which are valid beyond the diffusive approximation and remove its limitation $B_{\mathrm{tr}} \gg B_{\mathrm{z}}$. The theories are described in chronological order according to their publication year. We note that all these models do not yield any analytical or closed form expressions and always have to be calculated numerically.

Kawabata [95]. Very shortly after the work of Hikami, this model was the first one developed beyond the diffusive approximation: first for the 3D case [96] and later for the 2D case [95]. No details on the relaxation mechanisms are given. Furthermore the model takes into account paths with 1 and 2 collisions, which have no area and thus do not contribute to the coherent backscattering processes. This was corrected in later works. The derived expression has to be calculated numerically.

Wittmann & Schmid [97]. This quasiclassical theory is derived in real space by calculating the return probability of an electron after multiple scattering events to its origin. The dephasing magnetic field enters as an exponential damping in the probability amplitude. Spin-orbit coupling is not considered. The obtained results have to be calculated numerically and are similar to the ones obtained from the Hikami model (i.e. all $B_{\mathrm{SO}i} = 0$ in Eq. (2.27)).

D'yakonov & Zduniak [98, 99]. Based on the model of Kawabata, D'yakonov [98] derived a universal behavior at large magnetic fields, if the scattering is isotropic, and paths with one or two collisions are excluded, which have been erroneously included in the theory of Kawabata. At large B_{z} the QC show a universal behavior, which obeys

the following relation $\Delta\sigma \propto 7.74/\sqrt{B_z}$. SO interaction and the low field limit are not considered in this theory. The D'yakonov model was extended by Zduniak to include dephasing due the SO coupling and the limitation due to the coherence time. This allowed the model to be valid also for $B_z \ll B_{tr}$ and to describe the universal behavior of the QC at high fields. Spin relaxation due to SO coupling is described with the in-plane spin relaxation times $\tau_{SO}^{x,y}$ and out of plane spin relaxation time τ_{SO}^{z}, as in the HLN model. Interestingly, this model agrees quite well with the one from Hikami if SO strength is small. The model is used to extract SO times in a $In_{0.47}Ga_{0.53}As$ QW [99], where the universal behavior is shown as well.

Dmitriev [100]. Being similar to the previous works, the authors considered here also non-backscattering contributions to the conductivity and give a quasiclassical description of these. These non-backscattering contributions cause a small reduction of the WL amplitude. The usual contribution comes from the constructive interference of the backscattered paths as discussed in chapter 2.3. However, it turns out that there are also contributions to conductivity. A partial wave can travel from its initial point i on closed path in the cw direction in the sequence $i \to 1 \to 2 \to \cdots N \to i$ and in the ccw direction in the sequence $i \to N \to \cdots \to 2 \to i$, skipping the scatter site 1. As a result the phase difference between the cw and ccw path is different and their partial waves interfere destructively, thereby reducing backscattering. This effect becomes important in clean samples, where the number of collisions is small. Spin-orbit coupling is not considered in this model.

Miller [101]. The initial work of Lyanda-Geller [102] described the QC in the limit of high mobilities and strong SO coupling, which are linear-in momentum. In a later work with Miller [101] the theory was extended to include all relevant SO contributions for a GaAs 2DEG, i.e. α, β_1 and β_3. The resulting expression for the QC needs to be calculated

numerically and depends on the effective SO fields,

$$B^*_{\text{eff}} = \frac{2m^{*^2}}{e\hbar^3}(\alpha^2 - \beta_1^2 + 2\pi n\beta_1\gamma - \pi^2\gamma^2 n^2), \tag{2.32}$$

and

$$B^*_{\text{SO}} = \frac{m^{*^2}}{36e\hbar^3}\pi^2\gamma^2 n^2, \tag{2.33}$$

which can be extracted from fits to the data. The theory is valid for $B_\text{z} > B^*_{\text{eff}}$. In this work the theory is directly applied to measured magentoconductivity data in a GaAs/AlGaAs heterostructure, where gate voltages were used to control the density in the sample, allowing to directly extract the SO parameters α, β_1 and γ. We note, that in this case the linear Dresselhaus term β_1 is not renormalized as in the ILP model and thus does not attain a density dependence. The theory is not complete as it does not take into account coherent interference contributions and remains blind to $\pm\alpha = \beta$.

Glazov and Golub [103, 104]. To overcome some of the limitations in the previous theories, an attempt to fully describe the weak antilocalization in the ballistic limit was first done by Golub [103], who derived a numerical solution for the QC, which includes either the Rashba SO coupling or the linear Dresselhaus coupling and also considers the non-backscattering contributions. In a later work [104] the theory was extended to include all linear and cubic Dresselhaus terms as well as the Rashba term.

Probuaev and Golub [105]. In this specific theory the calculations of the QC include the Dresselhaus SO Hamiltonian for QWs, which are grown along the [110] and [111] direction, which are different from the [001] case. Along the [110] direction the Dresselhaus SO Hamiltonian reads

$$\mathcal{H}_D^{110} = \frac{\beta}{2}k_y\sigma_z + \frac{3\beta_3}{2}k_\text{F}\sin(3\varphi)\sigma_z, \tag{2.34}$$

where β and β_3 are defined as in the case for [001] QWs (see chapter 2.2.1). Remarkably, in this case, the SO coupling only couples with the spins z-component. Along the [111]

direction, one gets

$$\mathcal{H}_D^{111} = \frac{2\beta}{\sqrt{3}}(k_y\sigma_x - k_x\sigma_y) + \frac{4\beta_3}{\sqrt{6}}k_{\mathrm{F}}\sin(3\varphi)\sigma_z. \tag{2.35}$$

Due to the inhomogeneous distribution of donors in the doping layers, a random electric field appears, called the random Rashba field, and as a result the Rashba parameter depends on position in the plane. The correlation length l_c of the random Rashba field serves as a parameter to distinguish between various cases: If $l_{\mathrm{mfp}} \ll l_c$ spin flip processes occur, which is the situation as described by the Hikami model but here now in the ballistic regime. In the opposite limit $l_c \ll l_{\mathrm{mfp}}$ the QC are described with the Glazov model [104] but with different growth directions of the QW.

Sawada and Koga [106]. This is a numerical model, where the return probability is calculated by summing up a fixed number of scattering events for predefined closed loops. The set of closed loops can be scaled with the mean free path and are randomly picked when calculating the return probability. The effect of magnetic field, dephasing, SO coupling, interactions of the pseudospin and Zeeman field can be included on-demand via modulation of scattering amplitude. If only the Rashba term is considered, the model proves to be equivalent to the Golub model [103]. The total computation time is relatively small, making this model a promising tool.

Experiments beyond the diffusive approximation. We will review experiments, where only the theories beyond the diffusive approximation are applied. These experiments are conducted mostly in $\mathrm{In}_x\mathrm{Ga}_{1-x}\mathrm{As}$ systems, where the SO interaction is strong and high mobilities are present and thus $B_{\mathrm{SO}} \gg B_{\mathrm{tr}}$. We note that there are many experiments, which extracted the SO relaxation time τ_{SO} as a single parameter, which is not a very suitable parameter if compared across different experiments, to check for the validity of a specific theory. A better approach is to use fundamental parameters, such as the Rashba parameter, since these can be tuned in the experiment, and the underlying

dependencies reveal more information and can be compared with theoretical predictions of these parameters.

The work by Miller [101] serves as an ideal example. In a high mobility GaAs structure the authors used electrostatic gates to systematically change the density n and extract the effective SO fields (see Eq. (2.32) and Eq. (2.33)), from which they successfully extracted the Rashba parameter α and Dresselhaus coefficient γ.

The model developed by Golub [103] was tested mostly in $In_{0.47}Ga_{0.53}As$ systems, where the Rashba parameter was extracted. This is a convenient material system, as beating patterns in the Shubnikov de-Haas oscillations allow to extract the Rashba parameter, which allows direct comparison with the results from the model for the QC. In particular the works of Studenikin [107], Guzenko [108] and Zhou [109] compared their results with these two methods finding overall good agreement. To our knowledge there is so far no experimental study testing the extended Glazov model.

In a quite recent work Spirito [110] compared the models of Iordanskii [80], Miller [101], Zduniak [99] and Golub [103] in a AlGaN/GaN 2DEG with each other, by extracting the Rashba parameter α, finding good agreement across all models, except the one from Zduniak.

2.4.3 Summary

In table 2 we summarize the discussed models in tabular form for convenience in chronological order of publication year. On a side note: we distinguish between closed form expressions, which consist only of known functions, like the Digamma function and analytical expressions, which may also contain infinite series.

The discussed models here are, to our knowledge, the most prominent describing QC to conductivity with SO coupling. Despite this plethora of models, what strikes most, is that there are almost no closed-form expressions that describe QC with a detailed picture of the

underlying SO mechanism. Although extensive numerical calculations can be performed on a normal computer nowadays, closed form expressions are much more convenient for an experimentalist and allow to check if the limits of the model reproduce already existing theories, i.e. the limit of no SO interaction or if $\alpha = \beta$. Obtaining the SO coupling and phase breaking times from fits to WL and WAL curves, is standard procedure in quantum transport, but despite more than 30 years of research the progress on the theories has advanced only in small steps. In the vincinity of the PSH regime the parameter $\alpha - \beta$ is small and thus opens up a new regime, where the derivation of new expressions for the magnetoconductivity becomes possible. Short of a general formula for any Rashba and Dresselhaus strength, it would give a broad and powerful new tool into the hand of future experiments to characterize and tune the SO parameters. In this thesis we have derived such a new closed-form expression for the QC in 2D systems, which contains the Rashba and linear and cubic Dresselhaus SO couplings. The derived expression is valid in the limit of a weakly broken PSH symmetry, and enables to unambiguously extract all SO parameters.

Year/Authors	**regime**	**SO mechanism**	**comments**
1980 Hikami et al. [9]	diffusive	$\tau_{\mathrm{SO}}^{x} = \tau_{\mathrm{SO}}^{y}$, τ_{SO}^{z}, EY-type	closed form expression
1981 Maekawa & Fukuyama [81]	diffusive	see above	closed form expression, includes Zeeman splitting
1981 A'ltshuler et al. [79]	diffusive	DP and EY[1]	closed form expression
1984 Kawabata [95]	beyond diff.	$\tau_{\mathrm{SO}}^{x} = \tau_{\mathrm{SO}}^{y}$, τ_{SO}^{z}, EY-type	only numerically solvable
1987 Wittmann & Schmid [97]	beyond diff.	none	only numerically solvable, quasiclassical theory in real space
1994 Iordanskii et al. [80]	diffusive	$\beta = \beta_1 - \beta_3$, β_3, DP-type	analytical expression for finite B_z and $B_z = 0$[2]
1995 Pikus & Pikus [50]	diffusive	α, β, β_3, DP-type	only numerically solvable[2]
1996 Knap et al. [93]	diffusive	α, β, β_3, DP-type	review of Iordanskii and Pikus models with experiments
1997 D'yakonov & Zduniak [98, 99]	beyond diff.	$\tau_{\mathrm{SO}}^{x,y} = \frac{1}{2}\tau_{\mathrm{SO}}^{z}$, EY-type	only numerically solvable, universal behavior at high B_{z}
1997 Dmitriev [100]	beyond diff.	none	only numerically solvable
1998 Lyanda-Geller [102]	beyond diff.	linear in momentum, DP-type	only numerically solvable
1998 Averkiev et al. [83–85]	diffusive	$\tau_{\parallel}$, $\tau_{\perp}$, EY type	analytical expression, p-type QWs, with one and two subbands
2003 Miller et al. [101]	beyond diff.	α, β_1, β_3, DP-type	extended theory from Lyanda-Geller[3], for $B > B_{\mathrm{eff}}^{*}$
2005 Golub [103]	beyond diff.	α or β_1, DP-type	only numerically solvable
2006 Glazov & Golub [104]	beyond diff.	α, β, β_3, DP-type	only numerically solvable
2006 Punnoose [86]	diffusive	α, DP-type	analytical expression, similar to Iordanskii model but for α
2014 Porubaev & Golub [105]	beyond diff.	random Rashba $\alpha(\mathbf{r})$, β_1 and β_3, EY- (if $\alpha(\mathbf{r})$ dominates) & DP-type	QWs grown along [110] and [111], only numerically solvable
2017 Sawada & Koga [106]	beyond diff.	various interaction mechanisms *on-demand*	only numerically solvable

Table 2: [1]other relaxation mechanisms such as intervalley scattering are considered, [2]for $\alpha = \beta$ and $\beta_3 > 0$ the expression from HLN is obtained; [3]the Lyanda-Geller expression can also be used, results differ by a factor 3 and α and β_1 cannot be distinguished.

3 Stretchable Persistent Spin Helices in GaAs Quantum Wells

Florian Dettwiler,[1] Jiyong Fu,[2,†] Shawn Mack[3,‡], Pirmin J. Weigele,[1] J. Carlos Egues,[2] David D. Awschalom[3,4] and Dominik M. Zumbühl[1]

[1] *Department of Physics, University of Basel, CH-4056 Basel, Switzerland*

[2] *Instituto de Física de São Carlos, Universidade de São Paulo, 13560-970 São Carlos, São Paulo, Brazil*

[3] *California NanoSystems Institute, University of California, Santa Barbara, California 93106, USA*

[4] *Institute for Molecular Engineering, University of Chicago, Chicago, Illinois 60637, USA*

[†] Permanent address: Department of Physics, Qufu Normal University, Shandong 273165, China

[‡] Permanent address: Naval Research Laboratory, Washington, D.C. 20375, USA

This chapter has been published in *Physical Review X 7, 031010 (2017)*

3.1 Abstract

The Rashba and Dresselhaus spin-orbit (SO) interactions in 2D electron gases act as effective magnetic fields with momentum-dependent directions, which cause spin decay as the spins undergo arbitrary precessions about these randomly oriented SO fields due to momentum scattering. Theoretically and experimentally, it has been established that by fine-tuning the Rashba α and renormalized Dresselhaus β couplings to equal *fixed* strengths $\alpha = \beta$, the total SO field becomes unidirectional thus rendering the electron spins immune to decay due to momentum scattering. A robust persistent spin helix (PSH), i.e., a helical spin-density wave excitation with constant pitch $P = 2\pi/Q$, $Q = 4m\alpha/\hbar^2$, has already been experimentally realized at this singular point $\alpha = \beta$, enhancing the spin lifetime by up to 2 orders of magnitude. Here, we employ the suppression of weak antilocalization as a sensitive detector for matched SO fields together with independent electrical control over the SO couplings via top gate voltage V_T and back gate voltage V_B to extract all SO couplings when combined with detailed numerical simulations. We demonstrate for the first time the gate control of the renormalized β and the *continuous locking* of the SO fields at $\alpha = \beta$; i.e., we are able to vary both α and β controllably and continuously with V_T and V_B, while keeping them locked at equal strengths. This makes possible a new concept: "stretchable PSHs", i.e., helical spin patterns with continuously variable pitches P over a wide parameter range. Stretching the PSH, i.e., gate controlling P while staying locked in the PSH regime, provides protection from spin decay at the symmetry point $\alpha = \beta$, thus offering an important advantage over other methods. This protection is limited mainly by the cubic Dresselhaus term, which breaks the unidirectionality of the total SO field and causes spin decay at higher electron densities. We quantify the cubic term, and find it to be sufficiently weak so that the extracted spin-diffusion lengths and decay times show a significant enhancement near $\alpha = \beta$. Since within the continuous-locking regime quantum transport is diffusive (2D) for charge while ballistic (1D) for spin and thus amenable to coherent spin control, stretchable PSHs could provide the platform for the much heralded long-distance communication $\sim 8 - 25$ μm between solid-state spin

qubits, where the spin diffusion length for $\alpha \neq \beta$ is an order of magnitude smaller.

3.2 Introduction

The inextricable coupling between the electron spatial and spin degrees of freedom – the spin-orbit (SO) interaction – underlies many fundamental phenomena such as the spin Hall effects – quantum and anomalous [111] – and plays a crucial role in newly discovered quantum materials hosting Majorana [112] and Weyl fermions [113]. In nanostructures the SO coupling strength can be varied via gate electrodes [64, 65]. As recently demonstrated [114], this enables controlled spin modulation [15] of charge currents in nonmagnetic (quasiballistic) spin transistors.

The SO coupling in a GaAs quantum well has two dominant contributions: the Rashba [14] and the Dresselhaus [13] effects, arising from the breaking of the structural and crystal inversion symmetries, respectively. When the Rashba α and Dresselhaus β SO couplings match at $\alpha = \beta$ [23, 24], the direction of the combined Rashba-Dresselhaus field becomes momentum independent, thus suppressing D'yakonov-Perel spin-flip processes, provided that the cubic Dresselhaus term be small. The significantly enhanced spin lifetime at $\alpha = \beta$ enables nonballistic spin transistors and persistent spin helices [23, 24]. However, despite substantial efforts, so far this symmetry point has been achieved only at isolated points with finely tuned system parameters [25, 26, 29], which is too difficult to be reliably attained *on demand* as required for a useful technology.

3.3 Stretchable Persistent Spin Helices

Here, we overcome this outstanding obstacle by (i) using a technique that allows independent control of the SO couplings via a top gate voltage V_T and a back gate voltage V_B while (ii) simultaneously measuring the suppression of weak antilocalization (WAL) in an external magnetic field as a sensitive probe for matched SO couplings. While gate tuning of the renormalized Dresselhaus coefficient β was already theoretically described

in 1994 [80], we demonstrate this for the first time here in an experiment, and employ this tunability to show robust *continuous locking* of the Rashba and Dresselhaus couplings at $\alpha(V_T, V_B) = \beta(V_T, V_B)$ over a wide range of densities n, i.e., a "symmetry line" (not a point) in the (V_T, V_B) plane. This allows us to introduce the concept of the "stretchable persistent spin helix", see Fig. 3.1, with spin density $s_{x_+} \sim \sin(Qx_+)$, $s_{x_-} = 0$, and $s_z \sim \cos(Qx_+)$ and *variable* pitch $P = 2\pi/Q$, $Q = 4m\alpha/\hbar^2$. The stretchable PSH makes possible gate control of the spin precession over *long distances* due to strong protection from spin decay by up to 2 orders of magnitude enhanced spin lifetimes at the symmetry point $\alpha = \beta$ – without requiring in-plane electric fields to induce drift [70], and without relying on micron-width channels to suppress decay [115].

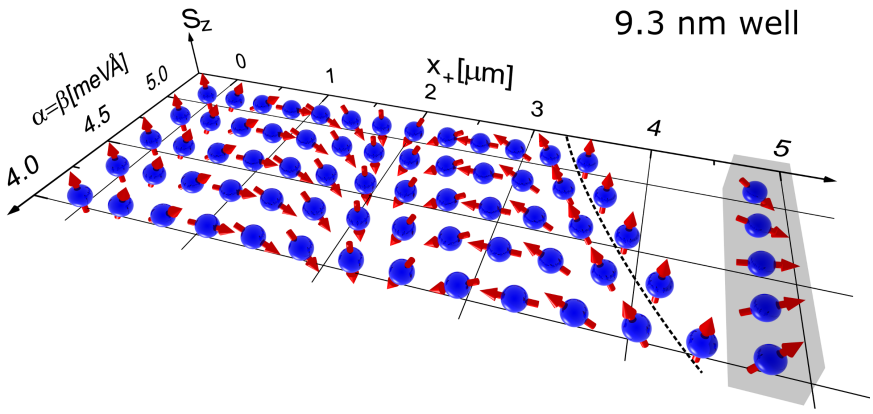

Figure 3.1: Stretchable PSHs. Illustration of spin helices at different values of $\alpha = \beta$ accessible in the measurements. The position x_+ for one 2π rotation (dashed curve) is changing for the gate-locked regime $\alpha = \beta$. The gray box highlights how the spin rotation can be controlled (in situ) at fixed position $\sim$4.8 μm by $\sim \pi/2$ over the same range of $\alpha = \beta$. The $\hat{x}_+ || [110]$ and $\hat{x}_- || [\bar{1}10]$ axes define the 2D plane.

Long-distance spin communication. — Within the range of the continuously matched-locked SO couplings $\alpha = \beta$, quantum transport in the well is diffusive for charge (2D) while essentially ballistic (1D) for spins (see Supplemental Material (SM), Sec. 3.6.8). A stretchable PSH could thus be used to coherently couple, e.g., spin qubits over unprecedented long distances. Figure 3.1 illustrates how spin information can be conveyed between spins via a stretchable PSH. These stretchy waves can be excited upon injection of spin polarization; see, e.g., Refs. [25, 26]. Other spin communication modes can be envisaged with this setup. The distance is limited mainly by the deviation from

$\alpha = \beta$ and by the cubic Dresselhaus term, which is small in this range as we quantify later on and leads to spin decay with spin-diffusion lengths $\lambda_{\text{eff}} \sim 8 - 25\mu$m over which spin dephases by 1 rad. Note that this type of spin manipulation and spin transfer is not possible for a helix $\alpha \neq \beta$, since λ_{eff} quickly drops below the helix pitch as the SO couplings are deviating from the symmetry point.

The full electrical control of the SO couplings demonstrated in our 9.3-nm wide quantum well can tune from $\alpha = \beta = 5\,$meVÅ to $4\,$meVÅ, thus enabling stretchable PSHs with pitches P stretching from $3.5\,\mu$m to $4.4\,\mu$m; see Fig. 3.1. Within the shortest spin-diffusion length $\lambda_{\text{eff}} \sim 8\,\mu$m for our 9.3-nm well, controlled spin rotations by an angle $\theta = Qx_+ = 2\pi x_+/P$ can be performed under spin protection on any spin sitting at a position x along the stretchable PSH by varying P in the range above. For example, a spin at $x \sim 4.8\,\mu$m can be rotated by $\Delta\theta \sim \pi/2$ as P varies in the range above, see gray box shading in Fig. 3.1. Thus, stretchable helices could provide a platform for long-distance spin communication.

Additional results. — WAL is also used to identify other regimes such as the Dresselhaus regime $\alpha = 0$ in a more symmetrically doped sample. Combined with numerical simulations, we extract the SO couplings α and β, the bulk Dresselhaus parameter γ, the spin-diffusion lengths and spin-relaxation times over a wide range of system parameters. We also quantify the detrimental effects of the third harmonic of the cubic Dresselhaus term which mainly limits spin protection. Interestingly, our spin-diffusion lengths and spin-relaxation times are significantly enhanced within the locked $\alpha = \beta$ range, thus attesting that our proposed setup offers a promising route for spin protection and manipulation.

In what follows, we first explain tuning of the Rashba coupling, then the essential density dependence of the Dresselhaus coupling β that enables the continuous locking of the SO fields, how it also leads to spin decay at higher densities, followed by the relevant weak.localization-weak-antilocalization (WL-WAL) detection scheme, measurements, and

simulations. A full account of our approach, including additional data and details of the model and simulations, is presented in the Appendix and the SM.

3.3.1 Controlling the Rashba Coupling α

The Rashba coefficient [14] α can be tuned with the wafer and doping profile [25] as well as *in-situ* using gate voltages [64, 65] at constant density n and thus independent of the Dresselhaus term, see below. A change of top gate voltage V_T can be compensated by an appropriate, opposing change of back gate voltage V_B [see Fig. 3.2 (a)] to keep n fixed [66, 116] while changing the gate-induced electric field δE_Z in the quantum well, where $z \perp$2D plane. Another Rashba term due to donor electric fields [117, 118] is negligible in our structures; see SM.

3.3.2 Linear & Cubic Dresselhaus Terms in 2D

Because of to the well confinement along the z direction (growth), the cubic-in-momentum bulk (3D) Dresselhaus SO interaction gives rise to, after the projection into the lowest quantum well subband eigenstates, distinct terms that are linear and cubic in $\mathbf{k}$, the 2D electron wave vector. The linear-in-k term has a coefficient $\beta_1 = \gamma\langle k_z^2\rangle$ and turns out practically independent of density in the parameter range of interest here. The cubic-in-k term, on the other hand, is density dependent and has yet two components with distinct angular symmetries: (i) the first-harmonic contribution proportional to $\sin\phi$ and $\cos\phi$ and (ii) the third-harmonic contribution proportional to $\sin 3\phi$ and $\cos 3\phi$; here ϕ is the polar angle in 2D between $\mathbf{k}$ and the [100] direction (see SM). Interestingly, the first-harmonic contribution with coefficient β_3 has the same angular symmetry as both the linear-in-k Dresselhaus β_1 term (see Refs. [50, 80]), and the Rashba α term. An additional term with the same form – the interface Dresselhaus term [44] – could also play a role, see SM.

To a very good approximation, the coefficient $\beta_3 \simeq \gamma k_F^2/4$, where the Fermi vector $k_F \simeq \sqrt{2\pi n}$ and n is the carrier density of the 2D gas. This neglects the tiny angular anisotropy

in the Fermi wave vector due to the competition between the Rashba and Dresselhaus effects (especially in GaAs wells). Note that by approximating $\beta_3 \simeq \gamma\pi n/2$, both the first-harmonic and the third-harmonic parts of the cubic-in-k Dresselhaus term actually become linear in k (see SM for details) and, more importantly, become density dependent. We can now group the linear-in-k Dresselhaus term β_1 together with the first-harmonic contribution β_3 into a single renormalized Dresselhaus term by defining $\beta = \beta_1 - \beta_3$. It is this density-dependent renormalized coefficient β that can be tuned with a gate voltage to match the Rashba α coupling continuously. This matching leads to a k-independent spinor (or, equivalently, to a k-independent effective SO field), whose direction is immune to momentum scattering. In this way we achieve independent, continuous control of the Rashba and Dresselhaus terms by using top gate and back gate voltages. This is an *unprecedented* tunability of the SO terms within a single sample.

Spin decay at higher densities. — The strength of the third-harmonic contribution of the Dresselhaus term is also described by the coefficient β_3. This term, however, is detrimental to spin protection as it breaks the angular symmetry of the other linear SO terms and makes the spinor k dependent and susceptible to in-plane momentum scattering, even for matched couplings $\alpha = \beta$. As we show, the detrimental effect of the third-harmonic contribution does not prevent our attaining the continuous locking over a relevant wide range of electron densities.

Gate-tunable range of the Dresselhaus coupling β. — For the narrow quantum wells we use here, β_1 is essentially gate independent since the wave function spreads over the full width of the well. This also implies $\langle k_z^2 \rangle \ll (\pi/W)^2$ (the infinite well limit), see Fig. 3.3(d), due to wave function penetration into the finite barriers. Thus, a change of density by a factor of ~ 2.5 changes $\beta_3/\beta_1 = \pi n/\langle 2k_z^2 \rangle$ by the same factor, resulting in a gate-tunable range of $0.08 \lesssim \beta_3/\beta_1 \lesssim 0.2$. In addition, quantum wells of width $W = 8$, 9.3, 11 and 13 nm were used [25, 119], resulting in a change of β_1 by roughly a factor of 2.

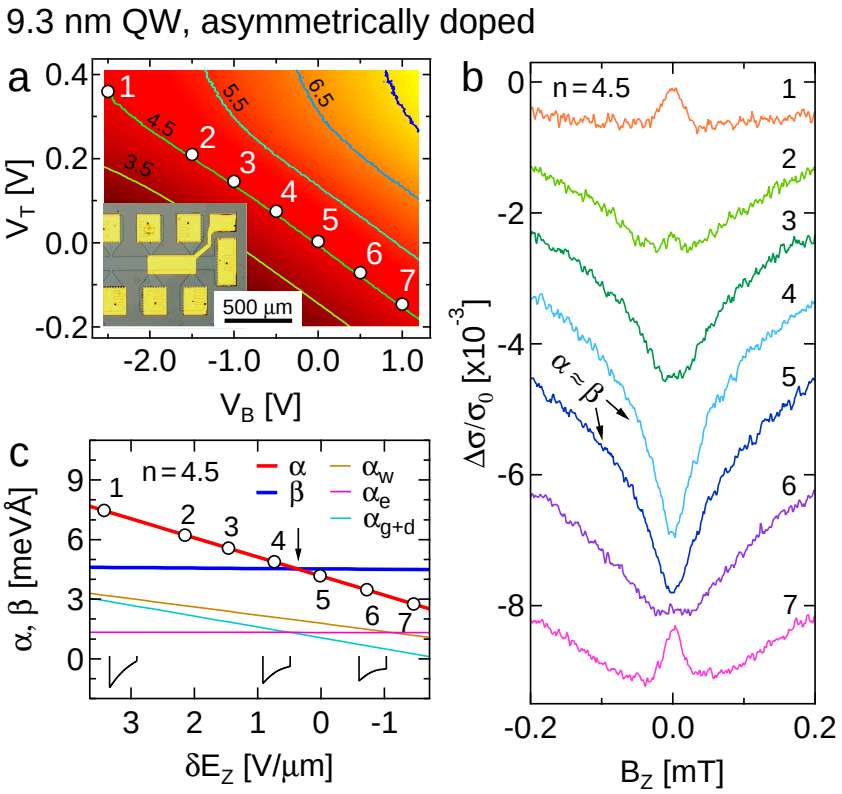

Figure 3.2: Weak localization (WL) as an $\alpha = \beta$ detector, gate control of Rashba α at constant density. **(a)** Measured charge density n (color) versus top gate voltage V_T and back gate voltage V_B (9.3-nm well). Contours of constant density $(3.5 - 7.5) \times 10^{11}\,\mathrm{cm}^{-2}$ are shown. Inset: Optical micrograph of typical Hall bar, with contacts (yellow), gate (center), and mesa (black lines). **(b)** Normalized longitudinal conductivity $\Delta\sigma/\sigma_0 = [\sigma(B_Z) - \sigma(0)]/\sigma(0)$ versus $B_Z \perp$ 2D plane. Curves for gate configurations $1 - 7$ along constant $n = 4.5 \times 10^{11}\,\mathrm{cm}^{-2}$ are shown (offset vertically), also labeled in **(a)** and **(c)**. **(c)** Simulated Rashba α and Dresselhaus β coefficients (see text) against gate-induced field change δE_Z, shown for constant $n = 4.5 \times 10^{11}\,\mathrm{cm}^{-2}$. The δE_Z axis – decreasing from left to right – corresponds exactly to the V_B abscissa of **(a)** for a covarying V_T, such that $n = 4.5 \times 10^{11}\,\mathrm{cm}^{-2}$ constant. Sketches of the well potential at 1, 4, and 6 illustrate the change of α with δE_Z. Note that $\alpha(\delta E_Z = 0) \neq 0$ since the external E-field (see SM) is not zero at $\delta E_Z = 0$.

3.3.3 Detection Scheme for Matched SO Couplings

WAL is a well-established signature of SO coupling in magnetoconductance $\sigma(B_Z)$ [37, 50, 72, 80, 93, 101] exhibiting a local maximum at zero field. In the $\pm\alpha = \beta$ regime, the resulting internal SO field is uniaxial, spin rotations commute and are undone along time-reversal loops. Therefore WAL is suppressed and the effectively spin less situation displaying weak localization [i.e., $\sigma(B_Z)$ exhibiting a local minimum at $B_Z = 0$] is restored [23, 24, 29, 50]. Away from the matched regime, the SO field is not uniaxial, spin rotations do not commute and trajectories in time-reversal loops interfere destructively upon averaging [72] due to the SO phases picked up along the loops thus leading to WAL. Hence this suppression is a sensitive detector for $\beta = \pm\alpha$. At high β_3, this detection scheme becomes approximate, giving $\beta \sim \pm\alpha$ [29]. We note that the WL dip – often used to determine phase coherence – sensitively depends on the SO coupling [e.g. curves 3-6 in Fig. 3.2(b)], even before WAL appears. Negligence of SO coupling could thus lead to spurious or saturating coherence times. At higher temperatures, when quantum coherence is lost, this detection scheme becomes inoperable, while it is expected that the mechanism for tuning both Rashba and effective Dresselhaus coefficients continues to function with only small corrections [44, 120] even up to room temperature. Also, note that Shubnikov-de Haas oscillations do not show any spin-orbit splitting here (see SM) given the strength of SO coupling in GaAs, making it clear that the quantum corrections in WAL and their suppression at the symmetry point present a very sensitive detector for SO coupling.

3.3.4 Continuous Locking $\alpha = \beta$

We proceed to demonstrate gate locking of the SO couplings α, β. Figure 3.2(b) displays $\sigma(B_Z)$ of the 9.3 nm-well for top gate and back gate configurations labeled 1-7, all lying on a contour of constant density; see Fig. 3.2(a). Along this contour, β is held fixed since the density is constant (β_1 is essentially gate independent), while α is changing as the gate voltages are modifying the electric field δE_Z perpendicular to the quantum well. Across these gate configurations, the conductance shows a transition from WAL (cf. 1 and 2) to

WL (4 and 5) back to WAL (7). Selecting the most pronounced WL curve allows us to determine the symmetry point $\alpha = \beta$. This scheme is repeated for a number of densities, varying n by a factor of 2, yielding the symmetry point $\alpha = \beta$ for each density n [see Fig. 3.3(a), blue markers], thus defining a symmetry line in the (V_T, V_B) plane. Along this line, β is changing with density, as previously described, and α follows β, remaining "continuously" locked at $\alpha = \beta$. As mentioned earlier, this is a very interesting finding, as it should allow the creation of persistent spin helices with gate-controllable pitches, as illustrated in Fig. 3.1.

Simulations and Fitting of γ. — Self-consistent calculations combined with the transport data can deliver all SO parameters. The numerical simulations [67] (see Appendix and SM) can accurately calculate α and $\langle k_z^2 \rangle$. This leaves only one fit parameter, γ, the bulk Dresselhaus coefficient, which can now be extracted from fits to the density dependence of the symmetry point, see solid blue line in Fig. 3.3(a), giving excellent agreement with the data (blue markers). This procedure can be repeated for a set of wafers with varying quantum well width and thus varying β_1. This shifts the symmetry point $\alpha = \beta$, producing nearly parallel lines, as indicated with colors in Fig. 3.3(a) corresponding to the various wafers as labeled. As shown, locking $\alpha = \beta$ over a broad range is achieved in all wafers. Since gate voltages can be tuned continuously, any and all points on the symmetry lines $\alpha = \beta$ can be reached. Again performing fits over the density dependence of the symmetry point for each well width, we obtain very good agreement, see Fig. 3.3(a), and extract $\gamma = 11.6 \pm 1\,\mathrm{eV\AA}^3$ consistently for all wells [Fig. 3.3(c)]. We emphasize that γ is notoriously difficult to calculate and measure [63, 93, 101]; the value we report here agrees well with recent studies [26, 63, 121]. Obtaining consistent values over wide ranges of densities and several wafers with varying well widths provides a robust method to extract γ.

Beyond γ, the simulations reveal important information about the gate tuning of the SO parameters. The Rashba coefficient is modeled as $\alpha = \alpha_{g+d} + \alpha_w + \alpha_e$ in the simulation, with gate and doping term α_{g+d}, quantum well structure term α_w, and Hartree term α_e.

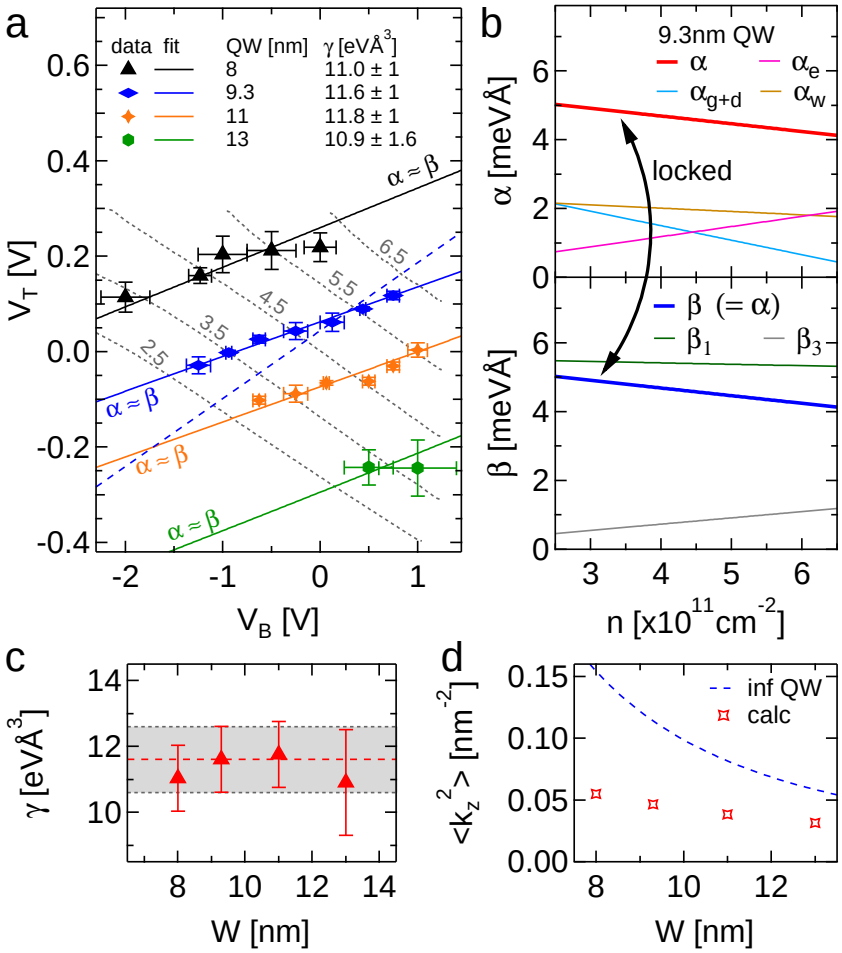

Figure 3.3: Tuning and continuously locking $\alpha = \beta$. **(a)** The markers indicate $\alpha \approx \beta$ for four different well widths (asymmetric doping) and various densities (gray contours of constant n, labeled in units of $10^{11}\,\mathrm{cm}^{-2}$) in the V_T and V_B plane. Error bars result from the finite number of conductance traces in the (V_B, V_T) space. Theory fits (solid lines) are shown for each well, with γ as the only fit parameter (inset table, error bars dominated by systematic error; see below). The dashed blue line indicates the slope of constant $\alpha = \beta_1$, neglecting β_3, which is inconsistent with the data. **(b)** Simulation of locked $\alpha = \beta$ versus density n along solid blue line from **(a)**, showing the various SO contributions (see text). **(c)** Values of γ from fits for each well width W. Red dashed line is the average $\gamma = 11.6 \pm 1\,\mathrm{eV\AA}^3$ (excluding $W = 13\,\mathrm{nm}$ due to its larger error), gray area is the $\sim 9\%$ error, stemming mostly from the systematic uncertainty in the input parameters of the simulations (see Appendix). **(d)** $\langle k_z^2 \rangle$ as a function of well width W for realistic (markers) and infinite (blue) potential.

Along a contour of constant density, the simulations show that mainly α_{g+d} and α_w are modified, while α_e and β remain constant; see Fig. 3.2(c). The density dependence for locked $\alpha = \beta$, on the other hand, shows that while β_1 is nearly constant, β_3 is linearly increasing with n, thus reducing $\beta = \beta_1 - \beta_3$; see Fig. 3.3(b). Hence, to keep $\alpha = \beta$ locked, α has to be reduced correspondingly. The Hartree term α_e, however, increases for growing n. Thus, on the $\alpha = \beta$ line, the other α-terms – mainly the gate- dependent α_{g+d} – are strongly reduced, maintaining locked $\alpha = \beta$, as shown in Fig. 3.3(b). We emphasize that neglecting the gate or density dependence of β_3 and fixing $\alpha = \beta_1 + \text{const.}$ results in a line with slope indicated by the blue dashed line in Fig. 3.3(a), which is clearly inconsistent with the data. Thus, the density-dependent β_3 enabling gate tunability of the Dresselhaus term is crucial here.

3.3.5 Dresselhaus Regime

We now show that α can be tuned through β *and through zero* in a more symmetrically doped wafer, opening the Dresselhaus regime $\beta \gg \alpha$. We introduce the magnetic field B_{SO}, where the magnetoconductance exhibits minima at $B_{\mathrm{Z1}} \approx -B_{\mathrm{Z2}}$. These minima describe the crossover between WAL and WL, where the Aharonov-Bohm dephasing length and the SO diffusion length are comparable. Beyond the WAL-WL-WAL transition [Fig. 3.4(b) upper panel], B_{SO} is seen to peak and decrease again (dashed curve). The gate voltages with maximal B_{SO} are added to Fig. 3.4(a) for several densities (red markers). We surmise that these points mark $\alpha \approx 0$: B_{SO} signifies the crossover between WL/WAL-like conductance, thus defining an empirical measure for the effects of SO coupling (larger B_{SO}, stronger effects). For $\alpha = 0$, the full effect of β on the conductance becomes apparent without cancellation from α, giving a maximal B_{SO}. Indeed, the simulated $\alpha = 0$ curve [dashed red line in Fig. 3.4(a)] cuts through the experimental points, also reflected in Fig. 3.4(c) by a good match with the simulated $\alpha = 0$ crossing point (red arrow).

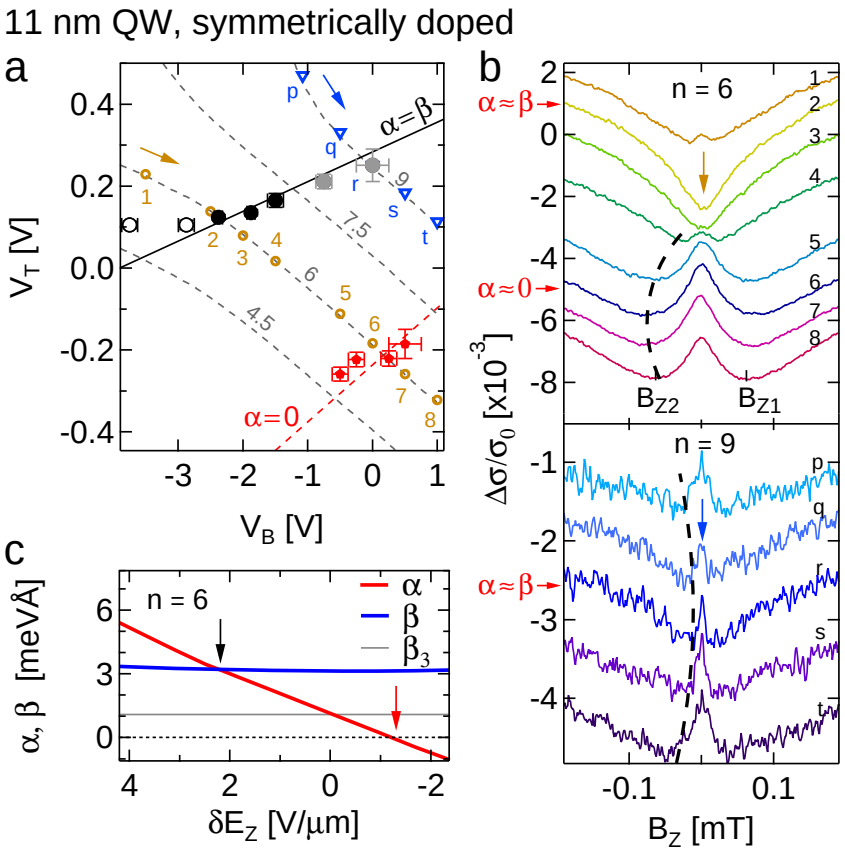

Figure 3.4: The Dresselhaus and the cubic regime. **(a)** Locked regime $\alpha \approx \beta$ (black or gray symbols) and Dresselhaus regime $\alpha \approx 0$ (red symbols) from the broadest WAL minima (maximal B_{SO}) in the V_T and V_B plane for a more symmetrically doped 11-nm well. The solid black line displays the $\alpha = \beta$ simulation, while the dashed red line marks the simulated $\alpha = 0$ contour. Open black markers (leftmost V_B) are entering the nonlinear gate regime, causing a slight deviation from theory, which assumes linear gate action. The rightmost V_B points (gray) are obtained from the minimal B_{SO} in the presence of WAL. **(b)** Sequence at $n = 6 \times 10^{11}\,\mathrm{cm}^{-2}$ (upper panel) and $n = 9 \times 10^{11}\,\mathrm{cm}^{-2}$ (lower panel), shifted vertically for clarity. Each brown/blue marker in **(a)** corresponds to a trace in **(b)**, as labeled by numerals or letters. B_{SO} is indicated as a guide for the eye by black dashed curves for negative B_Z. B_{SO} increases and peaks (indicating $\alpha = 0$) before decreasing again (upper panel). Broken spin symmetry regime (lower panel): WAL is no longer suppressed here due to symmetry breaking from the cubic term at large n. Still, $\alpha \approx \beta$ can be identified with the narrowest WAL peak. **(c)** Simulation of α and β along $n = 6 \times 10^{11}\,\mathrm{cm}^{-2}$. α traverses both β (black arrow) and for smaller δE_Z also zero (red arrow).

3.3.6 Diverging Spin-Orbit Lengths

For a comparison of experiment and simulation, we convert the empirical B_{SO} to a "magnetic length" $\lambda_{\mathrm{SO}} = \sqrt{\hbar/2eB_{\mathrm{SO}}}$, which we later on interpret as a spin-diffusion length, where $e > 0$ is the electron charge and the factor of 2 accounts for time-reversed pairs of closed trajectories. We also introduce the *ballistic* SO lengths $\lambda_{\pm} = \hbar^2/(2m^* |\alpha \pm \beta|)$. These lengths correspond to a spin rotation of 1 rad, as the electrons travel along $\hat{x}_+$ and $\hat{x}_-$, respectively, with spins initially aligned perpendicular to the corresponding SO field [e.g., for an electron moving along the $\hat{x}_+$ its spin should point along $\hat{x}_+$ or $\hat{z}$ so spin precession can occur, see SM (Eq. (3.27)), for an expression of the SO field]. For $\beta = +\alpha$, λ_- diverges (no precession, indicating that an electron traveling along $\hat{x}_-$ does not precess) while λ_+ is finite, and vice versa for $\beta = -\alpha$. An in-plane rotation of the PSH by a fixed angle $\pi/2$ from $\beta = +\alpha$ to $\beta = -\alpha$ was recently demonstrated [122].

Figure 3.5 shows the theoretical spin diffusion length λ_{eff} (see Appendix) and the ballistic $\lambda_{\pm}$, together with the experimental λ_{SO}, all agreeing remarkably well. Since at $\alpha = \beta$ spin transport is ballistic despite charge diffusion, λ_- and its diffusive counterpart λ_{eff} (small β_3) are essentially equivalent as shown in the SM. The enhanced λ_{SO} around $\alpha/\beta = 1$ corresponds to an increased spin relaxation time $\tau_{\mathrm{SO}} = \lambda_{\mathrm{SO}}^2/(2D)$. Note that $\max(\lambda_+, \lambda_-)$ quantifies the deviation from the *uniaxial* SO field away from $\alpha = \beta$, and thus the extent to which spin rotations are not undone in a closed trajectory due to the non-Abelian nature of spin rotations around noncollinear axes. This leads to WAL, a finite B_{SO} and $\lambda_{\mathrm{SO}} \simeq \max(\lambda_+, \lambda_-)$, as observed (see Fig. 3.5). Unlike the corresponding time scales, the SO lengths are only weakly dependent on density and mobility when plotted against α/β, allowing a comparison of various densities.

The third harmonic contribution of cubic-in-k term causes spin relaxation even at $\alpha = \beta$ and becomes visible at large densities: WAL is present in all traces and through $\alpha = \beta$ [Fig. 3.4(b), lower panel], because the SO field can no longer be made uniaxial, thus breaking spin symmetry and reviving WAL. A partial symmetry restoration is still apparent, where – in contrast to the $\alpha = 0$ case – a *minimal* B_{SO} is reached (dashed curves) con-

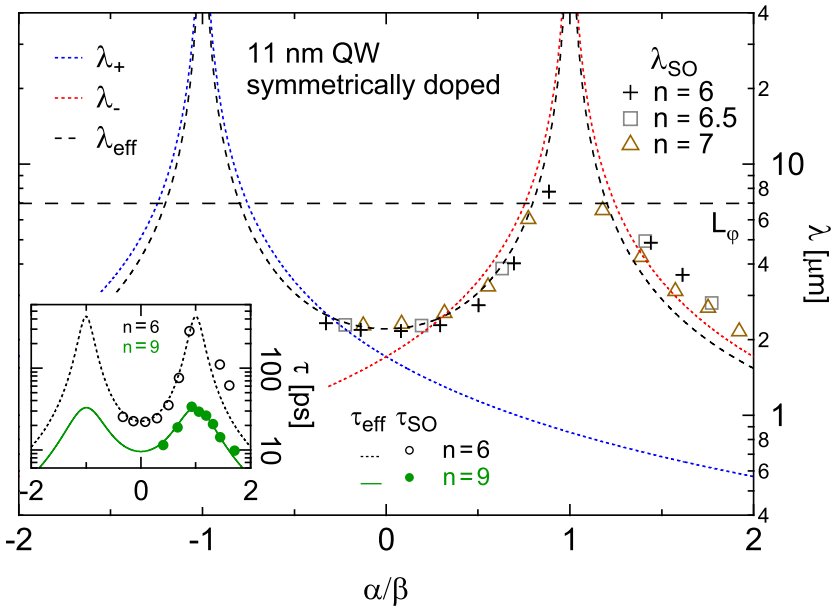

Figure 3.5: Experimental and theoretical SOl lengths and SO times. Experimental $\lambda_{\mathrm{SO}} = \sqrt{\hbar/2eB_{\mathrm{SO}}}$ (markers, densities as labeled, in units of $10^{11}\,\mathrm{cm}^{-2}$) as a function of the dimensionless ratio α/β (from SO simulation). The ballistic $\lambda_{\pm}$ (blue and red dashes) and effective λ_{eff} (black dashed curve) are only weakly n dependent (small β_3) when plotted against α/β. Thus, curves for only one density ($n = 6 \times 10^{11}\,\mathrm{cm}^{-2}$) are shown. The experimental uncertainty on λ_{SO} is captured by the spread given by the three slightly different densities. The coherence length $L_\varphi \approx 7\,\mu$m is added for illustration (obtained from WL curves), setting the visibility of SO effects on the conductance and thus the width of the WAL-WL-WAL transition. Inset: Experimental spin relaxation time $\tau_{\mathrm{SO}} = \lambda_{\mathrm{SO}}^2/(2D)$ (circles) as a function of α/β for two densities as indicated. Theory curves τ_{eff} (dashed) now include the symmetry-breaking third-harmonic term, preventing divergence at $\alpha/\beta = 1$, while λ_{eff} (main panel) does not.

sistent with $\alpha = \beta$ [gray markers Fig. 3.4(a) at large n]. We include the cubic β_3 in the spin-relaxation time τ_{eff} (see Appendix), shown in the inset of Fig. 3.5 for two densities, finding good agreement with the experimental $\tau_{\text{SO}} = \lambda_{\text{SO}}^2/(2D)$, where D is the diffusion constant. Over the whole locked regime of Fig. 3.3(b), WAL is absent, and τ_{SO} is enhanced between 1 and 2 orders of magnitude compared to $\alpha = 0$. Finally, the coherence length L_φ sets an upper limit for the visibility of SO effects: WAL is suppressed for $\lambda_{\text{eff}} \gg L_\varphi$, setting the width of the WAL-WL-WAL transition (see SM).

3.4 Final Remarks and Outlook

This work is laying the foundation for a new generation of experiments benefiting from unprecedented command over SO coupling in semiconductor nanostructures such as quantum wires, quantum dots, and electron spin qubits. Moreover, our work relaxes the stringency (i.e., the "fine-tuning") of the $\alpha = \beta$ symmetry condition at a particular singular point (gate) by introducing a "continuous locking" of the SO couplings $\alpha(V_T, V_B) = \beta(V_T, V_B)$ over a wide range of voltages, which should enable new experiments exciting persistent spin helices with variable pitches in GaAs wells [25, 26], i.e., *stretchable PSHs*. Further, this concept is also applicable to a range of other III-V semiconductors in various suitable configurations. Another possibility is the generation of a Skyrmion lattice (crossed spin helices) with variable lattice constants, as recently proposed in Ref. [123].

Finally, we stress that within the continuously locked regime of SO couplings we demonstrate in our study, SO-coupled quantum transport in our samples shows a very distinctive feature: it is diffusive (2D) for charge while ballistic (1D) for spins, thus providing a unique setting for coherent spin control. This ultimately adds a new functionality to the nonballistic spin transistor of Ref. [23]; i.e., it can now be made to operate as the ideal (ballistic) Datta-Das spin transistor – but in a realistic 2D diffusive system, with yet controlled spin rotations protected from spin decay.

3.4.1 Acknowledgements

We would like to thank A. C. Gossard, D. Loss, D. L. Maslov and G. Salis for valuable inputs and stimulating discussions. This work was supported by the Swiss Nanoscience Institute (SNI), NCCR QSIT, Swiss NSF, ERC starting grant, EU-FP7 SOLID and MICROKELVIN, U.S. NSF and ONR, Brazilian grants FAPESP, CNPq, PRP/USP (Q-NANO), and natural science foundation of China (Grant No. 11004120). F.D., J.F., P.J.W., J.C.E., and D.M.Z. designed the experiments, analyzed the data and co-wrote the paper. All authors discussed the results and commented on the manuscript. S.M. and D.D.A. designed, simulated, and carried out the molecular beam epitaxy growth of the heterostructures. F.D. processed the samples and with P.J.W. performed the experiments. J.F. and J.C.E. developed and carried out the simulations and theoretical work.

3.5 Appendix: Materials and Methods

GaAs quantum well materials. — The wells are grown on an n-doped substrate (for details see SM) and fabricated into Hall bar structures [see inset, Fig. 3.2(a)] using standard photolithographic methods. The 2D gas is contacted by thermally annealed GeAu/Pt Ohmic contacts, optimized for a low contact resistance while maintaining high back gate tunability (low leakage currents) and avoiding short circuits to the back gate. On one segment of the Hall bar, a Ti/Au top gate with dimensions of $300 \times 100\,\mu m^2$ was deposited. The average gate-induced E-field change in the well is defined as $\delta E_Z = 1/2\,(V_T/d_T - V_B/d_B)$, with effective distance $d_{T/B}$ from the well to the top gate or back gate, respectively, extracted using a capacitor model, consistent with the full quantum description (see SM). Contours of constant density follow $\delta V_T/d_T = -\delta V_B/d_B$. Deviations from linear behavior appear at most positive or negative gate voltages due to incipient gate leakage and hysteresis.

Low-temperature electronic measurements. — The experiments are performed in a dilution refrigerator with base temperature 20 mK. We use a standard four-wire lock-in technique at 133 Hz and 100 nA current bias, chosen to avoid self-heating while maximizing the signal. The density is determined with Hall measurements in the classical regime, whereas Shubnikov-de Haas oscillations are used to exclude occupation of the second subband, which is the case for all the data we discuss. The WAL signature is a small correction (10^{-3}) to total conductance. To achieve a satisfactory signal-to-noise ratio, longitudinal conductivity traces $\Delta\sigma/\sigma_0 = [\sigma(B) - \sigma(0)]/\sigma(0)$ are measured at least 10 times and averaged.

Numerical simulations. — The simulations calculate the Rashba coefficient α and $\langle k_z^2 \rangle$ based on the bulk semiconductor band parameters, the well structure, the measured electron densities, and the measured gate lever arms. We solve the Schrödinger and Poisson equations self-consistently ("Hartree approximation"), obtain the self-consistent eigenfunctions, and then determine α via appropriate expectation values [67]. The Dresselhaus coefficient γ is extracted from fits of the simulation to the experiment, which detects the absence of WAL at $\alpha = \beta = \gamma(\langle k_z^2 \rangle - k_F^2/4)$. Thus, given α and $\langle k_z^2 \rangle$ from the simulation and the measured $n = k_F^2/(2\pi)$, we obtain $\gamma = 11.6 \pm 1\,\mathrm{eV\AA}^3$ consistently for all asymmetrically doped wells. Taking into account the uncertainties of the band parameters, the experimental errors and a negligible uncertainty on $\langle k_z^2 \rangle$, an overall uncertainty of about 9%-10% or about $\pm 1\,\mathrm{eV\AA}^3$ on γ results. About 1%-2% error originates from the experimental uncertainty of determining $\alpha = \beta$. The doping distribution (above or below well) is not expected to influence γ, and hence we use the same γ for the more symmetrically doped wafer. Fits to the $\alpha = \beta$ experimental points then determine how much charge effectively comes from upper rather than lower doping layers, fixing the last unknown parameter also for the more symmetrically doped well (see SM).

Spin-dephasing times and lengths. — In WL or WAL measurements, additional spin-dephasing is introduced by the external magnetic field B via the Aharonov-Bohm

phase arising from the magnetic flux enclosed by the time-reversed trajectories: $\Delta\varphi = 2eAB/\hbar$, where A is the loop area. Here we take $A = \lambda_{\rm SO}^2 = 2D\tau_{\rm SO}$ as a characteristic "diffusion area" probed by our WL or WAL experiment, with $\tau_{\rm SO}$ being the spin-dephasing time, and $\lambda_{\rm SO}$ the spin diffusion length. By taking $\Delta\varphi = 1$ (rad) at $B = B_{\rm SO}$, we can extract the spin-diffusion length $\lambda_{\rm SO}$ and spin-dephasing time $\tau_{\rm SO}$ from the minima of the WAL curves from $\lambda_{\rm SO} = \sqrt{\hbar/2eB_{\rm SO}}$ and $\tau_{\rm SO} = \hbar(4eDB_{\rm SO})^{-1}$, respectively. The factor of 4 here stems from the two time-reversed paths and the diffusion length.

Effective SO times and lengths. — Theoretically, we determine $\tau_{\rm SO}$ via a spin random walk process [D'yakonov-Perel (DP)]. The initial electron spin in a loop can point (with equal probability) along the s_{x_-}, s_{x_+}, and s_z axes (analogous to x_+, x_-, and z, respectively), which have unequal spin-dephasing times $\tau_{\rm DP,s_{x_-}}$, $\tau_{\rm DP,s_{x_+}}$, and $\tau_{\rm DP,s_z}$. For unpolarized, independent spins, we take the average $\tau_{\rm eff} = (\tau_{\rm DP,s_{x_-}} + \tau_{\rm DP,s_{x_+}} + \tau_{\rm DP,s_z})/3$, which leads to an effective spin-diffusion length $\lambda_{\rm eff} = \sqrt{2D\tau_{\rm eff}}$. Actually, $\lambda_{\rm eff}$ is defined from the average variance $\lambda_{\rm eff}^2 = \bar{\sigma}^2 = 2D\tau_{\rm eff}$, obtained by averaging the spin-dependent variances $\sigma_{s_{x_-}}^2 = 2D\tau_{\rm DP,s_{x_-}}$, $\sigma_{s_{x_+}}^2 = 2D\tau_{\rm DP,s_{x_+}}$ and $\sigma_{s_z}^2 = 2D\tau_{\rm DP,s_z}$ over the spin directions s_{x+}, s_{x-}, and s_z (this is equivalent to averaging over the τ's and not over $1/\tau$'s). In the SM, we discuss the spin random walk and provide expressions for the DP times including corrections due to the cubic β_3 term. Figure 3.5 shows curves for the spin-dephasing times and lengths presented here. In the main panel, the cubic β_3 is neglected in $\lambda_{\rm eff}$ since for $n \leq 7 \times 10^{11}\,{\rm cm}^{-2}$, WL appears at $\alpha = \beta$ (small β_3). In contrast, the cubic term is included in $\tau_{\rm eff}$ in the inset since at the higher density $n = 9 \times 10^{11}\,{\rm cm}^{-2}$, WAL persists (sufficiently strong β_3).

3.6 Supplementary Information

3.6.1 Wafer Structure: Details

The quantum well (QW) samples are grown on (001) n-doped substrates, serving as a back gate, with total distance of 1210 nm between back gate and QW, including 600 nm of low-

temperature (LT) grown GaAs, see Fig. 3.6. The LT GaAs creates a barrier by pinning the Fermi level midgap [124]. Thus, in a simple plate capacitor model, the effective distance d_B between QW and back gate is reduced by the thickness of the LT barrier, increasing

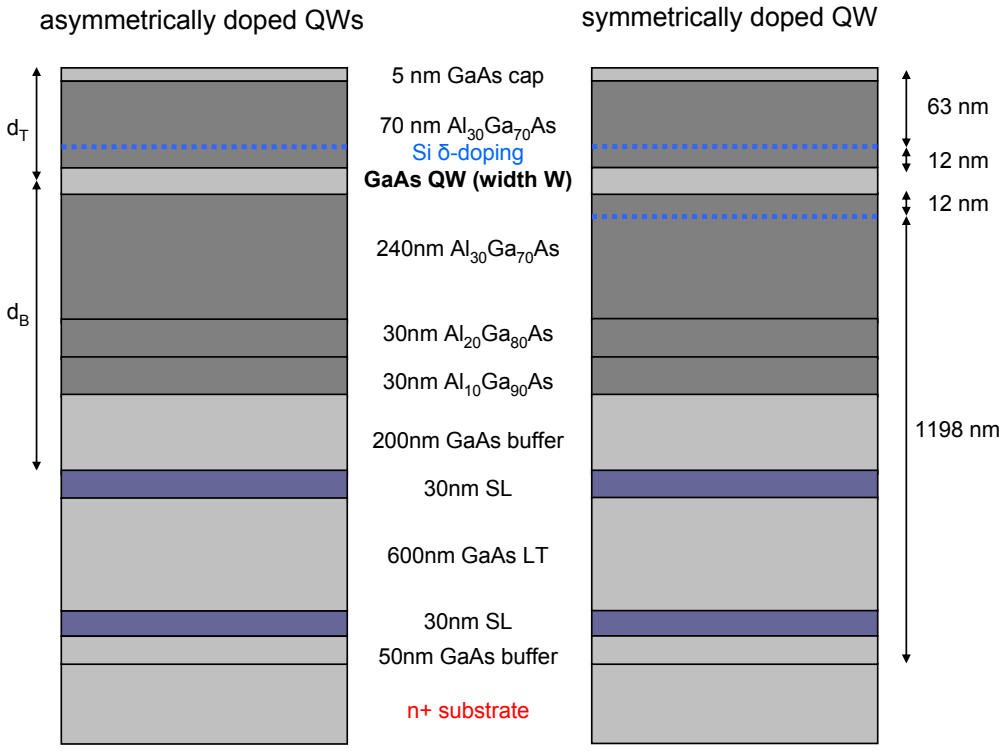

Figure 3.6: Quantum well wafer profiles. MBE growth profiles of the asymmetrically (left) and more symmetrically (right) doped QW wafers. The GaAs QW width W is $8, 9.3, 11$ and 13 nm for the asymmetric and 11 nm for the symmetric QW, respectively.

the range of tunability and reducing leakage currents at the same time. Similarly, d_T is defined as the distance between QW and top gate. Good agreement is found between $d_{B/T}$ extracted from the measured back/top gate dependence of the carrier density and the as-grown thicknesses of the layers in the QW structure. The QWs are 75 nm below the surface with a setback of 12 nm to the Si δ-doping layer above the well for the asymmetric QWs with $W = 8, 9.3, 11$ and 13 nm and an additional doping layer 12 nm below the 2DEG for the more symmetric 11 nm QW.

Using top and back gates, the density is tunable typically in a range of $n \approx 2$ - $8 \cdot 10^{11}$ cm^{-2} (Fig. 3.7a) corresponding to mobilities $\mu \approx 2$ - 20 m^2/(Vs) (Fig. 3.7b). Tunability is limited

by onset of gate leakage and hysteresis issues. For positive $V_T > 300\,\mathrm{mV}$ and large negative $V_B < -2\,\mathrm{V}$, a non-linear gate dependence is observed. Shubnikov-de Haas measurements indicate that all data in this study are in the single 2D subband regime, consistent with the numerical simulations. In section 3.6.9 we show a more detailed analysis of the Shubnikov-de Haas oscillations. For low densities $n \lesssim 2 \cdot 10^{11}\,\mathrm{cm}^{-2}$, WAL as a signature of SO coupling becomes very weak or disappears due to the small wave number $k_F^2 = 2\pi n$. At even lower densities the electrons become strongly localized by disorder. Hence the lower left corners of Fig. 3.7a) and b) corresponding to low densities are not displayed.

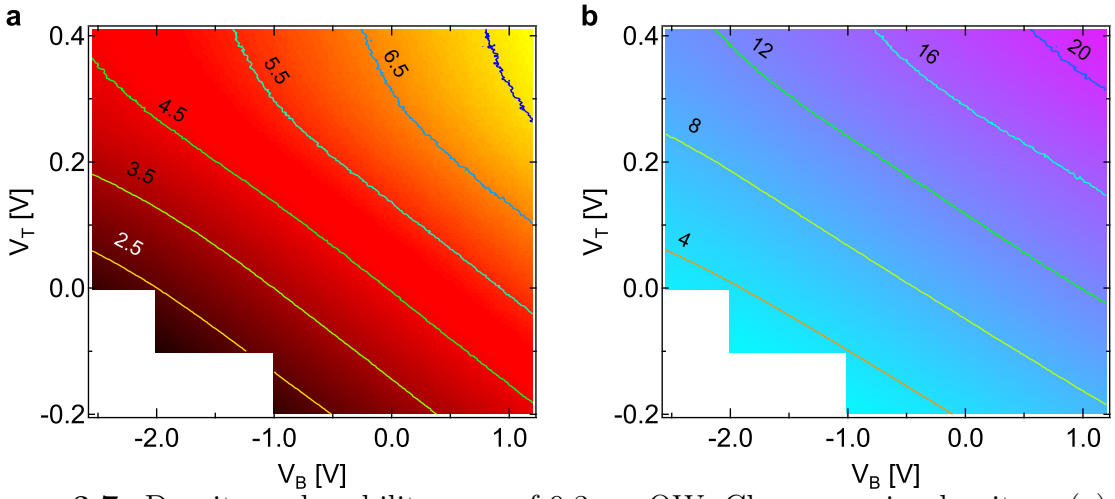

Figure 3.7: Density and mobility map of 9.3 nm QW. Charge carrier density n (a) and mobility μ (b) as a function of top gate voltage V_T and back gate voltage V_B. Contour lines are labeled in units of $10^{11}\,\mathrm{cm}^{-2}$ (a) and $\mathrm{m}^2/(\mathrm{Vs})$ (b), respectively. The lower left corner was omitted due to a general lack of WAL at low n.

3.6.2 Temperature Dependence

Elevated temperatures suppress quantum corrections to conductivity, as shown in Fig. 3.8. The magnetic field position B_{SO} of the MC minima, however, appears not affected by temperature (dashed line in Fig. 3.8), consistent with a spin-orbit (SO) length λ_{SO} independent of T. At elevated temperatures, WAL and the B_{SO} minima are shallower and eventually can disappear, due to loss of coherence. This leads to a broadening of the WAL-WL-WAL transition with increasing temperature, i.e. the size of the gate voltage range where WAL is suppressed grows with increasing temperature, see Fig. 3.9 from left

to right. Thus, in absence of symmetry breaking effects of the higher harmonic β_3, the phase coherence defines the width of the WAL-WL-WAL transition in our experiment.

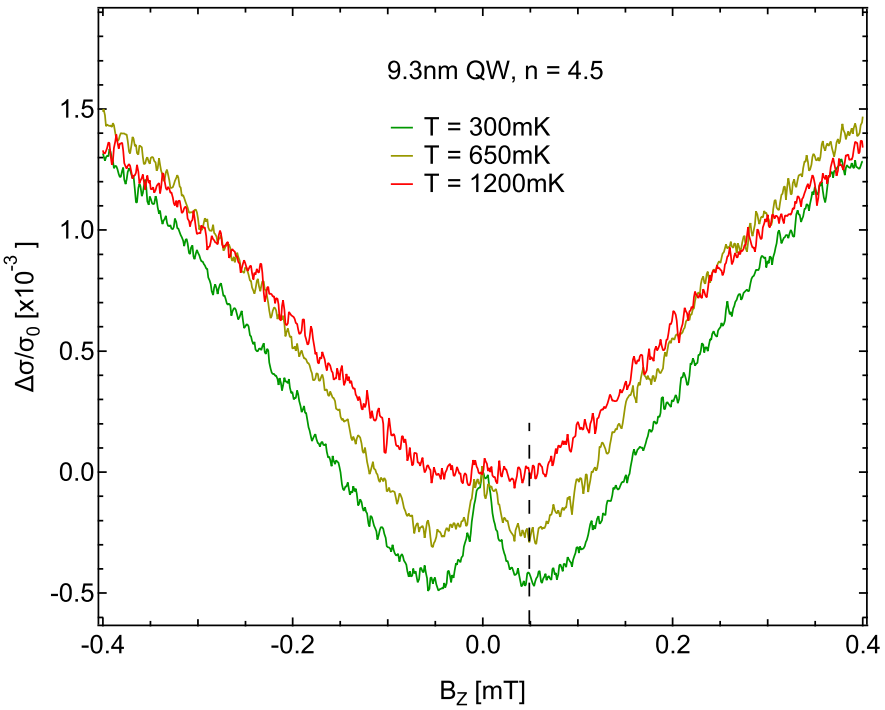

Figure 3.8: Temperature dependence of WAL. Magnetoconductance for a specific gate configuration (9.3 nm QW, $n = 4.5 \cdot 10^{11}\,\mathrm{cm}^{-2}$, $V_T = -146\,\mathrm{mV}$, $V_B = 1\,\mathrm{V}$) showing clear WAL signature at $T = 300\,\mathrm{mK}$ (green). The WAL maximum at $B_Z = 0$ weakens for $T = 650\,\mathrm{mK}$ (olive), and essentially disappears at $T = 1200\,\mathrm{mK}$ (red). The position of the MC minima (defined as B_{SO}) appears to be not affected by temperature (dashed vertical line).

3.6.3 Numerical Simulations

Self-consistent approach and potential. The confining potential of our GaAs/$Al_{0.3}Ga_{0.7}As$ wells (see Fig. 3.10) contains [67]: (i) the structural part V_{w} arising from the band offset at the interfaces, (ii) the potential V_{g} from the top and back gates, which allows us to adjust the symmetry of the well profile and the electronic densities while keeping the chemical potential μ constant, (iii) the doping potential V_{d}, which remains fixed at low temperatures (we also use $V_{\mathrm{g+d}} = V_{\mathrm{g}} + V_{\mathrm{d}}$), and (iv) the electronic Hartree potential V_{e} which depends on carrier density. The 3D electron charge density in the well ρ_{e} depends on the total potential $V_{\mathrm{sc}} = V_{\mathrm{w}} + V_{\mathrm{g+d}} + V_{\mathrm{e}}$, which in turn

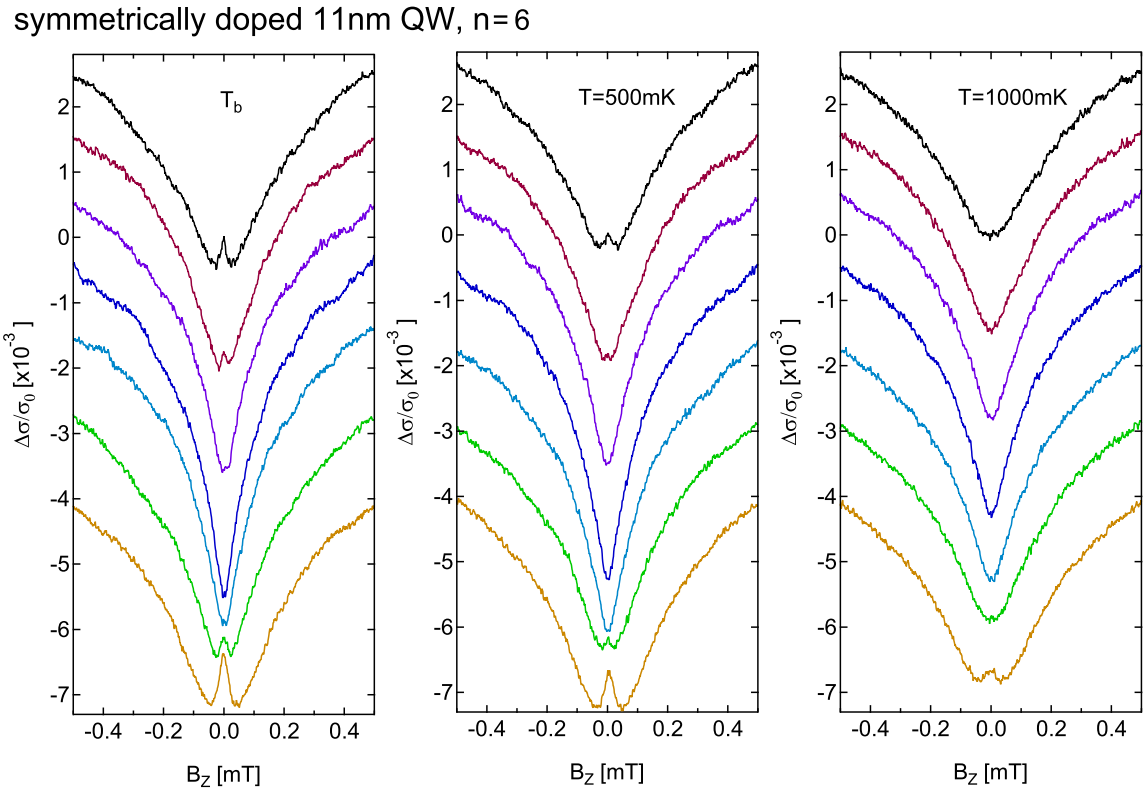

Figure 3.9: Temperature dependence of WAL-WL-WAL transition of the more symmetrically doped 11 nm QW, shown for base temperature (left panel), 500 mK (middle panel) and 1 K (right panel) for various (V_T, V_B) configurations (color coded) at constant density $n = 6 \cdot 10^{11}\,\mathrm{cm}^{-2}$. The curves are shifted vertically for clarity. Upon increasing T, WAL weakens and finally disappears on both sides of the low-T symmetry point (see e.g. green and dark brown curve), resulting in a widening of the transition.

depends on ρ_e via the Hartree term. Hence to find the eigensolutions of the system, we solve the Schrödinger equation for electrons in the total potential $V_\mathrm{sc} = V_\mathrm{w} + V_\mathrm{g+d} + V_e$. Both V_w and $V_\mathrm{g+d}$ depend only on the z variable (growth direction). Within the Hartree approximation, the electron charge density is $\rho_e(z,\vec{r}) = 2\sum_{\nu,\vec{k}} |\varphi_{\nu,\vec{k}}(z,\vec{r})|^2 f_{k,\nu}$, where $\varphi_{\nu,\vec{k}}(z,\vec{r}) = \frac{1}{\sqrt{A}} \exp(i\vec{k}\cdot\vec{r})\psi_\nu(z)$ with $\psi_\nu(z)$ being the ν^th subband wave function of the well, $\vec{k}$ the in-plane electron wave vector, A a normalizing area, and $f_{k,\nu}$ the Fermi-Dirac distribution. Note that within the Hartree approximation, $\rho_e(z,\vec{r}) \to \rho_e(z)$ because of the plane-wave dependence of the wave function in the xy-plane and hence the Hartree potential V_e depends only on z.

Upon summing over $\vec{k}$, $\rho_e(z)$ simplifies to $\rho_e(z) = \sum_\nu |\psi_\nu(z)|^2 n_\nu$, with the electron occupation of the ν^th subband $n_\nu = \frac{m^*}{\pi\hbar^2} k_B T \ln[1 + \exp(\mu - \mathcal{E}_\nu)/k_B T]$ and confinement energy

$\mathcal{E}_\nu$. Here μ is the electron chemical potential, k_B the Boltzmann constant and T the absolute temperature. The areal electron density n in the well and $\rho_e(z)$ are related via $n = \int dz \rho_e(z) = \sum_\nu n_\nu$. We then solve the resulting one-dimensional Schrödinger equation together with the Poisson's equation for the total charge density $\rho_{\rm tot}(z) = \rho_e(z) + \rho_{\rm d}(z)$, where $\rho_{\rm d}(z)$ denotes the ionized donor concentration profile. We obtain the subband energies $\mathcal{E}_\nu$ and wave functions $\psi_\nu(z)$ iteratively within this self consistent procedure when convergence is attained.

The potential profile and the corresponding wave function for the 9.3 nm well based on our self-consistent scheme are shown in Fig. 3.10 for top and back gates set to $V_T = 75\,\text{mV}$ and $V_B = -500\,\text{mV}$, respectively, corresponding to point 4 in Fig. 3.2 of the main text.

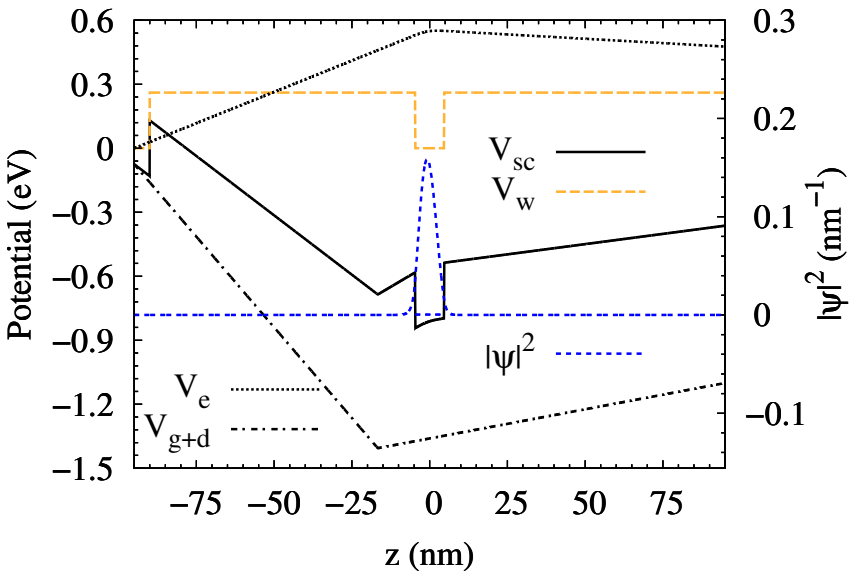

Figure 3.10: Self-consistent potential $V_{\rm sc}$ and the corresponding wave function Ψ for our GaAs/$Al_{0.3}Ga_{0.7}$As 9.3 nm quantum well with the top gate $V_T = 75\,\text{mV}$ and back gate $V_B = -500\,\text{mV}$. The QW band offset potential $V_{\rm w}$, the electron Hartree potential $V_{\rm e}$ and the gate plus doping potential $V_{\rm g+d}$ are also shown. The first subband energy level is $\mathcal{E}_1 = -776.0\,\text{meV}$ (indicated by solid green line inside QW), i.e. 16.4 meV below the Fermi energy (not shown), which is pinned at $-759.6\,\text{meV}$ (i.e., the mid gap energy in bulk GaAs). The resulting carrier density is $n = 4.5 \cdot 10^{11}\text{cm}^{-2}$. Note that the origin of the abscissa is in the center of the well and the wafer surface is located slightly farther away than specified in the growth profile (see also Fig. 3.6) due to the lever arm measured in the experiment.

Expressions for the SO coupling terms. *Rashba spin-orbit coupling* α. As shown

in Ref. [67], the strength α of the Rashba coupling can be cast as the expectation value $\langle ... \rangle$ of the weighted derivatives of the potential contributions (i)-(iv) above:

$$\alpha = \eta_{\rm w} \langle \partial_z V_{\rm w} \rangle + \eta_{\rm H} \langle \partial_z V_{\rm e} \rangle + \eta_{\rm H} \langle \partial_z V_{\rm g+d} \rangle, \tag{3.1}$$

with

$$\eta_{\rm w} = \frac{P^2}{3} \left(\frac{\delta_{\rm v}/\delta_{\rm c}}{E_g^2} - \frac{\delta_\Delta/\delta_{\rm c}}{(E_g + \Delta_{\rm w})^2} \right), \tag{3.2}$$

and

$$\eta_{\rm H} = -\frac{P^2}{3} \left(\frac{1}{E_g^2} - \frac{1}{(E_g + \Delta_{\rm w})^2} \right), \tag{3.3}$$

which involve the bulk quantities of the well layer, such as the band gap E_g and the usual Kane parameters Δ ("spin orbit") and P, in addition to the potential offsets $\delta_{\rm i}$, $i = {\rm c, v}, \Delta$ (e.g., in Fig. 3.10 $V_{\rm w} = \delta_c[\Theta(W/2 - z) + \Theta(z - W/2)]$ for a well of width W centered at $z = 0$; here $\Theta(z)$ is the Heaviside function. See also Fig. 3.10 and Sec. (III.E) below for a further discussion of these parameters). Even though $\alpha = \alpha_{\rm w} + \alpha_{\rm e} + \alpha_{\rm g+d}$ comprises seemingly independent contributions, we note that each of these $\alpha_{\rm w}$, $\alpha_{\rm e}$, and $\alpha_{\rm g+d}$ does depend on all four potentials (i)-(iv) via the self-consistent wave function used in the expectation values. In particular, they all change as we vary the gates (top and back), which allows us to fine tune α and thus attain the $\alpha = \beta$ regime when the Dresselhaus term is considered.

We emphasize that the Rashba coefficient α can be rewritten in terms of an "external" electric field $E_{\rm ext} = E_{\rm gate} + E_{\rm d} + E_{\rm e}$, where we have defined $E_{\rm gate} = \frac{1}{e}\langle \partial_z V_{\rm g} \rangle$, $E_{\rm d} = \frac{1}{e}\langle \partial_z V_{\rm d} \rangle$, and $E_{\rm e} = \frac{1}{e}\langle \partial_z V_{\rm e} \rangle$ with $e > 0$ the elementary charge. Since the total force on a bound state is zero (Ehrenfest's theorem), *i.e.*, $\langle \partial_z V_{sc} \rangle = \langle \partial_z (V_{\rm w} + V_{\rm e} + V_{\rm g} + V_{\rm d}) \rangle = 0$, one has the relation of α with $E_{\rm ext}$,

$$\alpha = (\eta_{\rm H} - \eta_{\rm w}) e E_{\rm ext}. \tag{3.4}$$

Now let us turn to the change of α due to a variation of $E_{\rm ext}$, i.e. a variation δV_T of the top gate voltage and/or a variation δV_B of the back gate voltage, giving $\delta\alpha =$

$e(\eta_{\rm H}-\eta_{\rm w})(\delta E_{\rm gate}+\delta E_{\rm d}+\delta E_{\rm e})$. In our model, the variation $\delta E_{\rm d}\simeq 0$ since the doping potential does not vary with the gates. Furthermore, in the case of constant density (as shown in Figs. 2c and 4c of the main text), we also have $\delta E_{\rm e}\simeq 0$ since the rearrangement of the *quantum mechanical* distributions of electrons in the gate range we studied is negligible. Therefore, to keep the carrier density n unchanged when we tune the gates, we have $\delta\alpha\simeq e(\eta_{\rm H}-\eta_{\rm w})\delta E_{\rm gate}$. Note that in the main text of the paper (and in Figs.3.2 and 3.4c), we use the notation of $\delta E_z=\delta E_{\rm gate}$ to describe the change of electric field along the growth direction due to the gates.

Dresselhaus spin-orbit couplings β_1 and β_3. The linear β_1 and cubic β_3 coefficients of the Dresselhaus well Hamiltonian arise from the expectation value of the bulk cubic Dresselhaus Hamiltonian [13]. Using our self-consistent electron wave functions, we obtain $\beta_1=-\gamma\langle\partial_z^2\rangle$ and $\beta_3=\gamma k_F^2/4$, where γ is the bulk Dresselhaus parameter and k_F the Fermi wave vector. To a very good approximation the Fermi contours are essentially circles and hence can be approximated by the 2D free electron result $k_F\simeq\sqrt{2\pi n}$, with n being the areal electron density, and $\beta_3\simeq\gamma\pi n/2$.

Input from the experiment. Input for our simulations are mainly based on the experimental conditions:

1. The chemical potential is pinned at mid gap in GaAs ($=-759.60\,\text{meV}$) [124].

2. The top gate voltage V_T and back gate voltage V_B enter the numerical calculation as boundary conditions when solving the Poisson's equation for $V_g(z)$, *i.e.*, $V_g(-d_T)=-eV_T$ and $V_g(d_B)=-eV_B$ with the coordinate origin being chosen as the center of the well, which amounts to a linear external gate potential $V_g(z)=-e\left[V_T+\frac{(V_B-V_T)}{d_B+d_T}(z+d_T)\right]$. The gate lever arms, *i.e.*, the d_T and d_B values, are taken from the experiment and are close to the nominal values from the wafer growth profile.

3. We model the delta-doping regions in our samples by considering monolayer-thick doped regions with an effective ionized areal doping density ρ^{eff} used in the simulation, distinct from the nominal doping ρ^{nom} specified in the MBE growth.

In the asymmetrically doped wafers, the effective doping density ρ^{eff} is chosen so that the areal electron density $n(V_T, V_B)$ in the QW matches the measured values for all gate voltages using the experimentally determined gate lever arms. We find a donor ionization efficiency $\rho^{\text{eff}}/\rho^{\text{nom}}$ of about 50% for all asymmetric wafers. We need to introduce the effective doping density ρ^{eff} because the simulation does not include effects such as partial absorption of donor electrons e.g. by positive background doping or DX centers, resulting in partial ($\sim 50\%$) rather than full ionization of donors.

In the more symmetrically doped wafer, in contrast to the asymmetric ones, we have two δ-doping layers: an upper layer above the QW with effective doping $\rho_{\text{u}}^{\text{eff}}$ and a lower layer below the QW with effective doping $\rho_{\text{l}}^{\text{eff}}$. The effective doping asymmetry ratio $r = \rho_{\text{l}}^{\text{eff}}/\rho_{\text{u}}^{\text{eff}}$ modifies the Rashba coefficient α by changing the electric field across the QW. In the experiment, we detect the $\alpha = \beta$ regime (absence of WAL), where $\beta \propto \gamma$. Thus, r and with it the simulated α will directly affect the extracted γ. There is no reason to have a γ for the symmetrically doped QW that is different from the asymmetrically doped, but otherwise identical QW. Thus, we choose the doping asymmetry r by requiring that the Dresselhaus parameter γ take on the same value $\gamma = 11.6\,\text{eVÅ}^3$ as for all the asymmetric wafers, while choosing $\rho_{\text{u}}^{\text{eff}}$ to maintain the measured charge density in the QW. Here, we obtain $\rho_{\text{u}}^{\text{eff}} \sim 0.61 \cdot \rho_{\text{u}}^{\text{nom}}$ and $r \sim 0.3$, i.e., about three times more doping from above than from below the QW.

We note that the QW electron density n is significantly smaller than the total effective ionized doping $\rho^{\text{eff}} = \rho_{\text{u}}^{\text{eff}} + \rho_{\text{l}}^{\text{eff}}$, e.g. $n \sim 5 \cdot 10^{11}\,\text{cm}^{-2}$ versus $\rho^{\text{eff}} \sim 15 \cdot 10^{11}\,\text{cm}^{-2}$. Due to the close proximity of the QW to the surface and to the interface with the LT GaAs barrier, a large fraction of the ionized donor electrons will populate surface and interface states, rather than the QW. This results in strong band bending at the surface and LT interface, lowering the QW energy below the chemical potential and allowing populate

the QW with electrons.

Fit of the Dresselhaus parameter γ. With our self-consistent calculation of α and $\langle k_z^2 \rangle$ we can determine a so-called γ-map, which gives contours in the V_B and V_T space where the condition $\alpha = \gamma(\langle k_z^2 \rangle - \frac{1}{4}k_F^2)$ is full filled. We fit our symmetry points (where $\alpha \approx \beta$) to this map and extract an effective value of $\gamma = 11.6\text{eVÅ}^3$. In Fig. 3.10 we show our experimentally determined symmetry points and the fit to these, as well as contours with similar values for γ. Our extracted value of γ is clearly in good agreement with the data, since the other values of γ would require symmetry points at different values of V_B and V_T.

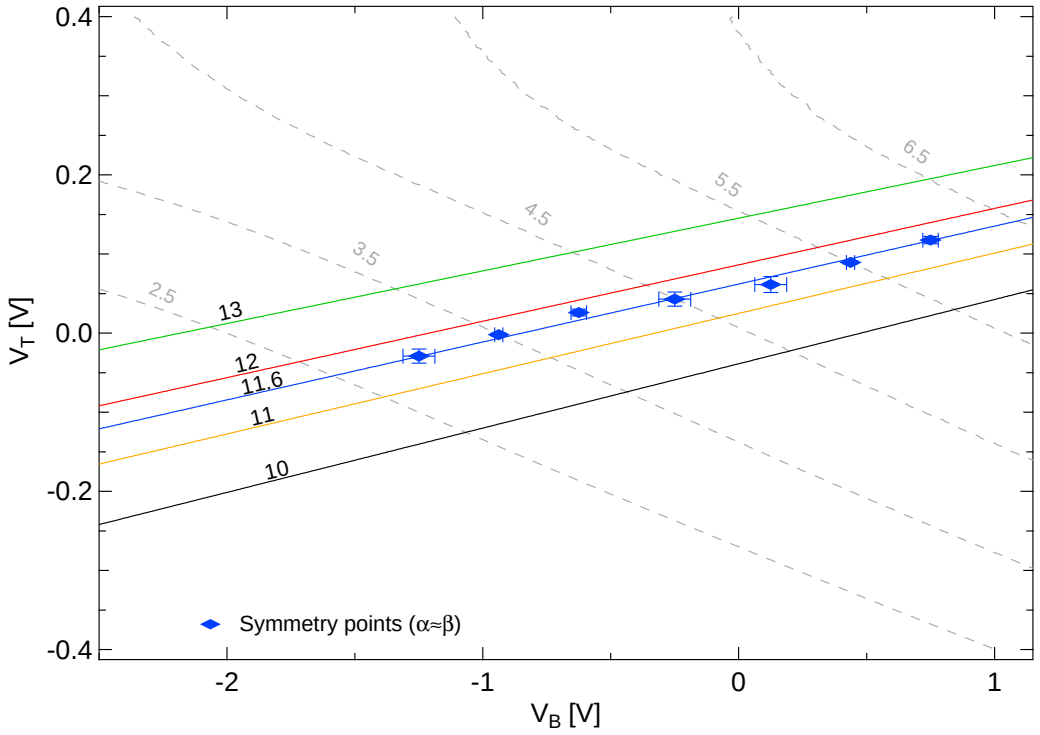

Figure 3.11: γ-map. Contours of various values for γ for the 9.3nm wafer and the determined symmetry points with their fit. The value of γ is indicated at each contour in units of eVÅ^3

3.6.4 Gate Voltages and Contours of Constant Density

We will now describe the effect of the gate voltages within a quantum mechanical model and compare the results to that of a simple classical plate capacitor model.

Quantum mechanical description. Here we treat the variation $\delta V_g^T(z)$ due to a change of top gate voltage δV_T and the variation $\delta V_g^B(z)$ due to a change of back gate voltage δV_B as a perturbation and obtain the first order correction to the lowest subband energy, $\delta\mathcal{E}_1 = \delta\mathcal{E}_1^T + \delta\mathcal{E}_1^B$ with

$$\delta\mathcal{E}_1^T = \langle\psi^0|\delta V_g^T(z)|\psi^0\rangle = -e\frac{d_B - \langle\psi^0|z|\psi^0\rangle}{d_B + d_T}\delta V_T, \tag{3.5}$$

and

$$\delta\mathcal{E}_1^B = \langle\psi^0|\delta V_g^B(z)|\psi^0\rangle = -e\frac{d_T + \langle\psi^0|z|\psi^0\rangle}{d_B + d_T}\delta V_B, \tag{3.6}$$

where ψ^0 is the envelope function in absence of $\delta V_g^T(z)$ and $\delta V_g^B(z)$, and d_T (d_B) the top (back) gate lever arms. Notice that in all our wafers the well width $W \ll d_T(d_B)$, which ensures $\langle\psi^0|z|\psi^0\rangle \ll d_T(d_B)$ since ψ^0 is mostly confined in the well (if ψ^0 is symmetric with respect to the center of the well, i.e., in a symmetric wafer, $\langle\psi^0|z|\psi^0\rangle$ is always zero). Therefore we have

$$\delta\mathcal{E}_1^T \simeq -e\frac{d_B}{d_B + d_T}\delta V_T, \qquad \delta\mathcal{E}_1^B \simeq -e\frac{d_T}{d_B + d_T}\delta V_B. \tag{3.7}$$

The resulting change of carrier density δn can be straightforwardly written as

$$\delta n = -\frac{m^*}{\pi\hbar^2}(\delta\mathcal{E}_1^T + \delta\mathcal{E}_1^B) = \frac{m^*}{\pi\hbar^2}e\left(\frac{d_B}{d_B + d_T}\delta V_T + \frac{d_T}{d_B + d_T}\delta V_B\right). \tag{3.8}$$

Note that this change of density considers only the response to changes of the gate voltages and neglects the resulting change of the self-consistent Hartree potential. When the self-consistent Hartree potential is also included, the resulting gate lever arm is identical to the lever arm obtained in the plate capacitor model (see below) and reproduces the

experimentally measured density changes very well. On a contour of constant density, the Hartree potential is essentially constant in the voltage range considered here, and thus drops out. From Eq. 3.8, a constant density results for $\delta V_T/d_T = -\delta V_B/d_B$. Furthermore, the change of electric field for constant density is

$$\delta E_z = \frac{\delta V_T - \delta V_B}{d_T + d_B} = \frac{\delta V_T + \delta V_T \frac{d_B}{d_T}}{d_T + d_B} = \frac{\delta V_T}{d_T}\frac{d_T + d_B}{d_T + d_B} = \frac{\delta V_T}{d_T} = -\frac{\delta V_B}{d_B}. \tag{3.9}$$

Classical plate capacitor model. Based on a simple plate capacitor model, a variation of top gate δV_T and back gate δV_B induces a change of carrier density δn^T and δn^B, respectively,

$$\delta n^T = \frac{\epsilon\epsilon_0}{e}\frac{\delta V_T}{d_T}, \qquad \delta n^B = \frac{\epsilon\epsilon_0}{e}\frac{\delta V_B}{d_B}, \tag{3.10}$$

which also agrees very well with the measured gate effect. To ensure a constant density when varying the top and back gates, i.e., $\delta n^T + \delta n^B = 0$, we obtain, $\delta V_T/d_T = -\delta V_B/d_B$, identical to the expression from the quantum mechanical description. Furthermore, the change of average electric field on the left and right of the 2DEG plate is $\delta E_\mathrm{z} = 1/2(\delta V_T/d_T - \delta V_B/d_B)$. On a contour of constant density, this again becomes $\delta E_\mathrm{z} = \delta V_T/d_T = -\delta V_B/d_B$, as before in the quantum description. For simplicity, we use $\delta E_\mathrm{z} = 1/2(V_T/d_T - V_B/d_B)$, i.e. using the actual applied gate voltages, rather than only changes of voltages, as a practical choice of the origin of E_z, e.g. for Figs. 3.3c) and 3.5c) (main text).

3.6.5 Estimate of the Error Bars in the Rashba Coupling due to the Uncertainties in Input Parameters

The Rashba coupling strength α is more sensitive to the band parameters, especially to the band offsets of the quantum well (see expression for α above), than the Dresselhaus β_1, which in our phenomenological description solely depends on the well confinement via the wave function. Therefore, to extract a reliable γ based on the condition $\alpha = \beta$ (locked $\alpha = \beta$ regime or absence of WAL), it is essential to assess how sensitive the Rashba

coupling is to the band parameters.

A sketch of the conduction and valence-band offsets for our GaAs/$Al_{0.3}Ga_{0.7}As$ quantum well is shown in Fig. 3.10, where the relevant bulk parameters are indicated. The commonly accepted band gap in GaAs at low temperature is 1.519 eV [43, 125–128], and the band gap in $Al_{0.3}Ga_{0.7}As$ is 1.951 ± 0.006 eV [126]. The main offsets of a GaAs/$Al_{0.3}Ga_{0.7}A$ quantum well, δ_c (electrons) and δ_v (heavy and light holes), are taken from literature with uncertainties of about 2% [126]. We obtain the split-off hole offset δ_Δ straightforwardly through the relation, $\delta_\Delta = \delta_v + \Delta_b - \Delta_w$ with Δ_w (Δ_b) the split-off gap in the well (barrier), see Fig. 3.10 and Table 3. The split-off gap Δ_b of the barrier is obtained from linear interpolation of the GaAs and AlAs values [127]. From the uncertainties in δ_v, Δ_b and Δ_w, one can evaluate the error bar of δ_Δ [129].

Another crucial quantity determining the Rashba α is the Kane parameter P (see Eq. 1-3), usually expressed via the quantity $E_P = 2m_0P^2/\hbar^2$ (see e.g. Ref. [127]), with m_0 the bare electron mass. We take E_P for GaAs from the widely accepted values quoted by Hermann and Weisbuch [130] (see also [127]), who extracted this parameter via a detailed fitting procedure involving both the effective mass and the g factor. In their fitting, an error of effective mass and g factor less than 1% has been assumed. As pointed out by Vurgaftman *et al.* in their classic review Ref. [127], other estimates of E_P with smaller errors seem to have internal inconsistencies. The band parameters and Kane parameter E_P used in the simulations and their corresponding errors are summarized in Table 3.

Table 3: Main relevant parameters for the Rashba coupling. The unit is in eV

	Δ_b(AlAs)	Δ_w(GaAs)	Δ_b($Al_{0.3}Ga_{0.7}As$)
Value	0.30[a,e] (0.28[c])	0.341[a–f] (0.340[h])	0.329[c]
Error	0.02 (6.7%)	0.001 (0.3%)	0.007 (2%)

	δ_c	δ_v	δ_Δ	E_P
Value	0.261[b]	0.171[b]	0.159[f]	28.9[c,g]
Error	0.003 (1.2%)[b]	0.003 (1.8%)[b]	0.01 (6.3%)[f]	0.9 (3.1%)[c,g]

[a]Ref. [125], [b]Ref. [126], [c]Ref. [127],[d]Ref. [128], [e]Ref. [43], [f]Ref. [129], [g]Ref. [130], and [h]Ref. [131].

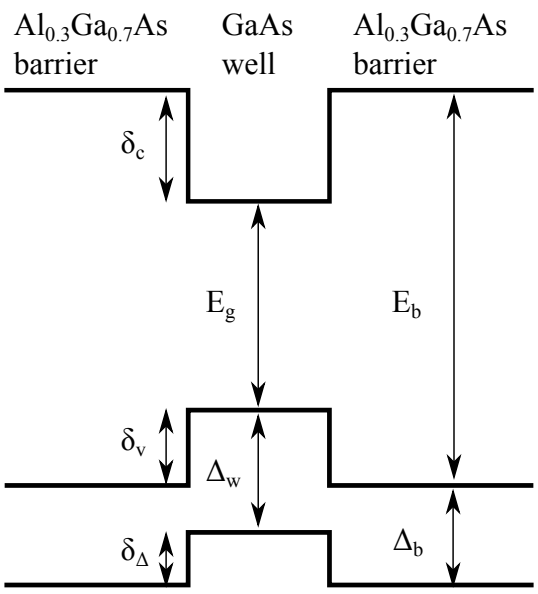

Figure 3.12: Schematic of the band offsets for GaAs/AlGaAs well. E_g (E_b) and Δ_w (Δ_b) are the fundamental band gap and the split-off gap in the well (barrier), respectively. δ_i ($i = c, v, \Delta$) denote the corresponding band offsets: δ_c for conduction band, δ_v for heavy hole (and light hole) , and δ_Δ for split-off hole.

With all these parameters and the corresponding errors at hand, we can now evaluate the Rashba coefficient α and its uncertainty. The α coefficient for our 9.3 nm well as a function of back gate is shown in Fig. 3.13, where we vary both the top and back gates so that the curve follows a constant density, $n = 4.5 \cdot 10^{11}\,\mathrm{cm}^{-2}$. The α plotted here actually corresponds to the one shown in Fig. 2c (red solid curve) of the paper. The error bar of α for several values of the back gate is also shown in Fig. 3.13.

The resulting error of α is found to be $\sim 8\%$, with two dominating contributions, $\sim 4\%$ from the uncertainty of the band parameters and $\sim 3\%$ from the Kane parameter P. The remaining $\sim 1\%$ error of α arises from the uncertainty of the measured carrier density, the effective lever arms, and the resulting uncertainty of the doping efficiency ($\rho^{\mathrm{eff}}/\rho^{\mathrm{nom}}$). This error analysis holds for all wafers used in this study. Note that to determine γ (Fig. 2c), we use the error bars arising from experimental uncertainty ($1 - 2\%$) only, not taking into account the 13 nm wafer data due to its significantly larger error bar (using three data points from the 8, 9.3 and 11 nm wafers in Fig. 2c). We then add the larger systematic error, resulting in a total error on γ of about $9 - 10\%$ or $\pm 1\mathrm{eV\AA}^3$. Finally, we note that the γ extracted from the 13 nm wafer is also consistent with this γ-value.

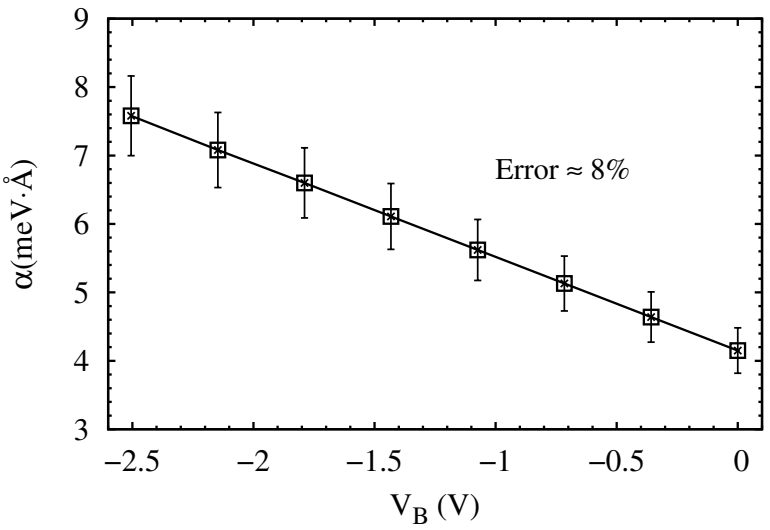

Figure 3.13: Error bar on the calculated Rashba coefficient α. Rashba coupling strength α as a function of V_B on a contour of constant density $n = 4.5 \cdot 10^{11}\,\mathrm{cm}^{-2}$ for the 9.3 nm QW and corresponds to the α curve (the red solid curve) in Fig. 1c. The error bar due to the uncertainty in input parameters for several values of back gate is also shown. The error is about 8%.

3.6.6 Interface Dresselhaus and Random Rashba SO Couplings

Below we introduce other possible factors that could possibly affect our results, including the interface Dresselhaus [44] and random Rashba SO couplings [48, 117, 132].

Interface Dresselhaus term. In addition to the *usual* Dresselhaus term arising from bulk inversion asymmetry, in heterostructures and QWs, there is also an extra contribution to the Dresselhaus coupling due to the interfaces. The general form of linear Dresselhaus term in QWs reads [44],

$$\mathcal{H}_D = -\langle \partial_z \gamma(z) \partial_z \rangle (\sigma_y k_y - \sigma_x k_x) = (\beta_u + \beta_{int})(\sigma_y k_y - \sigma_x k_x), \tag{3.11}$$

where $\beta_u \equiv -\langle \gamma(z) \partial_z^2 \rangle$ is the usual Dresselhaus coefficient, $\beta_{int} \equiv -\langle \gamma_{int}(z) \partial_z \rangle$ the contribution due to the interfaces of the QW, and $\gamma(z)$ characterizes the z dependence of the bulk Dresselhaus parameter, which depends on the material present at position z (e.g. GaAs or AlGaAs). Also, $\langle\rangle$ stands for the expectation value with respect to the ground

state wave function $\psi(z)$. We have

$$\gamma(z) = \gamma_b[\Theta(-z - W/2) + \Theta(z - W/2)] + \gamma_w\Theta(W/2 - |z|)$$
$$\gamma_{int}(z) = \gamma_b[-\delta(z + W^-/2) + \delta(z - W^+/2)] + \gamma_w[\delta(z + W^+/2) - \delta(z - W^-/2)],$$

with γ_w and γ_b as the bulk Dresselhaus parameter in the well and barrier layers, respectively, Θ the Heaviside step function, and $W^\pm = \lim_{\delta\to 0} W \pm \delta$ with W standing for the well width. Note that $\beta_1 \sim -\gamma_w\langle\partial_z^2\rangle$ for weak wave function penetration into the barriers. The interface Dresselhaus coefficient can be written in a more expanded form [44],

$$\begin{aligned}\beta_{int} &= -\int \psi^*(z)\gamma_{int}(z)\partial_z\psi(z) = \gamma_b\left[\psi\left(-\frac{W}{2}\right)\psi'\left(-\frac{W^-}{2}\right) - \psi\left(\frac{W}{2}\right)\psi'\left(\frac{W^+}{2}\right)\right] \\ &\quad +\gamma_w\left[\psi\left(\frac{W}{2}\right)\psi'\left(\frac{W^-}{2}\right) - \psi\left(-\frac{W}{2}\right)\psi'\left(-\frac{W^+}{2}\right)\right], \qquad (3.12)\end{aligned}$$

with $\psi'(z)$ the first derivative of the wave function. From Eq. 3.12, it is straightforward to obtain the interface Dresselhaus coefficient in structurally symmetric QWs as a special case, with $\beta_{int} = 2\psi(W/2)[\gamma_w\psi'(W^-/2) - \gamma_b\psi'(W^+/2)]$. Note that β_{int} in general is nonzero even in symmetric QWs, in contrast to the Rashba term, which vanishes in systems with no structural inversion asymmetry.

To estimate the size of the interface Dresselhaus term, we determine β_{int} through our self-consistent calculation. For completeness, we consider our wells of both asymmetric and symmetric doping configurations, corresponding to asymmetric 9.3 nm and 11 nm wells and symmetric 11 nm well. Note that the exact value of the bulk Dresselhaus parameter γ is controversial in both theory and experiment, and its value in GaAs ranges from 8.5 to 30 eVÅ^3[44, 125]. To proceed, we take our value $\gamma_w = 11.6$ eVÅ^3 for our self-consistent calculation, and determine how β_{int} depends on γ_b [133]. We find that β_{int} essentially has a linear dependence on γ_b, as shown in Fig. 3.14. A sign reversal of β_{int} at $\gamma_b \sim 8.5$ eVÅ^3, is attributed to the interplay of the quantities γ_w, γ_b, and $\psi'(z)$ (Eq. 3.12), with $\psi'(z)$ obeying the condition of $(1/m_w)\psi'(W^-/2) = (1/m_b)\psi'(W^+/2)$ and $(1/m_w)\psi'(-W^+/2) = (1/m_b)\psi'(-W^-/2)$ at the two interfaces, respectively. Here m_w

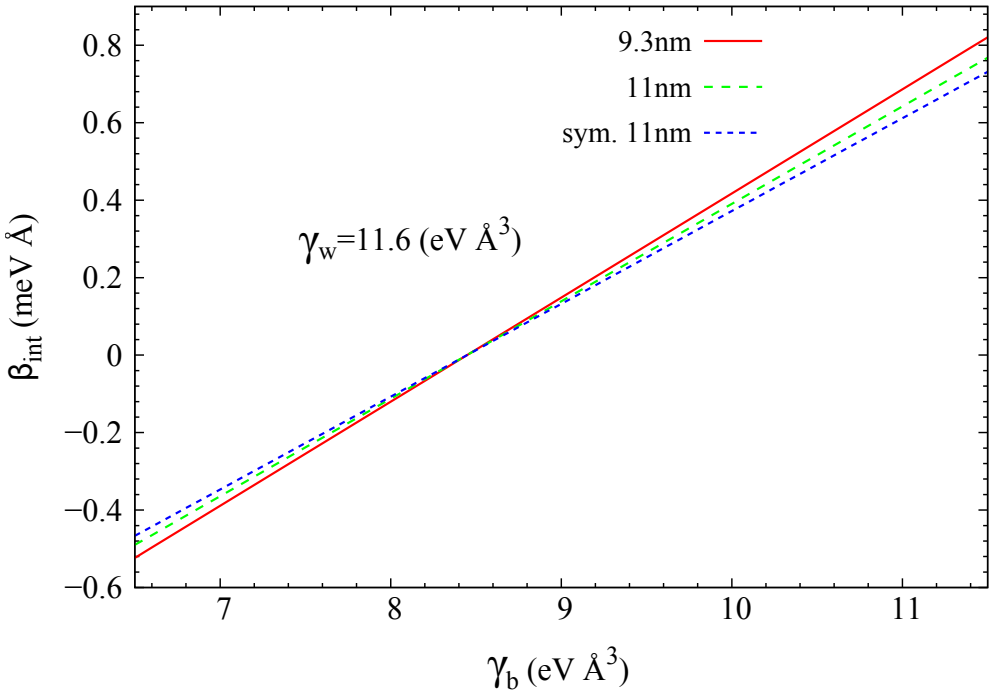

Figure 3.14: Interface Dresselhaus coefficient β_{int} as a function of γ_b at $\gamma_w = 11.6$ eVÅ^3, for the asymmetric 9.3 nm well, the asymmetric 11 nm well, and symmetric 11 nm well, respectively. The range of γ_b plotted here is based on a similar reduction of the γ_b value from its $\mathbf{k}\cdot\mathbf{p}$ value as the reduction of γ_w from its $\mathbf{k}\cdot\mathbf{p}$ value [133].

(m_b) is the effective electron mass in the GaAs ($Al_{0.3}Ga_{0.7}As$) layer[134]. Note that here we do not consider the spin-dependent matching at the interface, the effect of which was found negligible in medium-size band-gap semiconductors such as GaAs [42].

Though β_{int} appears at least a factor of 5-10 smaller in magnitude than β_u and may thus be negligible, we emphasize that this estimate of the interface Dresselhaus coefficient is speculative, since (i) the value γ_b for $Al_{0.3}Ga_{0.7}As$ is not available and (ii) the evaluation of γ_b from $\mathbf{k}.\mathbf{p}$ theory is not reliable. Note that we find $\gamma_w \sim 11.6$ eVÅ^3 for GaAs, more than a factor of two smaller than the value (~ 27 eVÅ^3) [43, 44] from $\mathbf{k}.\mathbf{p}$ calculations. Since the usual Dresselhaus term and the interface term have the same SO form, Eq. 3.11, the interface term simply gets absorbed in a changed value of γ which we extract from the experiment. However, in absence of a reliable value of γ_b in $Al_{0.3}Ga_{0.7}As$, the estimate only gives a very broad range for β_{int} (incl. a sign change of β_{int}, see Fig. 3.14), we cannot determine how much the extracted value of γ is affected. To our knowledge, $\beta_{\rm int}$ was not quantified in other work studying the SO terms [25, 26, 51]. Further work is needed in

the future to study the interface term, especially in very narrow QWs where the effect is expected to be large.

Random Rashba term. Fluctuations of the concentration of dopant ions could lead to a random electric field along the growth direction of QWs [132], and hence a random Rashba coupling [48, 49, 117, 132, 135]. Our recent self-consistent calculations showed that the averaged random Rashba strength α_R in GaAs QWs, similar to our wafers here, is around one order of magnitude smaller than the linear Rashba α term, i.e., $\alpha_R \sim 0.1\alpha$ [123]. Furthermore, we found that at the $\alpha = \beta$ point the random Rashba spin relaxation rate is more then 20 times smaller than relaxation due to the cubic Dresselhaus term, indicating a negligible effect of the random Rashba term in our QWs [123]. For more detailed discussions about the random Rashba term in GaAs wells and in other systems in which the random Rashba coupling could possibly become important, see Ref. [123].

3.6.7 Effective Spin-Orbit Magnetic Field

For a 001-grown GaAs well, the linear-in-the-wave-vector SO term contains both the Rashba and Dresselhaus contributions

$$H_{\mathrm{SO}}^{(1)} = \alpha(k_x\sigma_y - k_y\sigma_x) + \beta_1(k_y\sigma_y - k_x\sigma_x), \tag{3.13}$$

with α and $\beta_1 = \gamma\langle k_z^2\rangle$ the linear Rashba and ("bare") Dresselhaus coefficients, respectively, and $k_{x,y}$ the electron wave vector along the $\hat{x}||[100]$ and $\hat{y}||[010]$ directions. The cubic (in k) Dresselhaus term reads

$$H_{\mathrm{SO}}^{(3)} = \gamma(k_x k_y^2\sigma_x - k_y k_x^2\sigma_y). \tag{3.14}$$

Equations 3.13 and 3.14 can be rewritten in terms of sin/cos functions of ϕ (1st harmonic) and 3ϕ (3rd harmonic) with ϕ the polar angle between k and x axis. The linear term has

only the first harmonic contribution

$$H_{\rm SO}^{(1)} = k\Big\{[\alpha\cos(\phi)+\beta_1\sin(\phi)]\sigma_y - [\alpha\sin(\phi)+\beta_1\cos(\phi)]\sigma_x\Big\}, \tag{3.15}$$

while the cubic term contributes to both the first and third harmonics,

$$H_{\rm SO}^{(3)} = k\Big\{\beta_3[\cos(\phi)-\cos(3\phi)]\sigma_x - \beta_3[\sin(\phi)+\sin(3\phi)]\sigma_y\Big\}, \tag{3.16}$$

with $\beta_3 = \gamma k^2/4$ the cubic Dresselhaus coefficient.

Rotating the reference frame. For convenience, we further rewrite the above equations in the rotated coordinate system The $\hat{x}_+||[110]$ and $\hat{x}_-||[\bar{1}10]$. The linear SO term becomes

$$\begin{aligned}\mathcal{H}_{\rm SO}^{(1)} &= (-\alpha+\beta_1)k_-\sigma_+ + (\alpha+\beta_1)k_+\sigma_- \\ &= k\Big[(-\alpha+\beta_1)\sin(\theta)\sigma_+ + (\alpha+\beta_1)\cos(\theta)\sigma_-\Big],\end{aligned} \tag{3.17}$$

while the cubic term reads

$$\begin{aligned}\mathcal{H}_{\rm SO}^{(3)} &= \frac{\gamma}{2}(k_+^2-k_-^2)(k_-\sigma_+ - k_+\sigma_-) \\ &= k\Big\{\beta_3[\sin(3\theta)-\sin(\theta)]\sigma_+ - \beta_3[\cos(3\theta)+\cos(\theta)]\sigma_-\Big\},\end{aligned} \tag{3.18}$$

with θ the polar angle in the rotated coordinate system, i.e., the angle between k and x_+ axis. From Eqs. 3.17 and 3.18, one has all the first- and third-harmonic terms,

$$\begin{aligned}\mathcal{H}_{\rm SO} &= \mathcal{H}_{\rm SO}^{(1)} + \mathcal{H}_{\rm SO}^{(3)} \\ &= k\Big\{[(-\alpha+\beta)\sin(\theta)+\beta_3\sin(3\theta)]\sigma_+ + [(\alpha+\beta)\cos(\theta)-\beta_3\cos(3\theta)]\sigma_-\Big\},\end{aligned} \tag{3.19}$$

with $\beta = \beta_1 - \beta_3$ the renormalized "linear" Dresselhaus coefficient. Note that here $\beta = \beta_1 - \beta_3$ implying that part of the cubic Dresselhaus term ($\mathcal{H}_{\rm SO}^{(3)}$) renormalizes the linear

parameter β_1 thus altering the condition for attaining the regime of matched SO strength (or absence of WAL) from $\alpha = \beta_1$ to $\alpha = \beta$. With the approximation (main text) $\beta_3 \simeq \gamma\pi n/2$, which neglect the small anisotropy of the Ferm wave vector, this renormalization renders the Dresselhaus coupling β density dependent thus providing a means to gate-tune β and attain the "dynamical" locking $\alpha = \beta$ over a wide range of gate voltages, as described in the main text (see Fig. 3.3b)). The remaining part of the cubic term (third harmonic) breaks the angular symmetry of the SO terms and is detrimental to the protection from relaxation.

Effective SO magnetic fields. It is convenient to reexpress the spin-orbit Hamiltonian $\mathcal{H}_{\rm SO}$ in a compact form, i.e, in terms of an effective magnetic field $\mathbf{B}_{\rm RD}(\mathbf{k})$ due to the Rashba and Dresselhaus terms,

$$\mathcal{H}_{\rm SO} = \frac{1}{2} g\mu_{\rm B} \mathbf{B}_{\rm RD}(\mathbf{k}) \cdot \sigma, \tag{3.20}$$

with g the electron g-factor in the well, μ_B the Bohr magneton and

$$\mathbf{B}_{\rm RD}(\mathbf{k}) = \mathbf{B}^{(1)}_{\rm RD}(\mathbf{k}) + \mathbf{B}^{(3)}_{\rm RD}(\mathbf{k}), \tag{3.21}$$

$$\mathbf{B}^{(1)}_{\rm RD}(\mathbf{k}) = \frac{2}{g\mu_{\rm B}} k \left[(-\alpha + \beta)\sin(\theta)\hat{x}_+ + (\alpha + \beta)\cos(\theta)\hat{x}_-\right], \tag{3.22}$$

and

$$\mathbf{B}^{(3)}_{\rm RD}(\mathbf{k}) = \frac{2}{g\mu_{\rm B}} k \left[\beta_3 \sin(3\theta)\hat{x}_+ - \beta_3 \cos(3\theta)\hat{x}_-\right], \tag{3.23}$$

where $\mathbf{B}^{(1)}_{\rm RD}(\mathbf{k})$ and $\mathbf{B}^{(3)}_{\rm RD}(\mathbf{k})$ are the first- and third-harmonic SO fields, respectively. [80, 136] Note that within the approximation $\beta_3 \simeq \gamma\pi n/2$ both $\mathbf{B}^{(1)}_{\rm RD}(\mathbf{k})$ and $\mathbf{B}^{(3)}_{\rm RD}(\mathbf{k})$ are linear in k. In addition, observe that for matched SO couplings $\alpha = \pm\beta$, $\mathbf{B}^{(1)}_{\rm RD}(\mathbf{k})$ is unidirectional, i.e., its direction in real space is k independent, while $\mathbf{B}^{(3)}_{\rm RD}(\mathbf{k})$ has a k-dependent direction (through 3θ), as can be seen in Eqs. (3.22) and (3.23), respectively. As discussed in the main text, the third harmonic contribution of the cubic Dresselhaus term is detrimental to spin protection because its resulting effective field $\mathbf{B}^{(3)}_{\rm RD}(\mathbf{k})$ causes

random spin precessions upon momentum scattering even at $\alpha = \pm\beta$.

3.6.8 Diffusive Spin-Orbit Time and Length

Here we calculate several relevant time and length scales in our systems by using a simple 2D diffusive model.

Random walk in two dimensions: diffusive motion. We determine the theoretical spin relaxation time τ_{eff} via the D'Yakonov-Perel' (DP) spin dephasing mechanism: as an electron performs a two-dimensional random walk in real space due to momentum scattering, it precesses about the momentum-dependent spin-orbit field $\mathbf{B}_{\text{RD}}(\mathbf{k})$, whose direction is randomly changing as well, thus accruing random precessional phases and spin dephasing after many scattering events in a time τ_{DP}.

Let $r_{x_i} = \sum_{j=1}^{N} \delta_{x_i}^j$ be the x_i component of the electron position vector on the (x_-, x_+) plane after a total of N scattering events whose jth displacement along the corresponding direction we denote by $\delta_{x_i}^j$. As usual in random walks [137], $\langle r_{x_i}\rangle_t = 0 = \langle \delta_{x_i}^j\rangle_t$ and its variance $\sigma_{x_i}^2 = \langle r_{x_i}^2\rangle_t = N\langle(\delta_{x_i}^j)^2\rangle_t$. Here $\langle ...\rangle_t$ denotes a time average over the survival probability $P(t) = \exp(-t/\tau_p)$, with τ_p being the momentum scattering time. Here, $P(t)$ is the probability of surviving a time t without suffering a collision (momentum scattering). The individual mean square displacement $\langle(\delta_{x_i}^j)^2\rangle_t = \langle(v_{x_i}t)^2\rangle_t$ is independent of j and equals to $\langle(\delta_{x_i}^j)^2\rangle_t = v_F^2\tau_p^2$, where we have used $\langle v_{x_i}^2\rangle_t = v_F^2/2$ and $\langle t^2\rangle_t = 2\tau_p^2$. Since $N = \tau_{\text{DP}}/\tau_p$, we find $\sigma_{x_i}^2 = (\tau_{\text{DP}}/\tau_p)v_F^2\tau_p^2 = \tau_{\text{DP}}l^2/\tau_p = 2D\tau_{\text{DP}}$, where $l = v_F\tau_p$ is the electron mean free path and $D = l^2/2\tau_p$. We now define the spin diffusion lengths along x_+ and x_- via $\lambda_{\text{DP,x}_+}^2 = \sigma_{x_+}^2 = 2D\tau_{\text{DP}}$ and $\lambda_{\text{DP,x}_-}^2 = \sigma_{x_-}^2 = 2D\tau_{\text{DP}}$, respectively. Since $\lambda_{\text{DP,x}_+} = \lambda_{\text{DP,x}_-} = \lambda_{\text{DP}}$, the direction of the diffusion is isotropic and the product $\lambda_{\text{DP,x}_+}\lambda_{\text{DP,x}_-} = \lambda_{\text{DP}}^2 = 2D\tau_{\text{DP}}$ gives the characteristic loop area A of a closed trajectory. Thus we obtain $\lambda_{\text{DP}} = \sqrt{2D\tau_{\text{DP}}}$ for the conversion between spin relaxation time and spin diffusion length. As already shown in the main text and methods, using an Aharonov-Bohm phase of $\Delta\varphi = 1$ from the flux through A, we can convert the experimental B_{SO} to a

SO length $\lambda_{\mathrm{SO}} = \sqrt{\hbar/2eB_{\mathrm{SO}}}$, which we can further convert to a SO time $\tau_{\mathrm{SO}} = \lambda_{\mathrm{SO}}^2/(2D)$.

For a degenerate 2DEG, the individual DP spin relaxation rates are spin-direction dependent, with $\tau_{\mathrm{DP},\mathrm{s_{x_i}}}$ $(i = +, -, z)$ for spins polarized along $\hat{x}_+$, $\hat{x}_-$, and $\hat{z}$, being described by [60]

$$\frac{1}{\tau_{\mathrm{DP},\mathrm{s_{x_\pm}}}} = \frac{2\tau_1 k_F^2}{\hbar^2}\left[(\alpha \pm \beta)^2 + \frac{\tau_3}{\tau_1}\beta_3^2\right], \tag{3.24}$$

$$\frac{1}{\tau_{\mathrm{DP},\mathrm{s_z}}} = \frac{4\tau_1 k_F^2}{\hbar^2}\left[\alpha^2 + \beta^2 + \frac{\tau_3}{\tau_1}\beta_3^2\right]. \tag{3.25}$$

Here, τ_1 is the transport scattering time τ_p and we assume $\tau_1 \geq \tau_3$, where τ_3 is the third moment of the momentum relaxation time [60]. For dominant small angle scattering, one obtains $\tau_1 = 9\tau_3$.

Effective spin-dephasing time and effective spin-diffusion length Note that Eqs. 3.24 and 3.25 describe the relaxation of polarized spins, e.g. optically excited spins. In contrast, there is a negligible spin polarization in our transport experiment, therefore we define an effective τ_{eff} for a random spin, by taking the average of the spin lifetimes

$$\tau_{\mathrm{eff}} = \frac{1}{3}\left(\tau_{\mathrm{DP},\mathrm{s_{x_+}}} + \tau_{\mathrm{DP},\mathrm{s_{x_-}}} + \tau_{\mathrm{DP},\mathrm{s_z}}\right). \tag{3.26}$$

Here we average the spin relaxation times rather than the spin relaxation rates. This is because we have three independent, equally populated spin components that are each relaxing through its own, separate channels (diffusion), in contrast to a single spin species that can relax through three different channels. More precisely, we note that the initial electron spin in a loop can point (with equal probabilities) along the s_{x_-}, s_{x_+}, and s_z axes (analogous to x_+, x_-, and z, respectively), which have unequal (and independent) spin-dephasing times $\tau_{\mathrm{DP},\mathrm{s_{x_-}}}$, $\tau_{\mathrm{DP},\mathrm{s_{x_+}}}$, and $\tau_{\mathrm{DP},\mathrm{s_z}}$. Hence we take τ_{eff} to be the average in Eq. 3.26. Note that this also correctly results in a diverging τ_{eff} for $\alpha = \pm\beta$ in case of negligible β_3. With this at hand, we can define an effective diffusive SO length

$\lambda_{\text{eff}} = \sqrt{2D\tau_{\text{eff}}}$ reading

$$\lambda_{\text{eff}} = \frac{\hbar^2}{\sqrt{6}m^*}\sqrt{\left[(\alpha-\beta)^2+\frac{\tau_3}{\tau_1}\beta_3^2\right]^{-1}+\left[(\alpha+\beta)^2+\frac{\tau_3}{\tau_1}\beta_3^2\right]^{-1}+\frac{1}{2}\left[\alpha^2+\beta^2+\frac{\tau_3}{\tau_1}\beta_3^2\right]^{-1}} \tag{3.27}$$

Equivalently, this average spin diffusion length can be defined from the variance $\bar{\sigma}^2_{x_i} = (\sigma^2_{x_i,s_{x_-}} + \sigma^2_{x_i,s_{x_+}} + \sigma^2_{x_i,s_z})/3$, along $\hat{x}_i$ $i = +, -$, obtained by averaging over the initial spin directions. At $\alpha = \pm\beta$ and small β_3 (and/or $\tau_3 \ll \tau_1$) the SO length λ_{eff} diverges, as explained in the main text. We fit our data points using Eq. 3.27 and the ratio τ_3/τ_1 as a free parameter, as shown in Fig. 3.15. The resulting ratio $\tau_3/\tau_1 \lesssim 0.2$ (0.4) for $n = 6 \cdot 10^{11}\,\text{cm}^{-2}$ ($9 \cdot 10^{11}\,\text{cm}^{-2}$) can be explained by small angle scattering, originating from the long range potential of the remote donors.

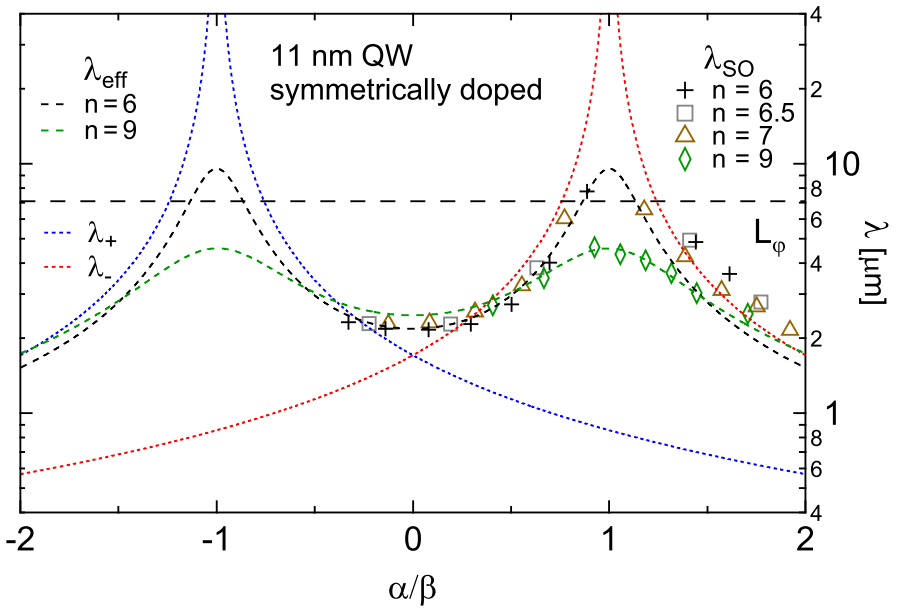

Figure 3.15: Theoretical and experimental SO lengths including symmetry breaking. In contrast to the ballistic $\lambda_\pm$ (dotted red and blue), the diffusive λ_{eff} (dashed black and green, fits to λ_{SO} data points) includes the symmetry breaking higher harmonic term and does not diverge at $\alpha = \pm\beta$. The highest density $n = 9 \cdot 10^{11}\,\text{cm}^{-2}$ (green markers) shows the strongest symmetry breaking effect, where WAL remains visible through $\alpha = \pm\beta$, thus allowing extraction of $\lambda_{\text{SO}} < L_\varphi$ at $\alpha = \beta$.

Equivalence between ballistic and spin-diffusion lengths. We now argue that the ballistic spin precession lengths $\lambda_\pm = \hbar^2/(2m^*|\alpha \pm \beta|)$ introduced in the main text and

the spin diffusion lengths $\lambda^{\mathrm{DP}}_{\mathrm{s_{x_-}}} = \sqrt{\sigma^2_{s_{x_-}}} = \sqrt{2D\tau_{\mathrm{DP,s_{x_-}}}}$ and $\lambda^{\mathrm{DP}}_{\mathrm{s_{x_+}}} = \sqrt{\sigma^2_{s_{x_+}}} = \sqrt{2D\tau_{\mathrm{DP,s_{x_+}}}}$ defined via the DP random-walk process are equivalent. Here we drop the index x_i on the variance, as it does not depend on $\hat{x}_i$ since D is assumed isotropic in our model (Sec. 3.6.8), and add a spin index to it, which we had mostly omitted in the preceding paragraphs for ease of notation. From its definition, $\lambda^{\mathrm{DP}}_{\mathrm{s_{x_-}}}$ describes the spin diffusion length for an electron performing a random walk in two dimensions with its spin pointing initially along s_{x_-}. A similar interpretation holds for $\lambda^{\mathrm{DP}}_{\mathrm{s_{x_+}}}$. The definition of the ballistic $\lambda_\pm$ did not include third harmonic effects. Thus when setting to zero the third harmonic term in Eq. 3.24 and converting the resulting $\tau_{\mathrm{DP,s_{x_\pm}}}$ to lengths using $\lambda^{\mathrm{DP}}_{\mathrm{s_{x_+}}}$ and $\lambda^{\mathrm{DP}}_{\mathrm{s_{x_-}}}$, we obtain straightforwardly $\lambda^{\mathrm{DP}}_{\mathrm{s_{x_+}}} = \hbar^2/(\sqrt{2}m^*|\alpha+\beta|) \simeq \lambda_+$ and $\lambda^{\mathrm{DP}}_{\mathrm{s_{x_-}}} = \hbar^2/(\sqrt{2}m^*|\alpha-\beta|) \simeq \lambda_-$. The diffusion constant D cancels in the conversion from time to length. Hence the diffusive spin relaxation length and the ballistic spin precession length are mathematically equivalent.

The physical reason for this equivalence is as follows. Firstly, recall that the ballistic precession lengths $\lambda_\pm$ define distances over which an electron traveling along $\hat{x}_\pm$ with its spin perpendicular to the effective Rashba-Dresselhaus field [Eq. 3.22] precesses by 1 radian. More specifically, an electron traveling along $\hat{x}_-$ ($\hat{x}_+$) with its spin pointing along either $\hat{x}_-$ ($\hat{x}_+$) or $\hat{z}$ (or any linear combination of these) will undergo spin precession about $\mathbf{B}^{(1)}_{\mathrm{RD}}(k_-,0) = \frac{2}{g\mu_{\mathrm{B}}}(\beta-\alpha)k_-\hat{x}_+$ ($\mathbf{B}^{(1)}_{\mathrm{RD}}(0,k_+) = \frac{2}{g\mu_{\mathrm{B}}}(\beta+\alpha)k_+\hat{x}_-$) covering a distance λ_- (λ_+) as it rotates by 1 radian. Secondly, note that the spin diffusion length $\lambda^{\mathrm{DP}}_{\mathrm{s_{x_-}}}$ ($\lambda^{\mathrm{DP}}_{\mathrm{s_{x_+}}}$) denotes a distance over which an electron moving initially along an *arbitrary* direction on the (x_+,x_-) plane and with its spin pointing along s_{x_-} (s_{x_+}), accrues a net precession of 1 radian about the total Rashba-Dresselhaus field [Eq. 3.22] after many random momentum scattering events. However, because the initial spin polarization is pointing along s_{x_-} (s_{x_+}) we can neglect the Rashba-Dresselhaus field component that is parallel to s_{x_-} (s_{x_+}), i.e., the $\hat{x}_-$ ($\hat{x}_+$) component, when calculating the spin dephasing due to the DP mechanism. This is physically justified as the precession around the parallel field component does not drive the spin direction away from its initial spin polarization, but rather just randomizes its phase around that direction. In the presence of just the x_+

(x_-) component of $\mathbf{B}_{\mathrm{RD}}$, which is perpendicular to the initial s_{x_-} (s_{x_+}), the real-space random-walk problem in two dimensions becomes a 1D problem in spin space with the electron spin performing random ("Abelian") precessions about this unidirectional field component. What we just described, despite 2D charge diffusion, is similar to a ballistic spin precession about a fixed axis, which is precisely what λ_+ (λ_-) is; hence the equivalence between the spin diffusion $\lambda^{\mathrm{DP}}_{\mathrm{s_{x_+}}}$ ($\lambda^{\mathrm{DP}}_{\mathrm{s_{x_-}}}$) and ballistic λ_+ (λ_-) lengths. Note that when the initial spin polarization for the diffusive motion is pointing along s_z then both components of the Rashba-Dresselhaus field are relevant for spin dephasing away from this initial spin direction; a simple calculation using $\lambda^{\mathrm{DP}}_{\mathrm{s_z}} = \sqrt{2D\tau_{\mathrm{DP,s_z}}}$ and Eq. 3.25 yields $\lambda^{\mathrm{DP}}_{\mathrm{s_z}} = \hbar^2/(2m^*\sqrt{\alpha^2+\beta^2})$.

3.6.9 Shubnikov-de Haas Oscillations

In this section we show Shubnikov-de Haas (SdH) oscillations measured during a separate cooldown of the 9.3 nm QW. Measurements were performed in a dilution refrigerator with base temperature 20 mK. We have used a standard four-wire lock-in technique at 633 Hz and 100 nA current bias. In Fig. 3.16 a) and b) the density and moblitiy maps for this cooldown are shown. The lower panels labeled with 1-3 show the SdH oscillations (left column) and their respective Fourier spectra (right column) for a contour of constant density ($n = 4.5 \cdot 10^{11}\,\mathrm{cm}^{-2}$) as indicated in the density and mobility map. In Fig. 3.17 the SdH oscillations and Fourier spectra for the gate configurations 4-6 from Fig. 3.16 a) are shown.

The SdH oscillations are clearly visible for all gate configurations. In the Fourier spectra we see a peak at the fundamental frequency of approximately 10 cycles per Tesla and multiples of it. Panel 1 of Fig. 3.16 also shows the SdH oscillations calculated from theory (to be presented elsewhere) with up to $k = 6$ Fourier components (black). These higher harmonics are clearly seen in the Fourier spectra and are in good agreement with the experimentally observed ones. We also note that these peaks are not accompanied by any additional peaks. The influence of the SO interaction on the magnetoconductance

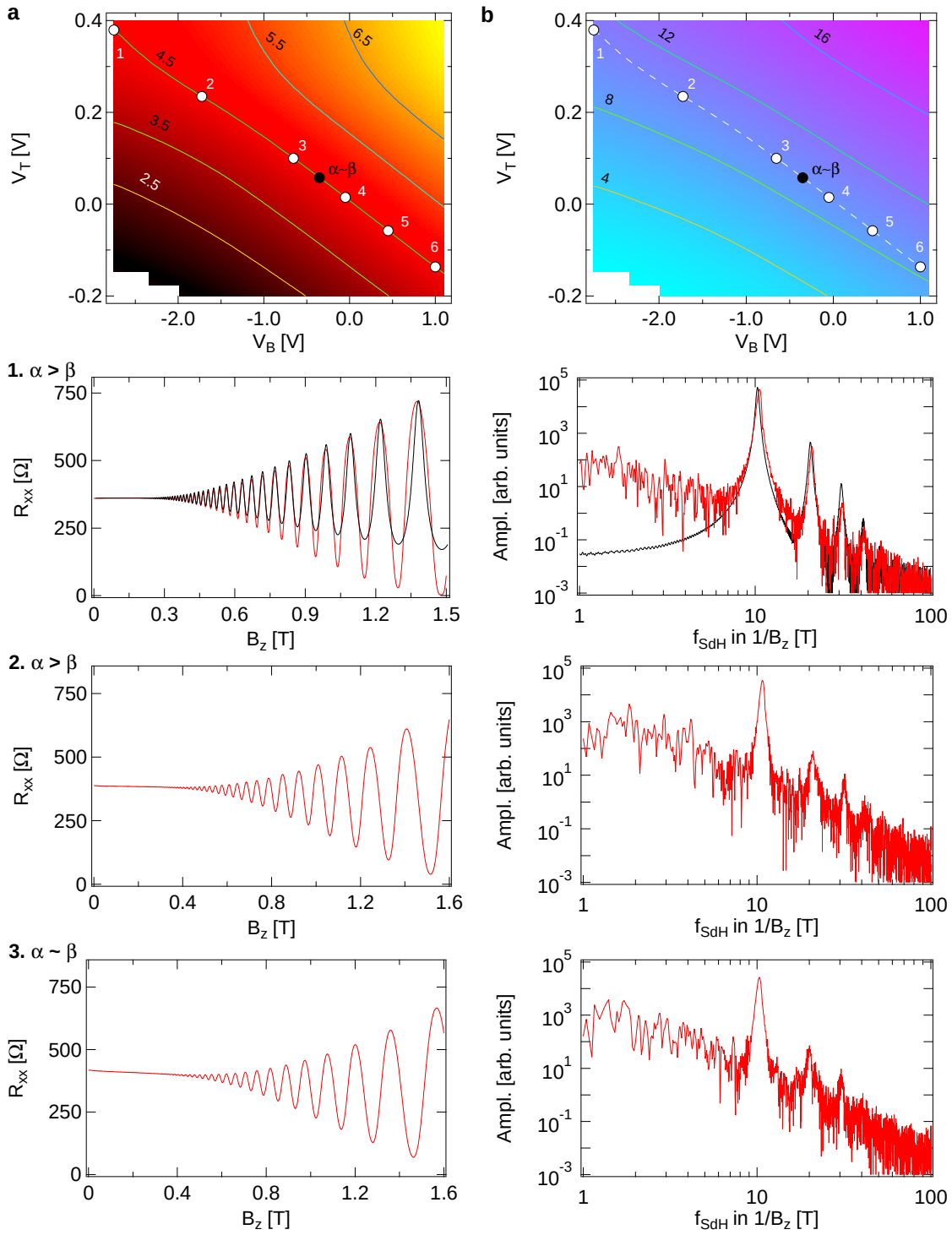

Figure 3.16: Shubnikov de Haas oscillations measured on the 9.3 nm QW - I. Charge carrier density n (**a**) and mobility (**b**) as a function of top gate voltage V_T and back gate voltage V_B. Contour lines are labled in units of 10^{11} cm^{-2} (**a**) and m^2/Vs (**b**), respectively. Gate configurations at which the SdH data was measured are indicated on the density and mobility map as points labled with 1-6. The gate configuration at which $\alpha = \beta$ is also shown. In the panel below the corresponding SdH oscillations at the gate configurations 1-3 are shown (left column) and beside its Fourier spectra (right column). In panel 1 the SdH oscillations plotted from theory and its Fourier spectrum are shown as well (black curves).

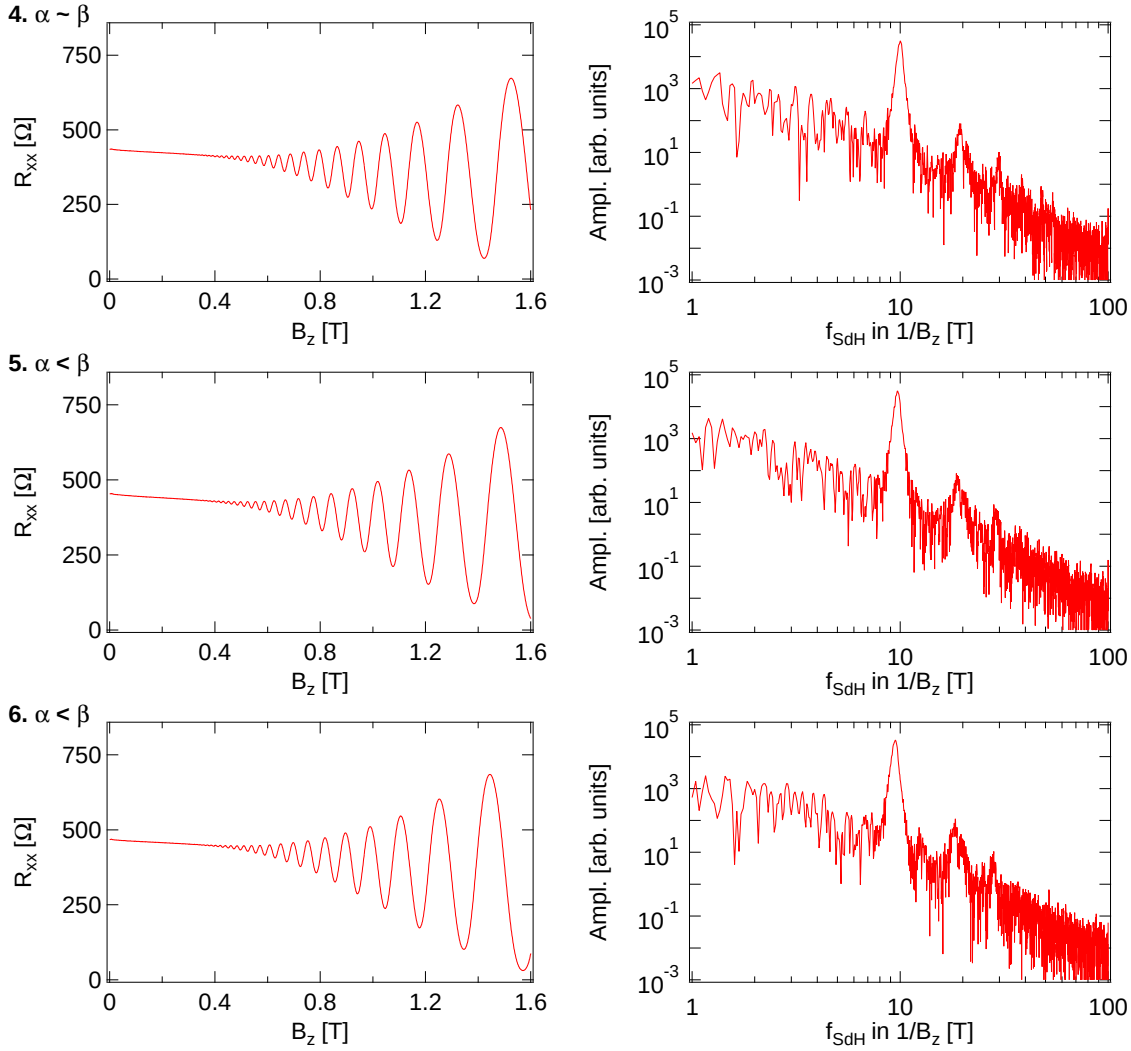

Figure 3.17: Shubnikov-de Haas oscillations measured on the 9.3 nm QW - II. Continued SdH oscillations and their Fourier spectra for the gate configurations 4-6 as indicated in Fig. 3.16 a.

oscillations can cause a spin splitting of the subbands which leads to a beating pattern in the oscillations. Here we do not see any beating nor are there any other frequencies visible. The beating pattern due to SO induced spin splitting has been reported in $In_xGa_{1-x}As$ quantum wells [138]. Generally the SO strength is much larger in In-based semiconductors than in GaAs, thus one would not expect to see here a beating of the SdH oscillations. We try to estimate the beating frequency compared to the SdH frequency for the measured data. The MC oscillations can simply be described by an oscillation of the density of states in $1/B$ [43]. For a beating to occur there must be two frequencies. By comparing the relevant energy scales we can get an estimate about the period with which the beating would occur in the low field regime. For simplicity we assume only a contribution of the Rashba SO interaction. We compare the Fermi energy E_F to the Rashba energy $E_R = \alpha k_F$. We get $E_R = 2\alpha k_F = 0.13\text{meV}$ and $E_F = \frac{\hbar^2 k_F^2}{2m^*} = 14.0\text{meV}$, where we have used $\alpha \approx 8\text{meVÅ}$ and $n = 4.5 \cdot 10^{11}\text{cm}^{-2}$. This means that these beatings would occur at a very large magnetic field, which is beyond the low field limit. Thus it is impossible to observe these oscillations in our data.

4 Symmetry Breaking of the Persistent Spin Helix in Quantum Transport

Pirmin J. Weigele, [1,*], D. C. Marinescu [2,*], Florian Dettwiler, [1] Jiyong Fu, [3] Shawn Mack [4], J. Carlos Egues, [5] David D. Awschalom [6,7] and Dominik M. Zumbühl [1]

[1] *Department of Physics, University of Basel, CH-4056 Basel, Switzerland*

[2] *Department of Physics and Astronomy, Clemson University, Clemson, South Carolina 29634, USA*

[3] *Instituto de Física, Universidade de Brasília, Brasília-DF 70919-970, Brazil*

[4] *U.S. Naval Research Laboratory, Washington, DC 20375, USA*

[5] *Instituto de Física de São Carlos, Universidade de São Paulo, 13560-970 São Carlos, São Paulo, Brazil*

[6] *California NanoSystems Institute, University of California, Santa Barbara, California 93106, USA*

[7] *Institute for Molecular Engineering, University of Chicago, Chicago, Illinois 60637, USA*

[*] These authors contributed equally to this work

This chapter has been submitted to Physical Review X.

4.1 Abstract

We exploit the high-symmetry spin state obtained for equal Rashba and linear Dresselhaus interactions to derive a closed-form expression for the weak localization magnetoconductivity – the paradigmatic signature of spin-orbit coupling in quantum transport. The small parameter of the theory is the deviation from the symmetry state introduced by the mismatch of the linear terms and by the cubic Dresselhaus term. In this regime, we perform quantum transport experiments in GaAs quantum wells. Top and back gates allow independent tuning of the Rashba and Dresselhaus terms in order to explore the broken-symmetry regime where the formula applies. We present a reliable two-step method to extract all parameters from fits to the new expression, obtaining excellent agreement with recent experiments. This provides experimental confirmation of the new theory, and advances spin-orbit coupling towards a powerful resource in emerging quantum technologies.

4.2 Introduction

The spin-orbit (SO) interaction is of profound importance for a broad range of phenomena in modern condensed matter physics, such as spin textures [139, 140], spin Hall effects [18, 141], topological insulators [19, 142–144] and Majorana fermions [20, 21], as well as for application in spintronics [22, 53] and quantum computation [145–147]. Semiconductors such as GaAs, InAs, or GaSb offer various strengths of SO coupling combined with a high level of electrical control [29, 64–66, 92, 116, 122, 148] over the SO parameters e.g. in quantum wells and are thus suitable for a broad range of experiments. The two dominant contributions to SO coupling in semiconductor quantum wells arise from breaking of structural and bulk inversion symmetry, quantified by the Rashba coefficient α and the Dresselhaus coefficient γ, respectively. While the Rashba effect [14] is linear in electron momentum, the bulk Dresselhaus [13] term is cubic. When projected into a quantized 2D system, it retains a cubic component with coefficient β_3 but also acquires a linear

component of strength β.

A particularly interesting situation arises when $\alpha = \beta$: a persistent spin helix (PSH) can be formed [23, 24], which is robust against D'yakonov Perel scattering, strongly suppressing spin relaxation [25]. In this state, spins do not precess at all when traveling ballistically along one particular direction in the 2D plane, while precessing quickly when proceeding along the orthogonal direction in the 2D plane. Effectively, spin symmetry is restored by a complete cancellation of the Rashba and linear Dresselhaus terms along one direction and the creation of a uniaxial internal SO field – broken only by the cubic Dresselhaus term and by a deviation from $\alpha = \beta$.

With optical methods, the SO parameters can be readily extracted from experiments [25, 26, 68–70, 149–152] by monitoring a spin component directly e.g. with Kerr rotation methods. This is much more difficult to achieve from electronic transport measurements where the spin information is not usually directly accessible. In materials with strong SO coupling, the beating patterns of the Shubnikov de-Haas oscillations can sometimes be used to extract the Rashba parameter [64–66, 116, 138]. Even if SO coupling is weak, quantum interference effects depend very sensitively on the spin of the electron, giving weak antilocalization (WAL) as the paradigmatic signature of SO coupling in quantum transport experiments. To extract the SO parameters from such highly-sensitive magnetoconductance measurements, one needs to rely on a model containing the relevant SO terms. For some special cases, it was possible to derive closed-form expressions already early-on: with cubic terms only [9, 79], without SO terms altogether [9, 153], or for the spin helix point $\beta = \pm\alpha$ and $\beta_3 = 0$, in which case weak localization (WL) was recovered [50] as if there were no SO coupling at all. It is clear that these are very isolated special cases of limited practical use.

A closed-form expression for the quantum corrections to the magnetoconductance that incorporates all the SO coupling terms identified above is highly desirable not just for its fundamental theoretical value, but particularly also for applications, where it is important to be able to extract the SO parameters from transport data in order to control and engi-

neer devices. This is required to turn SO coupling into a powerful resource for quantum technologies. Moreover, a closed-form theory is clearly preferable over a numerical expression which can be difficult or unpractical to handle for data fitting. However, despite almost 4 decades of considerable efforts, it was not possible to provide such a closed-form expression containing cubic and both linear terms.

The spin helix state – predicted [23, 24] and realized [25, 29, 121] only relatively recently – affords a new opportunity in tackling this long-standing and unresolved problem by offering a high symmetry point around which a new small parameter may be introduced: the deviation from the perfect spin symmetry, via imperfectly matched linear terms $\propto \alpha - \beta$ or through the cubic term $\propto \beta_3$. In both cases of broken spin symmetry, the effective SO field remains small, i.e. the WAL minima occur at small magnetic field, thus remaining in the spin diffusive regime.

Here, we exploit this new small parameter and are able to derive a new closed-form expression including cubic and both linear SO terms in the vicinity of the PSH point by following the established WAL formalism. Further, we develop a reliable method to extract all relevant SO parameters from quantum transport data using the new expression. This method exploits the cancellation of the linear terms to first extract independently the cubic term and phase coherence in the high carrier density regime where the cubic term already breaks spin symmetry and restores WAL. Then, we tune slightly away from $\alpha = \beta$ and can now also extract the linear SO parameters, again from fits to the new theory. This two stage procedure delivers all SO parameters, in very good agreement with recent transport studies [63, 148] as well as optical experiments [26, 40, 154]. In particular, we extract a Dresselhaus material parameter $\gamma = 11.5 \pm 1\,\mathrm{eV\AA}^3$ in good agreement with recent experiments.

4.3 Theory of Quantum Corrections to Conductivity

There is a large body of literature addressing the subject of quantum corrections over the past decades: already the very early work of Hikami, Larkin and Nagaoka [9] includes SO

effects in the form of impurity scattering (skew scattering) in the diffusive regime and is the only work to date to provide a closed-form expression in presence of SO interaction and a magnetic field. The effect of an in-plane magnetic field was also discussed soon after [81]. For the case of III-V semiconductors where the Dyakonov-Perel mechanism [56] is prevalent in the diffusive regime, the linear and cubic Dresselhaus terms were included in presence of a magnetic field [80], providing an analytical but not closed-form expression. A similar expression is obtained when only the Rashba term is retained [86]. For the generic case with both Rashba and linear as well as cubic Dresselhaus terms, a closed-form or analytical expression is not available and a numerical solution has to be obtained [50, 93].

Beyond the diffusive regime, only skew scattering was considered [95, 99] and had to be solved numerically. Both Rashba and Dresselhaus terms could be treated but only numerically and without taking into account coherent interference effects between the terms [101]. More complete numerical models exist for either only Rashba or only linear Dresselhaus terms [103] or also for all three terms [104, 106, 136].

Here, we consider a 2D electron gas placed in the $\hat{x} - \hat{z}$ plane and the $\hat{y}$-axis perpendicular to the plane. The single particle Hamiltonian corresponding to an electron of effective mass m^*, momentum $\mathbf{p} = \{p_x, p_y, p_z\}$ and spin $\sigma = \{\sigma_x, \sigma_y, \sigma_z\}$ with Rasbha and Dresselhaus SO coupling reads

$$\begin{aligned} H_{\mathbf{p}} = &\frac{p_x^2 + p_z^2}{2m^*} + \alpha(\sigma_z p_x - \sigma_x p_z) + \beta_1(\sigma_z p_z - \sigma_x p_x) \\ &- \gamma(\sigma_z p_z p_x^2 - \sigma_x p_x p_z^2) \,, \end{aligned} \tag{4.1}$$

where β_1 is the bare linear Dresselhaus coefficient. This choice of coordinates highlights the existence of a $\hat{z}$ in-plane axis, obtained through a $\pi/4$ in-plane rotation to be parallel to $[1\bar{1}0]$ ($\hat{x} \parallel [110]$), that becomes the quantization axis for the electron spin. At $\alpha = \beta$ the spin projection on this axis is a good quantum number of the system, a property not immediately apparent if one chooses the standard designation of $\hat{z}$ perpendicular on the plane.

Since the conduction in the degenerate Fermi system is realized only by states at the Fermi surface of wave vector k_F, p_x and p_z are expressed as a function of the polar angle $\varphi_{\mathbf{p}}$ between the momentum $\mathbf{p}$ and the [110] axis. In this case the Dresselhaus Hamiltonian obtains two distinct angular symmetries, effectively renormalizing the linear Dresselhaus strength to β [50, 80, 148]. We can now write the single particle Hamiltonian in terms of symmetric (+) and antisymmetric (-) combinations of the linear SO couplings, as

$$H_{\mathbf{p}} = \frac{\mathbf{p}^2}{2m^*} + \hbar(\mathbf{\Omega}_{\mathbf{p}} \times \sigma) \cdot \hat{y}. \tag{4.2}$$

The SO coupling is expressed via $\mathbf{\Omega}_{\mathbf{p}}$, which is defined as

$$\hbar\Omega^x_{\mathbf{p}} = k_F \left[(\alpha + \beta)\cos\varphi_{\mathbf{p}} - \beta_3 \cos 3\varphi_{\mathbf{p}}\right] , \tag{4.3}$$

$$\hbar\Omega^z_{\mathbf{p}} = k_F \left[(\alpha - \beta)\sin\varphi_{\mathbf{p}} - \beta_3 \sin 3\varphi_{\mathbf{p}}\right] , \tag{4.4}$$

where $\beta = \beta_1 - \beta_3$ is the renormalized linear Dresselhaus coefficient. We follow the standard formalism to calculate the quantum corrections to the conductivity [50, 73, 80, 153] for the single particle Hamiltonian in Eq. (4.2).

The quantum corrections to the conductivity result from the renormalization of the scattering matrix element through the coherent superposition of the incident and scattered states. Although the bare impurity scattering is considered to be spin-independent, in the presence of spin-orbit coupling, an additional spin component is involved in the calculated effective value of the matrix element. This is a result of the slight change in the energy of the electrons when the backscattered momentum is not perfectly anti-parallel, but rather deviates by a small vector $\mathbf{q}$. The ensuing variation in energy $\Delta E(\mathbf{q})$, considered small when compared with the energy uncertainty in the collision process $\hbar/\tau_0$, depends simultaneously on the two spin states of the electrons before and after the collision, which are considered uncorrelated. In a perturbative approach that involves a power expansion in $\Delta E(\mathbf{q})\tau_0/\hbar$, the renormalization is done through the eigenvalues of an operator, called the Cooperon, acting in the 4-dimensional space associated with the two spin 1/2

particles. The eigenvalues of this operator then yield the corrections to the conductivity when summed over all the changes $\mathbf{q}$ and spin channels. Here, in the vicinity of the spin helix symmetry, these eigenvalues can be calculated exactly and we obtain a closed-form expression for the quantum corrections.

The possible total-spin states formed correspond either to total angular momentum $J = 0$, the singlet S, or to the total angular momentum $J = 1$, the triplet states T_0 and $T_\pm$, labeled after the values of $J_z = 0, \pm 1$. The associated four eigenvalues make up the quantum corrections in a system with SO coupling. The singlet is antisymmetric under the exchange of the incident and scattered spins, leading to an additional minus sign, thereby making the singlet contribution positive and, thus, responsible for the antilocalization contribution to the conductivity. The triplet states, on the other hand, are all symmetric and contribute negatively to the conductivity upon backscattering, thus making up the localization contribution to the conductivity.

If a magnetic field is applied, the electron energy is quantized in Landau levels (LL) of index n. In this case, the magnetoconductivity corrections are evaluated from a properly normalized sum that incorporates all the spin channels in all LL. The interplay between the Landau level quantization and the action of the SO coupling in determining the WL contribution in the $\alpha = \beta$ regime is illustrated in Fig. 4.1(a). For any given Landau level $|n\rangle$, we plot the energy of the orbit with respect to the singlet state and indicate the values of the Cooperon wave vector k_x along $\hat{x}$, which fixes the center of the orbit.

As we show in the Appendix, when $\alpha \simeq \beta$, the coupling between the triplet modes decreases so much that it can be considered independent in a first order approximation. This is a consequence of the electron spins becoming polarized along the $\hat{z}$ direction under the action of an effective magnetic field $\sim (\alpha + \beta)$, an orientation that is left unchanged by the scattering process. In the vicinity of this high spin-symmetry point, the orbits of the triplet states are all separated in momentum space with T_+ located at $k_x - Q_+$, T_0 at k_x and T_- located at $k_x + Q_+$, where $Q_+ = \frac{2m^*}{\hbar^2}(\alpha + \beta)$. The energy of the orbits with the $T_\pm$ states is proportional to $((\alpha - \beta)^2 + 3\beta_3^2)/2$, while that of the state T_0 is proportional

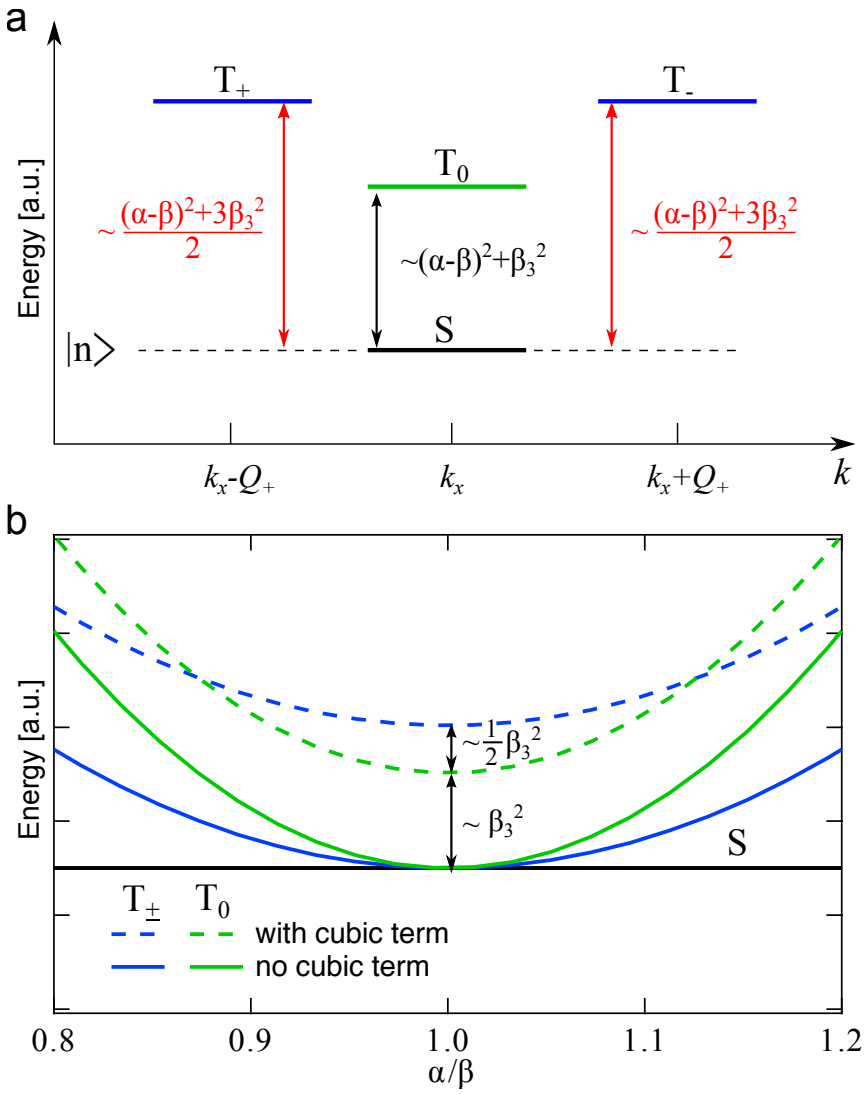

Figure 4.1: Cooperon terms around the PSH symmetry $\alpha = \beta$, with singlet (S) and triplet (T_0, $T_\pm$) states in a generic Landau level $|n\rangle$. (a) Energy of the Cooperon eigenstates as functions of k_x, the Cooperon momentum along $\hat{x}$ which fixes the center of the orbit. The S and T_0 states are located at k_x and become degenerate at $\alpha = \beta$ and $\beta_3 = 0$. T_+ and T_- are degenerate, but since the orbits are separated by $2Q_+$ there is no coupling between them, giving WL. (b) Energies of the eigenstates in one Landau level as a function of the ratio of α/β. The full curves correspond to the case where the cubic term is zero and all states are degenerate at $\alpha = \beta$ and WL is observed. The dashed lines correspond to the states, when the cubic term is strong, then S and T_0 state are not degenerate at $\alpha = \beta$ giving WAL even at $\alpha = \beta$.

to $(\alpha-\beta)^2+\beta_3^2$, as shown in Fig. 4.1(a). The four associated eigenstates are written in the tensor product space between the LL representation and the total angular momentum representation as $|n\rangle \bigotimes |J, J_z\rangle$. The corresponding Cooperon wave vector k_x is introduced in the position representation of $|n\rangle$.

Although the energies of the parallel spin modes $T_\pm$ are equal, the misalignment along k_x with the center orbits separated by exactly $2Q_+$ precludes any coupling between these modes. This situation corresponds to the separation in the momentum space of the two Fermi populations of up and down spin electrons by Q_+, that become spin polarized by an effective magnetic field proportional to $(\alpha+\beta)$ [24]. (The Cooperon is composed of two electrons, so the single particle states are separated in the momentum space by Q_+.) The remaining modes with $J_z=0$, whose orbits are located at k_x, generate opposite sign contributions to WL. Exactly at $\alpha=\beta$ and $\beta_3=0$ they cancel, leading to the disappearance of the WAL. In Fig. 4.1(b) we illustrate how the states in the same Landau level evolve as a function of α/β for zero cubic term (full curves) and finite cubic term (dashed curves), which highlights the role played by the cubic Dresselhaus term, lifting the degeneracy at $\alpha=\beta$ such that the T_0 and S state no longer fully cancel, giving WAL even at $\alpha=\beta$.

In the Appendix we outline the major steps for the calculation (with further details in the SM) while here we give only the result of the closed-form expression for the conductivity correction $\Delta\sigma(B_\perp)$ in a magnetic field $B_\perp$, expressed in terms of the digamma function Ψ,

$$\begin{aligned}\Delta\sigma(B_\perp) = -\frac{e^2}{4\pi^2\hbar}\Bigg[&\Psi\left(\frac{1}{2}+\frac{B_\varphi}{B_\perp}\right)+2\ln\frac{B_{\rm tr}}{B_\perp}\\ &-2\Psi\left(\frac{1}{2}+\frac{B_\varphi}{B_\perp}+\frac{B_{SO-}+3B_{SO3}}{2B_\perp}\right)\\ &-\Psi\left(\frac{1}{2}+\frac{B_\varphi}{B_\perp}+\frac{B_{SO-}+B_{SO3}}{B_\perp}\right)\Bigg].\end{aligned} \tag{4.5}$$

The coherence time τ_φ and transport time $\tau_{\rm tr}$ define two characteristic fields, the dephasing

field B_φ and the transport field B_{tr}, which are given by

$$B_\varphi = \frac{\hbar}{4eD\tau_\varphi}, \tag{4.6a}$$

$$B_{\mathrm{tr}} = \frac{\hbar}{4eD\tau_{\mathrm{tr}}}, \tag{4.6b}$$

with D the diffusion constant in 2D.

The form of Eq. (4.5) is very similar to the one from Hikami, Larkin and Nagaoka [9], but now the arguments in the digamma functions contain the linear Rashba and Dresselhaus terms as well as the cubic Dresselhaus term, via the effective magnetic fields $B_{\mathrm{SO}-}$ and B_{SO3}. These are defined as

$$B_{\mathrm{SO}\pm} = \frac{\hbar}{4e}\left(\frac{2m^*}{\hbar^2}(\alpha \pm \beta)\right)^2, \tag{4.7a}$$

$$B_{\mathrm{SO3}} = \frac{\hbar}{4e}\left(\frac{2m^*}{\hbar^2}\beta_3\sqrt{\frac{\tau_3}{\tau_1}}\right)^2, \tag{4.7b}$$

where $\hbar$ the reduced Planck constant and e the elementary charge. The contribution of the cubic Dresselhaus term β_3 is represented in Equation (4.7b), multiplied by the square root of the ratio of the backscattering time τ_1 and its third harmonic τ_3 which arises due to the higher angular harmonics of the Dresselhaus term in the SO Hamiltonian [50, 80] (see Eq. (S4) in SM). In modulation doped structures, the doping layer is set back from the 2D electron gas. Compared to doping incorporated inside the quantum well, this creates a softer, longer range scattering potential for the electrons with more prevalent small angle scattering [155, 156]. For the ratio of scattering times, the range of possible values is $1/9 \leq \tau_3/\tau_1 \leq 1$, where 1/9 corresponds to dominant small angle scattering [93] and 1 indicates short range scattering (isotropic). Equation (4.5) is valid in the diffusive regime, where $B_{\mathrm{tr}} \ll B_\perp$ and naturally requires weak SO coupling. This is assuming that the spins are precessing only by a small angle in a time τ_{tr}, corresponding to the condition $B_{\mathrm{SO}\pm} \ll B_{\mathrm{tr}}$.

In Fig. 4.2 we plot the magnetoconductance according to Eq. (4.5) with and without the

cubic Dresselhaus term. As we vary the Rashba strength α while keeping the renormalized Dresselhaus term β constant, the conductivity traces transition from WAL (red traces) to WL (black trace), where $\alpha = \beta$. We note that the absence of WAL alone (red dashed and black traces, left panel) does not uniquely identify the PSH symmetry point. Rather, the most pronounced WL curve (black trace) with the deepest and sharpest dip indicates realization of the PSH point. Some small amount of SO coupling (cubic and/or linear terms) away from the symmetry point quenches WL, reducing the depth and sharpness of the WL dip without the appearance of WAL, i.e. a maximum of conductivity at zero field. A lower coherence time has a similar effect, also reducing the depth of the WL dip, and can be difficult to separate from the effects of weak SO coupling [157–159]. If a sufficiently strong cubic term is present, WL is suppressed and WAL appears even at $\alpha = \beta$ (black trace), where the position of the WAL minima (indicated by the dashed blue curve) are closest to $B_\perp = 0$.

4.4 Experiment

4.4.1 Control of Spin Orbit Parameters

We will now discuss the different constituents of Eq. (4.7a) and Eq. (4.7b) and how they relate to experimental adjustable parameters. Electric fields, doping and the interface of the heterojunction result in a confining potential, which causes structure inversion asymmetry and is the origin of the Rashba effect [14]. Its strength α can be tuned as a function of the electric field [64, 65] and is parameterized in our QW as follows

$$\alpha = \alpha_0 + \alpha_1 \delta E_z, \tag{4.8}$$

where α_0 is a sample specific offset and α_1 accounts for the effect of the induced electric field detuning δE_z coming from the voltages applied to the top and back gates (see Eq. (4.29) in the Appendix). The Dresselhaus SO interaction [13] is characterized by the

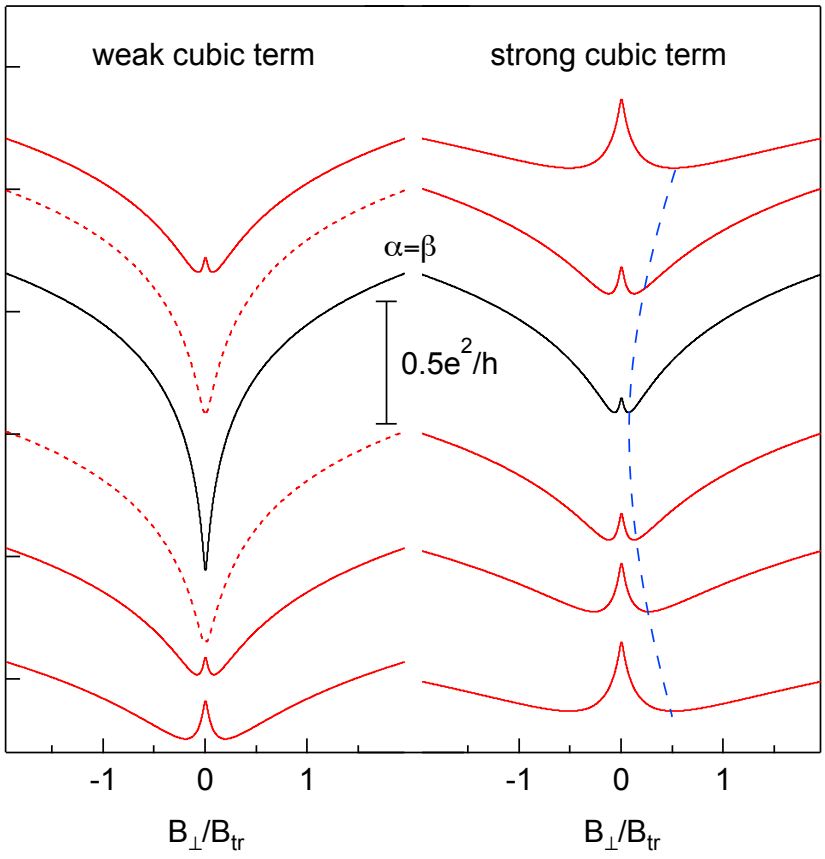

Figure 4.2: Magnetoconductance curves in the regime close to the spin helix symmetry as given by Eq. (4.5). The black traces correspond to $\alpha = \beta$. Left panel: Spin orbit coupling causes a quench of the WL before WAL appears (dashed red traces). Right panel: For a strong cubic term, WAL appears even at $\alpha = \beta$ and is defined by the WAL trace with the WAL minima closest to $B_\perp = 0$

renormalized linear Dresselhaus strength β, which reads

$$\beta = \beta_1 - \beta_3 = \gamma \left(\langle k_z^2 \rangle - \frac{k_F^2}{4} \right), \tag{4.9}$$

where $\beta_1 = \gamma \langle k_z^2 \rangle$ and $\beta_3 = \frac{1}{4}\gamma k_F^2$ is the cubic Dresselhaus term, with γ being the bulk Dresselhaus material coefficient. As the Fermi momentum $k_F^2 = 2\pi n$ depends on the density n, the renormalized Dresselhaus strength becomes controllable via gate voltages, which has recently been demonstrated [148]. Over the range of the applied gate voltages $\langle k_z^2 \rangle$ is effectively constant.

4.4.2 Evaluation Procedure

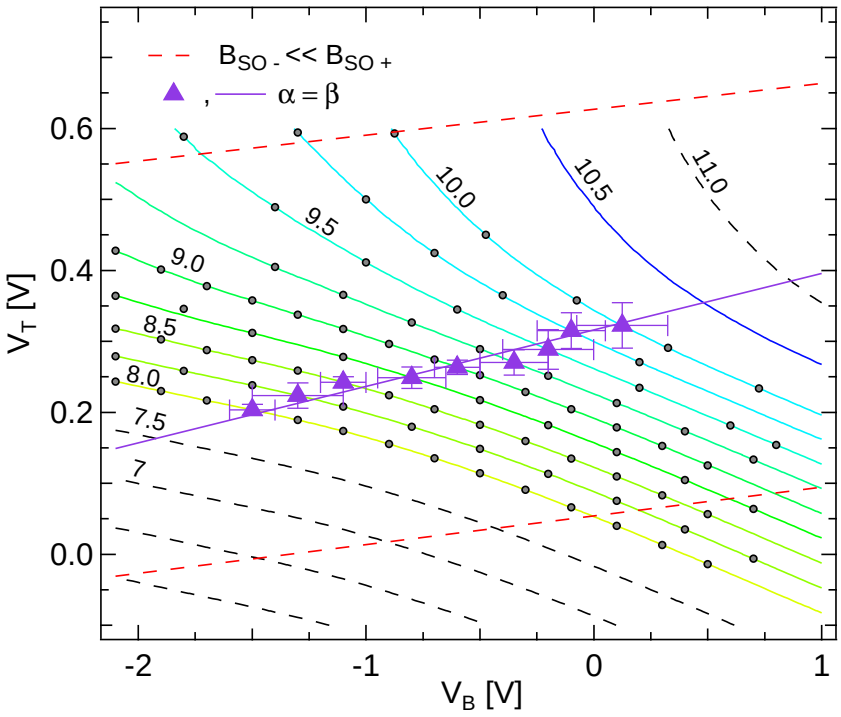

Figure 4.3: Density map with symmetry points (purple triangles) as a function of top V_T and back gate V_B voltage for data set #2 (see supplementary for details). Along contours of constant density (labeled in units of $10^{15}\mathrm{m}^{-2}$), B_{SO-} is changing as a function of detuning δE_z, while B_{SO3} is constant. The gray circles indicate the measured gate configurations. The triangles correspond to the approximate position where $\alpha = \beta$ and the purple line corresponds to a plot of the calculated PSH condition from the extracted SO parameters. Eq. (4.5) is valid everywhere between the red dashed lines.

In the experiment, we first extract the cubic term and phase coherence where the linear

terms cancel but the cubic term already breaks spin symmetry. Then, we detune the linear terms away from equal size and can extract their strength as well, again from fits to the new theory. We control the strength of the SO parameters α and β with the top gate voltage V_T and the back gate voltage V_B. As described in the previous paragraphs, these parameters depend on density n and the detuning δE_z. To obtain a more useful parameter space, we measure the density as a function of V_T and V_B and obtain a density map, shown in Fig. 4.3, with contours of constant density, along which the detuning δE_z changes. We note that for sufficiently negative back gate and positive top gate voltages, the contours of constant density become non-linear, which limits the usable range of δE_z and n. The range of the density is further limited by the requirement that the cubic Dresselhaus term β_3, which depends on density, be large enough, such that B_{SO3} causes WAL even at the PSH symmetry.

The PSH symmetry points are indicated by the purple markers in Fig. 4.3 and their position is estimated from the conductivity traces with the least pronounced WAL feature. This can be done, since along contours of constant density only $B_{\mathrm{SO-}}$ changes as a function of δE_z and B_{SO3} remains constant, as scattering potentials do not change τ_3/τ_1 significantly for constant density. The gate configurations where conductivity traces were measured are indicated by the gray circles in Fig. 4.3. At the gate configurations around the symmetry point, $B_{\mathrm{SO-}}$ is very small and is set to zero when fitting Eq. (4.5) to the data, where only B_φ and B_{SO3} are the fit parameters (see Appendix Sec. 4.6.4 and Supplemental Material Sec. 4.7.4). The transport field B_{tr} is known from independent Hall measurements of density n and mobility μ. Since the symmetry point is not precisely known, we determine B_{SO3} very similarly at the surrounding gate configurations and take the average value, thus obtaining a more robust value for B_{SO3}.

In Fig. 4.4(a) we show typical fits (red) to the measured (black) conductivity traces around the symmetry point. The agreement between fit and theory is very good for $B_\perp \ll B_{\mathrm{tr}}$, where B_{tr} is indicated by the dashed gray curve. The extracted fit parameters B_{SO3} (red triangles) and B_φ (blue triangles) are shown as a function of density in the upper panel of

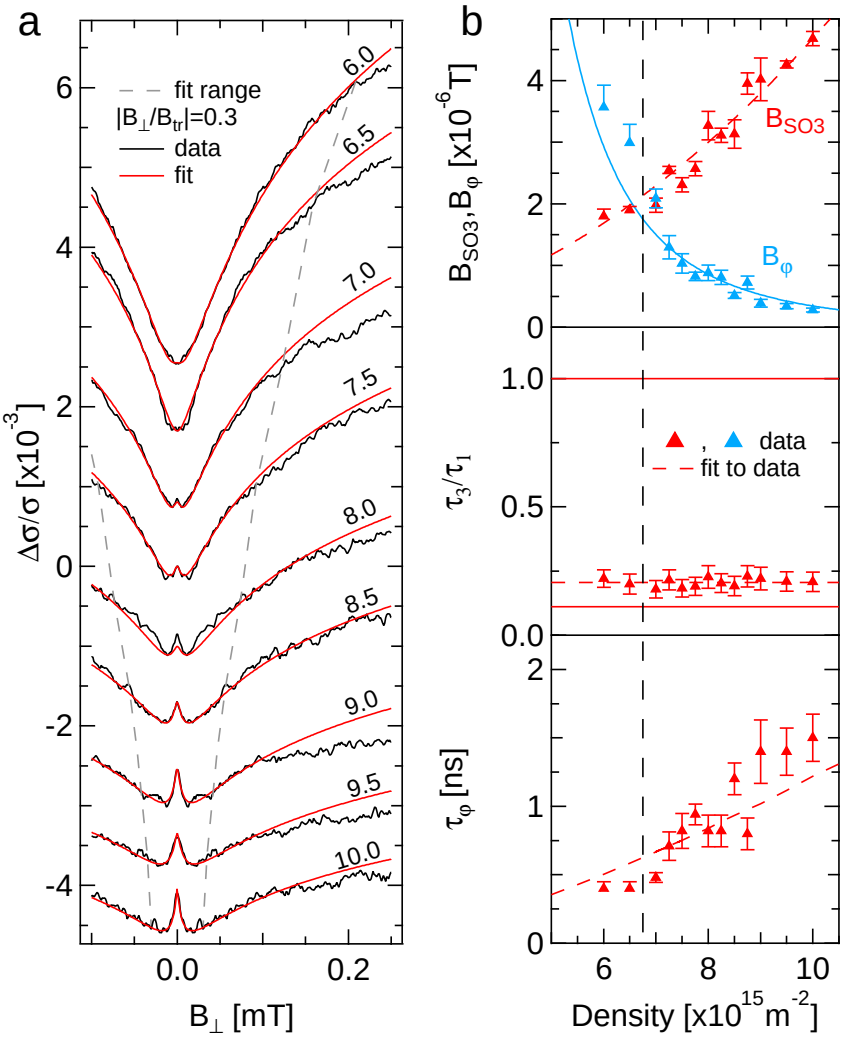

Figure 4.4: (a) Measured conductivity traces (black) around the symmetry point and fits (red) using Eq. (4.5) with the respective density labeled at each trace in units of $10^{15}\mathrm{m}^{-2}$. The measured traces have been symmetrized in $B_\perp$ for fitting. The gray dashed curves correspond to the fit range obeying $B_\perp \ll B_{\mathrm{tr}}$. (b) *Upper panel*: extracted B_{SO3} values versus density. The red dashed curve is a quadratic fit to B_{SO3}. The blue markers and curve correspond to the extracted and calculated B_φ (see main text). *Middle panel*: extracted τ_3/τ_1 using the later to be determined γ for each individual value of B_{SO3} from the upper panel. The red dashed line is the average of τ_3/τ_1. *Lower panel*: coherence time from the extracted B_φ for the respective density and mobility. The red dashed curve is a fit to the data assuming Nyquist dephasing. For the two lowest densities 6.0 and 6.5 (left of the dashed vertical line), the extracted values of B_{SO3} and B_φ are only bounds, see text.

Fig. 4.4(b). A quadratic fit (see Eq. (4.7b)) to the B_{SO3} data finds good agreement, see red dashed line. At low temperatures, Nyquist dephasing dominates [37] and $\tau_\varphi^{-1} \propto T\lambda_F/l_e$, with T being the electron temperature, λ_F the Fermi wavelength and l_e the mean free path. Here, the electron temperature is ∼100 mK estimated independently [160, 161]. Since $B_\varphi \propto \tau_\varphi^{-1}$, we can express B_φ in terms of density and mobility via the above expression for τ_φ. This is shown with the blue curve, reproducing the trend of the extracted B_φ quite well. For $n < 7{\times}10^{15}\mathrm{cm}^{-2}$, indicated by the dashed black line in Fig. 4.4 b), we observe that the conductivity traces in Fig. 4.4 a) no longer show a WAL feature and that $B_{\mathrm{SO3}} \leq B_\varphi$. Thus for densities to the left of the black dashed line, the extraction of a meaningful value for B_{SO3} and B_φ is no longer possible and only an upper bound can be determined.

Using the value of B_φ we can also determine the coherence time τ_φ for each density, which is shown in the lower panel of Fig. 4.4(b). The coherence time is of the order of 1 ns, which is a value expected in GaAs 2D electron gases at mK temperatures [101, 162, 163]. The red dashed curve shows the dependence of τ_φ on density, calculated also for Nyquist dephasing, in qualitative agreement with the data. This allows us to keep τ_φ constant along contours of constant density as the mobility change of ∼10 % is smaller than the error on τ_φ.

We now proceed with the evaluation away from the PSH symmetry by keeping B_{SO3} and τ_φ fixed for each density, thus facilitating the extraction of $B_{\mathrm{SO}-}$ as a function of the detuning δE_z. In Fig. 4.5(a) we show the fits (green) to the conductivity traces along constant density, finding good agreement of the fit with the data. We repeat this for all densities with the respective values of τ_φ and B_{SO3} as previously determined. This delivers a full data set of $B_{\mathrm{SO}-}$ as a function of the density n and the detuning δE_z. Rewriting Eq. (4.7a) with the expressions of α and β (see Eq. (4.8) and Eq. (4.9)) we obtain

$$B_{\mathrm{SO}-} \propto \left(A + \alpha_1 \delta E_z + \frac{1}{2}\pi\gamma n\right)^2, \tag{4.10}$$

with the fit parameters α_1 and γ and $A = \alpha_0 - \gamma\langle k_z^2\rangle$. Thus, the extracted values of $B_{\mathrm{SO}-}$

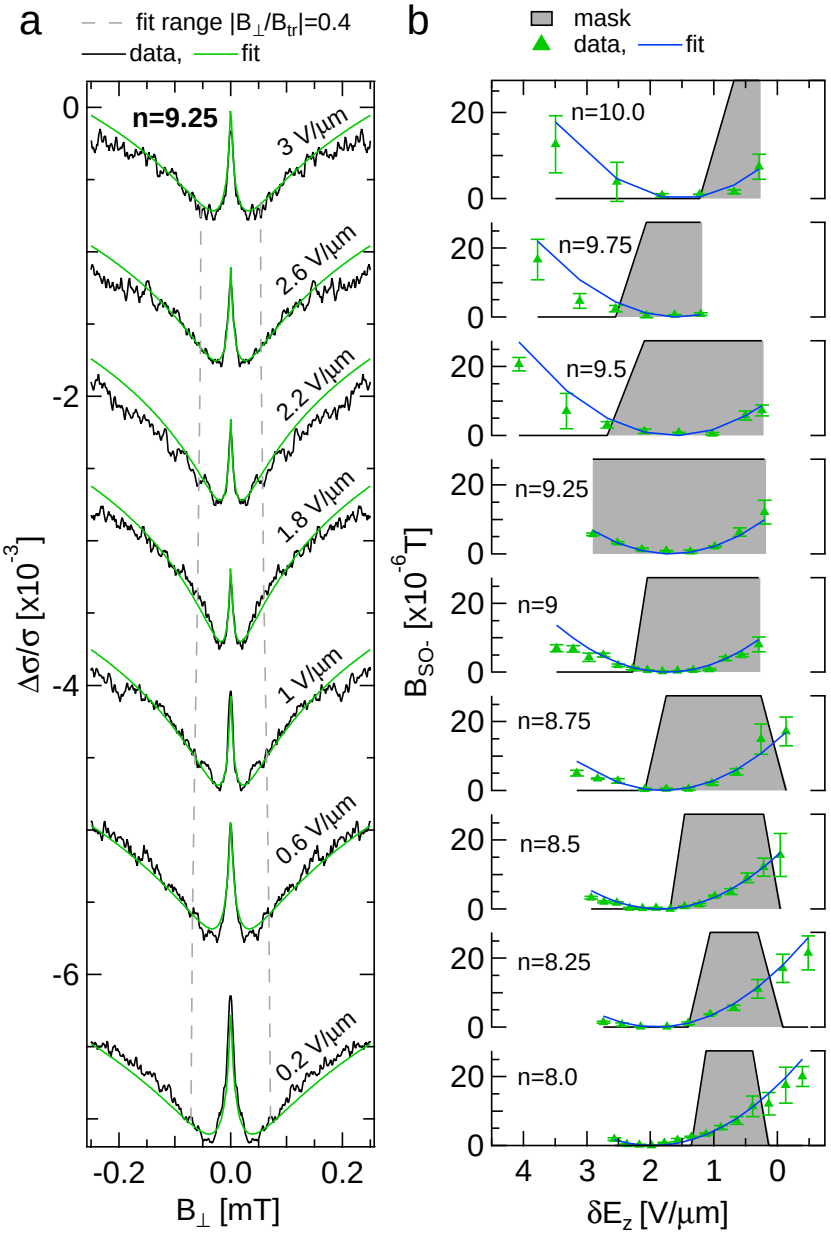

Figure 4.5: Measured traces away from $\alpha \approx \beta$. (a) Fits (green) to the conductivity traces (black) for constant density $n = 9.25 \times 10^{15}\mathrm{m}^{-2}$ in Fig. 4.3. The gray dashed lines indicate the range for the diffusive approximation. Each curve is labeled with its detuning value δE_z. (b) Extracted values of $B_{\mathrm{SO}-}$ versus the detuning δE_z for all densities (arranged vertically and labeled in units of $10^{15}\mathrm{m}^{-2}$ for each $B_{\mathrm{SO}-}$ curve). The error bars correspond to the error on the fit parameter (i.e. one standard deviation). The data in the gray shaded area is included in the fit.

are expected to follow a parabolic shape, which is also seen in Fig. 4.5(b). Some deviations from a parabola are apparent, which are due to the non-linear dependence of the density on gate voltages (see Fig. 4.3). We exclude such data from the fit. The gray shaded area indicates the data points included in the fit – the fit mask – considering the validity of the theory and using only the linear region of gate voltage parameter space, see Fig. 4.3 and Appendix Sec. 4.7.4. The non linear behavior can be seen for larger detunings as the effect of δE_z weakens and the $B_{\mathrm{SO}-}$ parabolas become stretched.

The resulting fit to the data is shown in Fig. 4.5(b) (blue curve), in good agreement with the data within the fit mask and directly yields A, α_1 and γ. Self consistent simulations give a value for $\langle k_z^2 \rangle$ [148], allowing us to determine the Rashba offset parameter α_0 from A.

4.4.3 Determination of the SO Parameters

In Fig. 4.6 we show the results from 5 independent measurements obtained from 2 Hall bar samples on the same quantum well material (see supplementary Sect.4.7.3). Panels (a) through (c) show the fitted values for γ, α_0 and α_1, with their average (red lines) and standard deviation of the mean (red dashed lines). Data sets vary in exact position and especially in number of points measured per density, resulting in varying fit values and associated error bars. To work from the largest possible set of data available we simply include all these independent measurements in the analysis. The complete data sets can be seen on display in the supplementary. The blue lines correspond to the respective values obtained recently from the same wafer material in a previous study [148].

We note that the reported values of γ in quantum transport over the last 30 years ranged from $\sim$ 4-28 eVÅ^3 [101, 164]. The values of $\gamma = 28\,\mathrm{eV\AA}^3$ are close to the literature value, which is obtained from $\mathbf{k} \cdot \mathbf{p}$ calculations. However, electronic bandstructure calculations in $\mathbf{k} \cdot \mathbf{p}$ approximation or with density functional theory tend to give inaccurate SO parameters because these calculations neglect either the many body interactions or contain too many parameters which have to be assumed. In recent years, self consistent numerical

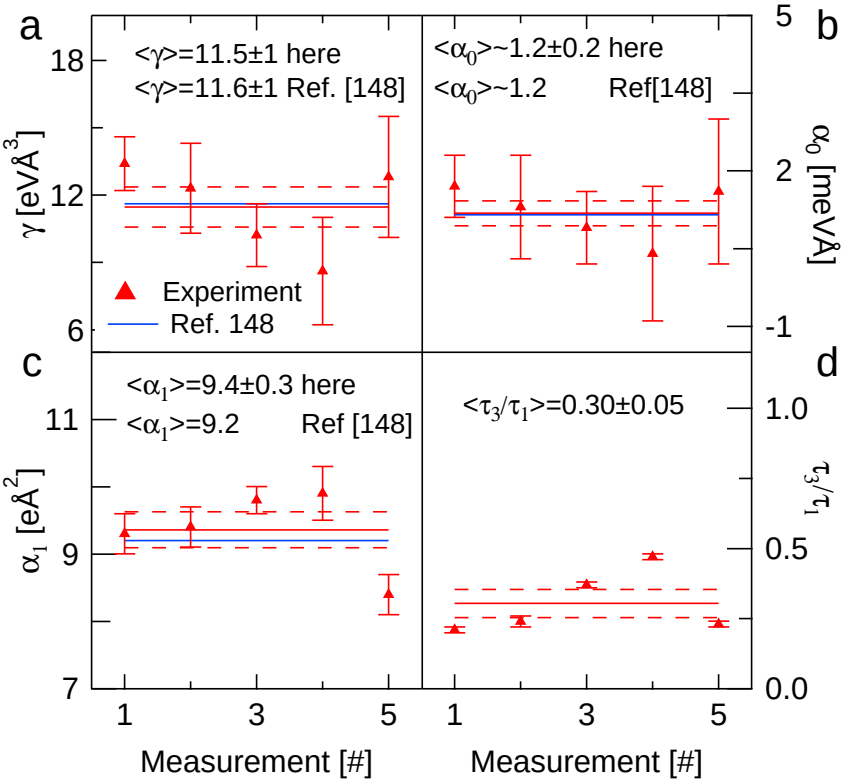

Figure 4.6: SO parameters from 5 measurements obtained on 2 samples. Measurements 1 and 3 correspond to Hall bar no. I and measurements 2,4 and 5 correspond to Hall bar no. II, where measurement 5 is from another cool down, details in supplementary Sect. 4.7.3. The blue lines correspond to the values obtained in a previous work [148], the red lines correspond to their average and the red dashed lines correspond to the standard deviation of the mean. (a) Dresselhaus coefficient γ (b) offset α_0 of the Rashba parameter, (c) α_1 of the Rashba parameter and (d) average scattering time ratio τ_3/τ_1.

calculations including the cubic Dresselhaus term were combined with experiments [63, 148], giving values $\gamma \sim$ 9-11.5 eVÅ^3. These results are confirmed by state of the art single particle GW approximations, calculating the self-energy of a many body system of electrons [165] or density functional theory with density dependent exchange potentials [166]. These results agree very well with our average of $11.5 \pm 1\,\text{eVÅ}^3$ and also recent works using optical spin excitation [26, 121, 154].

The offset parameter α_0 accounts for SO coupling from the electric fields of the charges in the doping layer and the potential of the Hartee term and is a sample specific parameter. It can be calculated via self-consistent methods [67, 148], which is identical with the average of the extracted value. Finally, the Rashba field parameter α_1 has an average value of around $9.4\,\text{eÅ}^2$ which can also be calculated purely from band structure parameters in a quantum well [67] giving $9.2\,\text{eÅ}^2$, very close to previously extracted values [148] and ours.

With the previously determined values of B_{SO3}, we can now extract the value of τ_3/τ_1 using Eq. (4.7b) and the now known value of γ. Assuming τ_3/τ_1 being constant over the range of measured densities, allows us to extract τ_3/τ_1 from the quadratic fit to the B_{SO3} data, shown in the upper panel of Fig. 4.4(b). The fit parameter is proportional to $\gamma\tau_3/\tau_1$ and turns out to be almost the same for all measurements and yields the values shown in Fig. 4.6(d) by supplying the respective value of γ from each measurement. Since $\tau_3/\tau_1 \propto 1/\gamma^2$, smaller values of γ yield a larger τ_3/τ_1, see data points #3 and #4 in Fig. 4.6(d). From the $B_{\text{SO3}}(n)$ data we can also determine τ_3/τ_1 as a function of density n, using the extracted γ, which is shown in the middle panel of Fig. 4.4(b). The values barely change over the range of measured densities and its average value of ~ 0.2 agrees with the one extracted from the fit to B_{SO3}. Overall, the extracted values of τ_3/τ_1 are around 0.3, much smaller than 1, indicating that small angle scattering dominates [93].

4.5 Conclusion

We derived a closed-form expression for the quantum corrections in the vicinity of the PSH symmetry, which includes the Rashba and linear Dresselhaus terms, as well as the

cubic Dresselhaus term. In transport experiments, we studied how breaking of the PSH symmetry, due to the cubic Dresselhaus term and the deviation of the balanced condition of the linear terms, allows to fully quantify the SO strength in a GaAs QW. We achieved this by carefully identifying the different PSH symmetry breaking mechanisms using quantum interference effects.

From the extracted SO terms we directly obtain fundamental SO parameters such as the Dresselhaus coefficient γ and the Rashba parameter α_1, which are in good agreement with recent calculations and experiments. Supplying the variance $\langle k_z^2 \rangle$ from self-consistent simulations allowed to determine the offset α_0 of the Rashba parameter.

The good agreement of the extracted SO parameters with recent theories is an excellent indicator that the new model accurately describes the quantum corrections in the vicinity of the PSH symmetry and can be used as a tool in future studies, whenever Rashba and Dresselhaus SO strengths are comparable. The capability to extract all relevant SO parameters from quantum transport experiments – obtained from fits to a new closed-form theory – opens the door to engineer and control the SO interaction as a useful resource in novel quantum materials such as tailored spin textures, Majorana fermions and parafermions. Further, it can be used to coherently manipulate spins in emerging quantum technologies such as spintronics and quantum computation. This technique is also applicable in other materials where the symmetry-broken PSH regime is accessible.

4.5.1 Acknowledgement

We would like to thank Silas Hoffman, Makoto Kohda, Klaus Richter and Gian Salis for valuable inputs and stimulating discussions, and Michael Steinacher for technical support. This work was supported by the Swiss Nanoscience Institute (SNI), NCCR QSIT, Swiss NSF, ERC starting grant (DMZ), the European Microkelvin Platform (EMP), U.S. NSF DMR-1306300 and NSF MRSEC DMR-1420709 and ONR N00014-15-1-2369, Brazilian grants FAPESP (SPRINT program), CNPq, PRP/USP (Q-NANO), and natural science foundation of China (Grant No. 11004120).

4.5.2 Author Contributions

P. J. W., J. C. E. and D. M. Z. designed the experiment and analyzed the data. All authors discussed the results and commented on the manuscript. S. M. and D. D. A. designed, simulated and carried out the molecular beam epitaxy growth of the heterostructure. P. J. W. carried out the measurements, D. C. M. derived the new expression for the quantum corrections, F. D. fabricated the samples, J. F. and J. C. E. developed and carried out the simulations and theoretical work.

4.6 Appendix: Materials and Methods

4.6.1 Formalism to calculate quantum corrections

Here, we highlight the most relevant results from the formalism to calculate the quantum corrections. The full procedure to calculate the Cooperon and its eigenvalues is shown in detail in the supplementary materials (SM). Our starting point is the general expression connecting the quantum corrections to the conductivity $\Delta\sigma$ and the Cooperon eigenvalues $C_i(\mathbf{q})$,

$$\Delta\sigma = -\frac{2e^2 D\tau_0^2\nu_0}{\hbar^2}\sum_{\mathbf{q},i} C_i(\mathbf{q})\ . \tag{4.11}$$

To determine the relevant singlet and triplet Cooperon modes ($i = 0, 1, 2, 3$), we start with the impurity mediated equation for the Cooperon amplitude $C_{\mathbf{p},\mathbf{p}'}(\mathbf{q})$

$$\begin{aligned} C_{\mathbf{p},\mathbf{p}'}(\mathbf{q}) &= |V_{\mathbf{p},\mathbf{p}'}|^2 \\ &\quad + \sum_{\mathbf{p}''} |V_{\mathbf{p},\mathbf{p}''}|^2 G^+_{-\mathbf{p}''+\hbar\mathbf{q},\epsilon+\hbar\omega} G^-_{\mathbf{p}'',\epsilon} C_{\mathbf{p}'',\mathbf{p}'}\ . \end{aligned} \tag{4.12}$$

The Cooperon amplitude above represents the effective interaction vertex which renormalizes the impurity scattering potential $V_{\mathbf{p},\mathbf{p}'}$. It iteratively includes all higher-order processes (multiple scattering events) involving the scattering off of impurities of two electrons following time-reversed paths described by the retarded and advanced impurity-averaged propagators $G^{\pm}$. We solve Eq. 4.12 via an iterative procedure by expanding the

Cooperon ampliture in its angular harmonics and in the limit $\hbar q \ll p$ (since $\hbar\mathbf{q} = \mathbf{p} + \mathbf{p}'$ and $\mathbf{p}' \approx -\mathbf{p}$). After some lengthy but straightforward calculation (SM) we find for the relevant zeroth-order harmonic of the Cooperon amplitude

$$C^{(0)}_{\mathbf{p},\mathbf{p}'}(\mathbf{q}) = \frac{|V_{\mathbf{p},\mathbf{p}'}|^2}{\tau_0 \mathcal{H}} \ . \tag{4.13}$$

The operator $\mathcal{H}$ in the denominator of the Cooperon is

$$\begin{aligned} \mathcal{H} &= Dq^2 + \frac{1}{\tau_\varphi} + D\left\{\left[Q_+^2 + Q_3^2\right] J_z^2 + \left[Q_-^2 + Q_3^2\right] J_x^2 \right. \\ &+ \left. 2Q_+ q_z J_x - 2Q_- q_x J_z\right\} \ , \end{aligned} \tag{4.14}$$

where $J_{x,z}$ are the total spin angular momentum components and

$$Q_\pm = \frac{2m^*}{\hbar^2}(\alpha \pm \beta) \ , \tag{4.15}$$

$$Q_3 = \frac{2m^*}{\hbar^2}\left(\beta_3\sqrt{\frac{\tau_3}{\tau_1}}\right) . \tag{4.16}$$

We can now diagonalize the Cooperon operator in Eq. (4.13), a matrix in the basis of the total angular momentum of the two spins, and obtain the quantum correction from Eq. (4.11). In what follows, we carry out this procedure for the case in the presence of a quantizing magnetic field $B_\perp$ relevant for the experimental probing of the weak- (and anti-) localization corrections to the conductivity. As described in detail in the SM, in this case we need to switch to a real space description. This is so because in the presence of a magnetic field we approximate the propagators by simply multiplying their zero-field counterpart by a vector potential ($\mathbf{A}$) dependent phase [153]

$$\tilde{G}^\pm(\mathbf{r},\mathbf{r}') = e^{\frac{ie}{\hbar}\int_{\mathbf{r}}^{\mathbf{r}'}\mathbf{A}(\mathbf{l})\cdot d\mathbf{l}} G^\pm(\mathbf{r},\mathbf{r}') \ . \tag{4.17}$$

This standard procedure leads to the change $\mathcal{H} \to \tilde{\mathcal{H}}$ with

$$\tilde{\mathcal{H}}(\mathbf{r},\mathbf{r}') = e^{i\frac{2e}{\hbar}\int_{\mathbf{r}}^{\mathbf{r}'}\mathbf{A}(\mathbf{l})\cdot d\mathbf{l}} \mathcal{H}(\mathbf{r},\mathbf{r}') \ , \tag{4.18}$$

in the denominator of the zeroth-order Cooperon operator; the Fourier transform of $\mathcal{H}(\mathbf{r},\mathbf{r}')$ at zero magnetic field is given by Eq. (4.14).

We solve the generalized eigenvalue problem,

$$\int e^{i\frac{2e}{\hbar}\mathbf{A}\cdot(\mathbf{r}'-\mathbf{r})}\mathcal{H}(\mathbf{r},\mathbf{r}')\psi(\mathbf{r}')d\mathbf{r}' = \mathcal{E}\psi(\mathbf{r}) \ , \tag{4.19}$$

with suitable expansions of the integrand in powers of $\Delta\mathbf{r} = \mathbf{r}' - \mathbf{r} \ll l$ and define the canonical transformation,

$$-i\nabla_z = \sqrt{\tfrac{2eB_\perp}{\hbar}}\tfrac{(a-a^\dagger)}{i\sqrt{2}} \ , \tag{4.20}$$

$$z + z_0 = \tfrac{1}{\sqrt{\frac{2eB_\perp}{\hbar}}}\tfrac{(a+a^\dagger)}{\sqrt{2}} \ , \tag{4.21}$$

with $z_0 = k_x\hbar/2eB_\perp$ (k_x is the Cooperon wave vector along $\hat{x}$). a and $a^\dagger$ are bosonic operators, i.e. $[a,a^\dagger]=1$ that describe the quantization of the Landau levels. We thus obtain the characteristic equation in the number representation,

$$\begin{aligned} & \left\{\frac{1}{\tau_\varphi} + D\left(Q_+^2+Q_3^2\right)J_z^2 + \left(Q_-^2+Q_3^2\right)J_x^2\right. \\ - \ & DQ_+J_z\sqrt{\frac{4eB_\perp}{\hbar}}(a+a^\dagger) - iDQ_-J_x\sqrt{\frac{4eB_\perp}{\hbar}}(a-a^\dagger) \\ + \ & \left. D\left(\frac{4eB_\perp}{\hbar}\right)\left(a^\dagger a+\frac{1}{2}\right)\right\}|u\rangle = \mathcal{E}|u\rangle \ , \end{aligned} \tag{4.22}$$

where $|u\rangle$ is the corresponding eigenket.

In the basis of the total spin angular momentum associated with the 4-dimensional tensor product of the two spin operators of the electrons in time-reversed path, we evaluate the singlet and triplet Landau eigenvalues $\tilde{\mathcal{E}}_{n,i} = \mathcal{E}_{n,i}/(4DeB_\perp/\hbar)$ of the Cooperon ($i=0$ corresponds to the singlet state and $i=1,2,3$ label the triplet state).

The singlet $J=0, J_z=0$ solution of the Cooperon equation is immediately factored, as it is diagonal both in the spin and Landau level spaces. With these, the single Cooperon

mode generates an eingenvalue for the n-th Landau level given by,

$$\tilde{\mathcal{E}}_{n,0} = n + \frac{1}{2} + \frac{B_\varphi}{B_\perp} \,. \tag{4.23}$$

The remaining triplet equation, from Eq. (4.22), is written in the basis of $J = 1, J_z = \{1, 0, -1\}$ in terms of the effective magnetic fields from Eqs. (4.6a)-(4.7b)as

$$\begin{vmatrix} \frac{B_\varphi}{B_\perp} + \frac{B_{\mathrm{SO}+}}{B_\perp} + \frac{B_{\mathrm{SO}-}+3B_{\mathrm{SO}3}}{2B_\perp} & -i\sqrt{\frac{B_{\mathrm{SO}-}}{2B_\perp}}(a-a^\dagger) & \frac{B_{\mathrm{SO}-}+B_{\mathrm{SO}3}}{2B_\perp} \\ +a^\dagger a + \frac{1}{2} - \sqrt{\frac{B_{\mathrm{SO}+}}{B_\perp}}(a+a^\dagger) - \tilde{\mathcal{E}} & & \\ -i\sqrt{\frac{B_{\mathrm{SO}-}}{2B_\perp}}(a-a^\dagger) & \frac{B_\varphi}{B_\perp} + \frac{B_{\mathrm{SO}-}+B_{\mathrm{SO}3}}{B_\perp} + a^\dagger a + \frac{1}{2} - \tilde{\mathcal{E}} & -i\sqrt{\frac{B_{\mathrm{SO}-}}{2B_\perp}}(a-a^\dagger) \\ \frac{B_{\mathrm{SO}-}+B_{\mathrm{SO}3}}{2B_\perp} & -i\sqrt{\frac{B_{\mathrm{SO}-}}{2B_\perp}}(a-a^\dagger) & \frac{B_\varphi}{B_\perp} + \frac{B_{\mathrm{SO}+}}{B_\perp} + \frac{B_{\mathrm{SO}-}+3B_{\mathrm{SO}3}}{2B_\perp} \\ & & +a^\dagger a + \frac{1}{2} + \sqrt{\frac{B_{\mathrm{SO}+}}{B_\perp}}(a+a^\dagger) - \tilde{\mathcal{E}} \end{vmatrix} = 0 \,. \tag{4.24}$$

In the limit of $\alpha \approx \beta$, $B_{\mathrm{SO}-} \ll B_{\mathrm{SO}+}$, as well as $B_{\mathrm{SO}3} \ll B_{\mathrm{SO}+}$, leading to a justified cancellation of all off-diagonal terms proportional with $B_{\mathrm{SO}-}$ or $B_{\mathrm{SO}-} + B_{\mathrm{SO}3}$ in Eq. (4.24). Then, by redefining the canonical transformations to operators $a, a^\dagger$ are modified to incorporate the additional translation proportional to Q_+,

$$\begin{aligned} -i\nabla_z &= \sqrt{\tfrac{2eB_\perp}{\hbar}}\tfrac{(a-a^\dagger)}{i\sqrt{2}} \,, \\ z + z_0 \mp \frac{\hbar Q_+}{2eB_\perp} &= \tfrac{1}{\sqrt{\frac{2eB_\perp}{\hbar}}}\tfrac{(a+a^\dagger)}{\sqrt{2}} \,, \end{aligned} \tag{4.25}$$

where $-$ corresponds to $J_z = 1$ and $+$ to $J_z = -1$. Then each mode can be diagonalized independently generating the following triplet eigenvalues,

$$\tilde{\mathcal{E}}_{n,1} = \tilde{\mathcal{E}}_{n,2} = n + \tfrac{1}{2} + \tfrac{B_\varphi}{B_\perp} + \tfrac{B_{SO-}+3B_{SO3}}{2B_\perp}, \tag{4.26}$$

$$\tilde{\mathcal{E}}_{n,3} = n + \tfrac{1}{2} + \tfrac{B_\varphi}{B_\perp} + \tfrac{B_{SO-}+B_{SO3}}{B_\perp} \,, \tag{4.27}$$

Within the same approximation, the associated eigenstates are written in the tensor product space between the LL and the total angular momentum representations as $|n\rangle \bigotimes |J, J_z\rangle$. Because the modes are obtained from three different canonical transfor-

mations, Eq. (4.21) for $J_z = 0$, and Eq. (4.25) for $J_z = \pm 1$, the corresponding orbit center in the position representation is determined by the Cooperon wave vector k_x for $J_z = 0$ and $k_x \mp Q_+$ for $J_z = \pm 1$ respectively. The difference $2Q_+$ between the centers of the parallel-spin Cooperon configurations corresponds to the Q_+ separation between the k_x momenta of the single-particle states associated with the $\alpha = \beta$ regime [24]. (The Cooperon has a charge $2e$ vs. the single particle states of charge e, hence the halving of the momentum translation along $\hat{x}$.)

Phenomenologically, this situation corresponds to a decreased coupling between the triplet modes within the same Landau level as the scattering processes do not involve any spin-flipping. The original orientation of the incident particle is preserved as the electron population becomes polarized by the effective field $B_{\mathrm{SO}+}$ along the $\hat{z}$ axis.

After angular integration, Eq. (4.11) is properly modified to account for the magnetic field, i.e., $\frac{1}{2\pi}\int qdq \to \frac{1}{4\pi}\frac{4eB_\perp}{\hbar}\sum_n$, and the quantum corrections to the conductivity $\Delta\sigma(B_\perp)$ in the presence of a magnetic field are obtained,

$$\begin{aligned}\Delta\sigma(B_\perp) &\sim \sum_{n=0}^{n_m}\sum_{i=0,3}\frac{1}{\tilde{\mathcal{E}}_{n,i}} \\ &= \sum_{n=0}^{n_m}\left\{\frac{2}{n+\frac{1}{2}+\frac{B_\varphi}{B_\perp}+\frac{B_{SO-}+3B_{SO3}}{2B_\perp}}\right. \\ &\left. + \frac{1}{n+\frac{1}{2}+\frac{B_\varphi}{B_\perp}+\frac{B_{SO-}+B_{SO3}}{B_\perp}} + \frac{1}{n+\frac{1}{2}+\frac{B_\varphi}{B_\perp}}\right\}.\end{aligned} \tag{4.28}$$

which upon further manipulations (SM) leads to Eq. (4.5) in the main text. This is the main theoretical result of our work and essential for the two-stage fitting procedure used to accurately determine all the spin-orbit couplings presented here. We emphasize that the closed form expression for $\Delta\sigma(B_\perp)$ in Eq. (4.5) contains not only the Rashba, but also the linear and cubic Dresselhaus terms.

4.6.2 GaAs quantum well materials

The sample is a modulation-doped 11 nm thick GaAs/AlGaAs quantum well, grown by molecular beam epitaxy on a (001) n-doped substrate with two symmetrically placed δ doping layers, each set back 12 nm from the quantum well. The highly n-doped substrate serves as a back gate by incorporating a 600 nm thick low temperature grown GaAs barrier, which pins the Fermi level midgap [124]. This reduces the effective distance d_B from the QW to the back gate and increases the available range of gate voltages. Using wet etching, two identical Hall bars were defined with a Ti/Au gate of $300 \times 100\,\mu m^2$ on top. The 2DEG is contacted with thermally annealed low resistance GeAu/Pt contacts. The annealing parameters were carefully determined to achieve decent contact to the 2D gas without short circuiting the back gate. The top and back gate architecture allows us to keep the density in the QW constant, while changing the electric field detuning δE_z, which can be calculated in terms of the distances effective d_T and d_B and gate voltages V_T and V_B of the top- and back gate, using a simple plate capacitor model. The detuning then reads [148]:

$$\delta E_z = \frac{1}{2}\left(\frac{V_T}{d_T} - \frac{V_B}{d_B}\right). \tag{4.29}$$

The back gate range is [-3 ,1] V and [-0.3 ,0.6] V for the top gate, corresponding to a density range of [3 ,12] $\times 10^{15}\mathrm{m}^{-2}$, and mobility range [2 ,14] m^2/Vs. Individual density and mobility maps are shown in the supplementary.

4.6.3 Measurement Technique

We perform the experiments in a ^{3}He-^{4}He dilution refrigerator with a base temperature of 20 mK. We measure in a standard four-wire lock-in configuration with a time constant of 100 ms and a current bias of 100 nA, chosen to avoid self-heating, which can reduce the coherent part of the signal. After setting the gate voltages for each gate configuration gates were given 20 minutes to stabilize. To observe a clear WL/WAL signal each trace was measured at least 10-20 times and averaged.

4.6.4 Symmetry Point Determination and Value of B_{SO3}

To obtain a value of B_{SO3}, the symmetry point (i.e. $\alpha = \beta$) has to be determined first. For this we perform fits to the measured conductivity traces for all gate configurations along constant density, but replace the SO fields in the argument of Eq. (4.5) with $B^*_{\mathrm{SO}} \propto (\alpha - \beta)^2 + B_{\mathrm{SO3}}$ and the extracted value of B^*_{SO} will show a minima at $\alpha = \beta$ and we can locate the approximate position of the symmetry point for each density, where we can then estimate the value of B_{SO3} (see supplementary, Sec. 4.7.4).

4.6.5 Fit Mask

The fit mask ensures that the data points included are described by Eq. (4.5) and have the correct δE_z. We exclude data from the gate configurations in the non-linear region of the density map (see Fig. 4.3), where the contours for $V_B \lesssim -1\mathrm{V}$, start to bend. This bending corresponds to a change in the effective distance d_B to the back gate, which we use to calculate the detuning δE_z. We suspect unpinning of the Fermi level to be the reason for this change in d_B. For more positive gate voltages we exclude data from gate configurations, where the fit to the conductivity traces no longer matches the data. This gives a lower bound on the validity of Eq. (4.5) and agrees quite well with the condition $B_{SO-} \ll B_{SO+}$ (see red dashed lines in Fig. 4.3).

4.7 Supplementary Information

4.7.1 Calculation of the Quantum Corrections

The quantum corrections to the conductivity are obtained by considering that the electron states used in calculating the scattering matrix element that determines the relaxation rate are themselves modified by previous scattering processes. The coherent superposition of the (time-reversed) scattered states leads to stable transport modes associated with a decrease in the conductivity value known as the localization correction. Next we outline

the main steps in the calculation of these quantum corrections to the conductivity. We follow closely the works of Iordanskii et al. [80], Knap et al. [93] and Marinescu [167]

In the following, we assume that scattering on impurities is elastic, spin-independent, and involves only states at the Fermi surface, whose density of states per spin is $\nu_0 = m^*/2\pi\hbar^2$. The scattering matrix element $V_{\mathbf{p},\mathbf{p}'}$ of two electrons with momenta $\mathbf{p}$ and $\mathbf{p}'$, dependent only of the angle φ between the incident and scattered directions, gives rise to a scattering lifetime τ_0

$$\frac{\hbar}{\tau_0} = \nu_0 \int |V_{\mathbf{p},\mathbf{p}'}|^2(\varphi) d\varphi \ , \tag{4.30}$$

within the first Born approximation. The propagation of the particles is described by impurity averaged advanced (A) and retarded (R) Green's functions, written in terms of the single particle Hamiltonian, $H_{\mathbf{p}}$ (see Eq. (2) in the main text) as,

$$G^{\pm}(\mathbf{p}, \epsilon) = \frac{1}{\epsilon - H_{\mathbf{p}} \pm i\frac{\hbar}{2\tau_0}}. \tag{4.31}$$

As discussed in the main text, the main object in the theory of localization is the Cooperon operator, which represents an impurity averaged scattering amplitude for an electron state $\mathbf{p}$ that is almost perfectly backscattered into $\mathbf{p}' \approx -\mathbf{p}$; $\hbar\mathbf{q} = \mathbf{p} + \mathbf{p}'$, $\hbar q \ll p$ denotes deviations from the $\mathbf{p}' = -\mathbf{p}$ case. In this limit, the quantum corrections to the conductivity can be determined in terms of the Cooperon eigenvalues $C_i(\mathbf{q})$ [7, 9]

$$\Delta\sigma = -\frac{2e^2 D \tau_0^2 \nu_0}{\hbar^2} \sum_{\mathbf{q},i} C_i(\mathbf{q}) \ , \tag{4.32}$$

where $D = v_F^2\tau_1/2$ is the 2D diffusion coefficient, i indexes the singlet and triplet spin states (to be discussed further below), v_F the Fermi velocity and τ_1 the transport scattering time. The anisotropy of the scattering matrix element $V_{\mathbf{p},\mathbf{p}'}$ [50] results in a series of transport times, of which τ_1 is the first ($n = 1$), defined by

$$\frac{\hbar}{\tau_n} = \nu_0 \int |V_{\mathbf{p},\mathbf{p}'}|^2(1 - \cos n\varphi) d\varphi \ , \tag{4.33}$$

with $n = 1, 2, 3...$ The impurity mediated Cooperon equation is

$$C_{\mathbf{p},\mathbf{p}'}(\mathbf{q}) = |V_{\mathbf{p},\mathbf{p}'}|^2 + \sum_{\mathbf{p}''} |V_{\mathbf{p},\mathbf{p}''}|^2 G^+_{-\mathbf{p}''+\hbar\mathbf{q},\epsilon+\hbar\omega} G^-_{\mathbf{p}'',\epsilon} C_{\mathbf{p}'',\mathbf{p}'} \ . \tag{4.34}$$

To proceed, we first integrate the kernel in Eq. (4.34) over the kinetic energy $p^2/2m^*$ in the complex plane then expand the result in terms of the scattering rate $\hbar/\tau_0$, the leading term in the denominator. Since after many scattering events the spin directions of the two electron spins traveling along time-reversed paths are completely uncorrelated, we label them by distinct indices σ and ρ, respectively. Thus Eq. (4.34) becomes,

$$\begin{aligned} C_{\mathbf{p},\mathbf{p}'}(\mathbf{q}) = |V_{\mathbf{p},\mathbf{p}''}|^2 + \nu_0 \int_0^{2\pi} d\varphi_{\mathbf{p}''} |V(\varphi_p - \varphi_{p''})|^2 \Big\{ & 1 + i\omega\tau_0 + i\mathbf{q}\cdot\mathbf{v}_{\mathbf{p}''}\tau_0 - (i\mathbf{q}\cdot\mathbf{v}_{\mathbf{p}''})^2\tau_0^2 \\ & + \left[i\mathbf{\Omega}_{\mathbf{p}''} \times (\sigma+\rho)\cdot\hat{y}\right]\tau_0 - \left[i\mathbf{\Omega}_{\mathbf{p}''} \times (\sigma+\rho)\cdot\hat{y}\right]^2\tau_0^2 \\ & - 2\left(\mathbf{q}\cdot\mathbf{v}_{\mathbf{p}''}\right)\left[\mathbf{\Omega}_{\mathbf{p}''} \times (\sigma+\rho)\cdot\hat{y}\right]\tau_0^2 \Big\} C_{\mathbf{p}'',\mathbf{p}'}. \end{aligned} \tag{4.35}$$

Let us now search for an iterative solution by expanding the Cooperon in terms of harmonics: $C_{\mathbf{p},\mathbf{p}'}(q) = C^{(0)}_{\mathbf{p},\mathbf{p}'}(q) + C^{(1)}_{\mathbf{p},\mathbf{p}'}(q)\cos\varphi_{\mathbf{p}} + C^{(2)}_{\mathbf{p},\mathbf{p}'}(q)\cos 2\varphi_{\mathbf{p}} + \ldots$, with φ_p being the angle between $\hbar\mathbf{q} = \mathbf{p} + \mathbf{p}'$ and $\mathbf{p}$. The first order correction $C^{(1)}_{\mathbf{p},\mathbf{p}'}(q)$ is readily written in terms of the components of total spin $\mathbf{J} = (\sigma+\rho)/2$ (in $\hbar$ units) of the two electrons

$$\begin{aligned} \int_0^{2\pi} d\varphi_{\mathbf{p}''} |V(\varphi_{\mathbf{p}} - \varphi_{\mathbf{p}''})|^2 \{ & vq\cos\varphi_{p''} \\ & + 2\left[(\alpha-\beta)\sin\varphi_{\mathbf{p}''} - \beta_3\sin 3\varphi_{\mathbf{p}''}\right] J_x \\ & - 2\left[(\alpha+\beta)\cos\varphi_{\mathbf{p}''} - \beta_3\cos 3\varphi_{\mathbf{p}''}\right] J_z \} \ . \end{aligned} \tag{4.36}$$

Here $\varphi_{\mathbf{p}''}$ is the angle between $\mathbf{p}''$ and $\mathbf{q}$, i.e., the same angular dependence of $C_{\mathbf{p}'',\mathbf{p}'}(\mathbf{q})$.

Noticing that

$$\begin{aligned}
&\nu_0 \int_0^{2\pi} d\varphi_{\mathbf{p}''} |V(\varphi_{\mathbf{p}} - \varphi_{\mathbf{p}''})|^2 \cos n\varphi_{\mathbf{p}''} \\
&= \nu_0 \int_0^{2\pi} d\varphi |V(\varphi_{\mathbf{p}} - \varphi_{\mathbf{p}''})|^2 \cos n(\varphi_{\mathbf{p}} - \varphi_{\mathbf{p}''}) \cos n\varphi_{\mathbf{p}} \\
&= \cos n\varphi_{\mathbf{p}} \left(\frac{1}{\tau_0} - \frac{1}{\tau_n} \right) \\
&= \frac{(\tau_n - \tau_0)}{\tau_0 \tau_n} \cos n\varphi_{\mathbf{p}} \approx \frac{(\tau_n - \tau_0)}{\tau_0^2} \cos n\varphi_{\mathbf{p}}
\end{aligned} \tag{4.37}$$

with τ_1 and τ_3 given by Eq. (4.33), we can cast the first-order correction to the Cooperon in the form

$$\begin{aligned}
C^{(1)} &= i(\tau_1 - \tau_0) \left[\mathbf{v}_{\mathbf{p}''} \cdot \mathbf{q} + 2(\alpha - \beta) J_x \sin \varphi_{\mathbf{p}''} \right. \\
&- \left. 2(\alpha + \beta) J_z \cos \varphi_{\mathbf{p}''} \right] \\
&- i(\tau_3 - \tau_0) \left(-2\beta_3 J_x \sin 3\varphi_{\mathbf{p}''} + 2\beta_3 J_z \cos 3\varphi_{\mathbf{p}''} \right) C^{(0)} \ .
\end{aligned} \tag{4.38}$$

Upon inserting $C = C^{(0)} + C^{(1)}$ in the kernel of Eq. (4.34) and performing some simplifications, all contributions proportional to τ_0 drop out. A further linearization of Eq. (4.34) yields the lowest order expression the for zeroth-order harmonic of the Cooperon

$$C^{(0)}_{\mathbf{p},\mathbf{p}'}(\mathbf{q}) = \frac{|V_{\mathbf{p},\mathbf{p}'}|^2}{\tau_0 \mathcal{H}} \ , \tag{4.39}$$

where $\mathcal{H}$ is an operator in the 4-dimensional space associated with the total angular momentum J, corresponding to the addition of the two spins, reading

$$\begin{aligned}
\mathcal{H} &= Dq^2 + \frac{1}{\tau_\varphi} + 2k_F^2 \left[(\alpha + \beta)^2 \tau_1 + \beta_3^2 \tau_3 \right] J_z^2 \\
&+ 2k_F^2 \left[(\alpha - \beta)^2 \tau_1 + \beta_3^2 \tau_3 \right] J_x^2 \\
&+ 2k_F (\alpha - \beta) \tau_1 v q_z J_x - 2k_F (\alpha + \beta) \tau_1 v q_x J_z \ .
\end{aligned} \tag{4.40}$$

where we have replaced $-i\omega$ by $1/\tau_\varphi$, the dephasing time, a descriptor of the inelasticity

of the propagation. For convenience we introduce the following parameters

$$\begin{aligned} Q_{\pm} &= \frac{2m^*(\alpha \pm \beta)}{\hbar^2} , \\ Q_3 &= \frac{2m^*\beta_3}{\hbar^2}\sqrt{\frac{\tau_3}{\tau_1}} . \end{aligned} \tag{4.41}$$

We can then recast $\mathcal{H}$ as

$$\begin{aligned} \mathcal{H} &= Dq^2 + \frac{1}{\tau_\varphi} + D\left\{\left[Q_+^2 + Q_3^2\right] J_z^2 + \left[Q_-^2 + Q_3^2\right] J_x^2 \right. \\ &+ \left. 2Q_- q_z J_x - 2Q_+ q_x J_z\right\} . \end{aligned} \tag{4.42}$$

At this point we can diagonalize $\mathcal{H}$ and easily find eigenvalues $C_i(\mathbf{q})$ of the Cooperon operator (via Eq. 4.39) and from Eq. 4.32 determine the weak localization corrections [80]. In the next section we generalize the above procedure by including a magnetic field, essential for probing weak localization experimentally, and outline the derivation of the general weak-localization formula first derived in this work (see Eq. (4.5) in the main text).

4.7.2 Quantum Corrections in Presence of a Magnetic Field

In the presence of a quantizing magnetic field, the position representation of the Green's function $G^{\pm}(\mathbf{r}, \mathbf{r}')$ is modified as [79]

$$\tilde{G}^{\pm}(\mathbf{r}, \mathbf{r}') = e^{\frac{ie}{\hbar}\int_{\mathbf{r}}^{\mathbf{r}'} \mathbf{A}(\mathbf{l})\cdot d\mathbf{l}} G^{\pm}(\mathbf{r}, \mathbf{r}') , \tag{4.43}$$

a good approximation when the Landau orbit is larger than the Fermi wavelength. Because of this approximation for the Green's functions, it is convenient to work in position representation. By following essentially the same protocol as in the previous section, i.e., from Eqs. (4.34) to (4.39), but now in the position representation, we find that the denominator of the zeroth-order Cooperon acquires a phase (i.e., $\mathcal{H} \to \tilde{\mathcal{H}}$ in Eq. 4.39)

$$\tilde{\mathcal{H}}(\mathbf{r}, \mathbf{r}') = e^{i\frac{2e}{\hbar}\int_{\mathbf{r}}^{\mathbf{r}'} \mathbf{A}(\mathbf{l})\cdot d\mathbf{l}} \mathcal{H}(\mathbf{r}, \mathbf{r}') , \tag{4.44}$$

where the Fourier transform of $\mathcal{H}$ in the absence of the magnetic field is given in Eq. (4.42). This approximation is correct for $|\mathbf{r}-\mathbf{r}'| \ll l$, where l is the mean free path. In this case, the integral defining the phase in Eq. 4.44 can be linearized to $\mathbf{A}\cdot(\mathbf{r}'-\mathbf{r})$. Now we can solve the generalized eigenfunction-eigenvalue equation for $\mathcal{H}(\mathbf{r},\mathbf{r}')$,

$$\int e^{i\frac{2e}{\hbar}\mathbf{A}\cdot(\mathbf{r}'-\mathbf{r})}\mathcal{H}(\mathbf{r},\mathbf{r}')\psi(\mathbf{r}')d\mathbf{r}' = \mathcal{E}\psi(\mathbf{r}) \ , \tag{4.45}$$

by taking advantage that the difference $\Delta\mathbf{r} = \mathbf{r}' - \mathbf{r}$ is small so that the integrand above can be expanded as a power series of $\Delta\mathbf{r}$. The kernel of the integral equation becomes,

$$\begin{aligned}
&\mathcal{H}(\mathbf{r}'-\mathbf{r})\left[1 + i\frac{2e}{\hbar}\mathbf{A}\cdot\Delta\mathbf{r} + \frac{1}{2}\left(i\frac{2e}{\hbar}\mathbf{A}\cdot\Delta\mathbf{r}\right)^2\right] \\
&\times\left[\psi(\mathbf{r}) + \nabla\psi\cdot\Delta\mathbf{r} + \frac{1}{2}(\nabla\psi\cdot\mathbf{A})\right] \\
&= \mathcal{H}(\mathbf{r}'-\mathbf{r})\left\{1 + \left(\nabla + i\frac{2e}{\hbar}\mathbf{A}\right)\cdot\Delta\mathbf{r}\right. \\
&\left. + \frac{1}{2}\left[\left(\nabla + i\frac{2e}{\hbar}\mathbf{A}\right)\cdot\Delta\mathbf{r}\right]^2\right\}\psi(\mathbf{r}) \ .
\end{aligned} \tag{4.46}$$

By using the identity

$$\int d\mathbf{r}'\mathcal{H}(\mathbf{r}'-\mathbf{r})\,(\Delta\mathbf{r})^n = \frac{\partial^n\mathcal{H}(\mathbf{q})}{i^n\partial q^n}\,|_{\mathbf{q}=0} \ . \tag{4.47}$$

we can recast the expanded eigenfunction-eigenvalue equation for $\mathcal{H}(\mathbf{r},\mathbf{r}')$ in the form

$$\begin{aligned}
&\left\{1 + \left(-i\nabla + \frac{2e}{\hbar}\mathbf{A}\right)\cdot\nabla_{\mathbf{q}}\right. \\
+ \quad &\left.\frac{1}{2}\left[\left(-i\nabla + \frac{2e}{\hbar}\mathbf{A}\right)\cdot\nabla_q\right]^2\right\}\mathcal{H}\,|_{\mathbf{q}=0}\,\psi(\mathbf{r}) \\
= \quad &\mathcal{E}\psi(\mathbf{r}) \ .
\end{aligned} \tag{4.48}$$

We consider a magnetic field $\mathbf{B}$ along the $\hat{y}$ axis. In the Landau gauge, $\mathbf{B}$ can be expressed as the curl of the vector potential $\mathbf{A} = \{A_x = B_\perp z, A_y = 0, A_z = 0\}$. Hence Eq. (4.48)

becomes

$$\begin{aligned} & \left\{ \frac{1}{\tau_\varphi} + D\left[Q_+^2 + Q_3^2\right] J_z^2 + \left[Q_-^2 + Q_3^2\right] J_x^2 \right. \\ - \quad & 2DQ_+ J_z \left(-i\nabla_x + \frac{2eB_\perp}{\hbar} z\right) + 2DQ_- J_x \left(-i\nabla_z\right) \\ + \quad & \left. D\left(-i\nabla_x + \frac{2eB_\perp}{\hbar} z\right)^2 + D\left(-i\nabla_z\right)^2 \right\} \psi(\mathbf{r}) = \mathcal{E}\psi(\mathbf{r}), \end{aligned} \tag{4.49}$$

with $\mathcal{H}(\mathbf{q})$ and its derivatives obtained from Eq.(4.42). We now introduce $z_0 = k_x\hbar/2eB$ (k_x is the Cooperon wavevector along the $\hat{x}$ direction) and define the canonical transformation,

$$\begin{aligned} -i\nabla_z &= \sqrt{\tfrac{2eB_\perp}{\hbar}} \tfrac{(a-a^\dagger)}{i\sqrt{2}} \ , \\ z + z_0 &= \tfrac{1}{\sqrt{\frac{2eB_\perp}{\hbar}}} \tfrac{(a+a^\dagger)}{\sqrt{2}} \ , \end{aligned} \tag{4.50}$$

so as to write Eq. (4.49) into the number representation,

$$\begin{aligned} & \left\{ \frac{1}{\tau_\varphi} + D\left(Q_+^2 + Q_3^2\right) J_z^2 + \left(Q_-^2 + Q_3^2\right) J_x^2 \right. \\ - \quad & DQ_+ J_z \sqrt{\frac{4eB_\perp}{\hbar}} (a + a^\dagger) - iDQ_- J_x \sqrt{\frac{4eB_\perp}{\hbar}} (a - a^\dagger) \\ + \quad & \left. D\left(\frac{4eB_\perp}{\hbar}\right)\left(a^\dagger a + \frac{1}{2}\right) \right\} |u\rangle = \mathcal{E}|u\rangle \ , \end{aligned} \tag{4.51}$$

where $|u\rangle$ is the corresponding eigenket. Equation (4.51) maintains the structure of the original Cooperon in spin space (c.f. the corresponding eigenvalue equation for $\mathcal{H}$ in Eq. 4.42), with q^2 being replaced by $\frac{4eB_\perp}{\hbar}\left(a^\dagger a + \frac{1}{2}\right)$, while its components q_x and q_z were replaced by $\sqrt{\frac{4eB_\perp}{\hbar}}(a + a^\dagger)/2$ and $\sqrt{\frac{4eB_\perp}{\hbar}}(a - a^\dagger)/2i$ respectively. To simplify our notation, in what follows we introduce the following effective magnetic fields [80]: $B_\varphi = \hbar/4eD\tau_\varphi$, $B_{SO+} = \hbar Q_+^2/4e$, $B_{SO-} = \hbar Q_-^2/4e$, $B_{SO3} = \hbar Q_3^2/4e$, $B_{tr} = \hbar/4eD\tau_1$. Note that the solution of Eq. (4.51) is obtained as a spinor in the 4-dimensional spin space corresponding to the tensor product of the two spin operators associated with the incident

and scattered particle, respectively. In what follow we work on the basis J, J_z of the total angular momentum $J = 0$ and $J = 1$ and their corresponding z-components $J_z = 0$ and $J_z = 1, 0 - 1$.

The *singlet* $J = 0$, $J_z = 0$ solution is immediately factored, as it is diagonal both in the spin and Landau level spaces. The n-th singlet Landau eingenvalue is

$$\mathcal{E}_0 = \frac{4DeB_\perp}{\hbar}\left(n + \frac{1}{2} + \frac{B_\varphi}{B_\perp}\right) , \tag{4.52}$$

or

$$\tilde{\mathcal{E}}_{n,0} = \frac{\mathcal{E}_0}{\frac{4DeB_\perp}{\hbar}} = \left(n + \frac{1}{2} + \frac{B_\varphi}{B_\perp}\right) , \tag{4.53}$$

The *triplet* solutions can be obtained from Eq. (4.51) (with $4eDB_\perp/\hbar$ factored out) written as a 3×3 matrix in the basis of $J = 1$, $J_z = 1, 0, -1$ via

$$\begin{vmatrix} \frac{B_\varphi}{B_\perp} + \frac{B_{SO+}}{B_\perp} + \frac{B_{SO-}+3B_{SO3}}{2B_\perp} & -i\sqrt{\frac{B_{SO-}}{2B_\perp}}(a - a^\dagger) & \frac{B_{SO-}+B_{SO3}}{2B_\perp} \\ +a^\dagger a + \frac{1}{2} - \sqrt{\frac{B_{SO+}}{B_\perp}}(a + a^\dagger) - \tilde{\mathcal{E}} & & \\ -i\sqrt{\frac{B_{SO-}}{2B_\perp}}(a - a^\dagger) & \frac{B_\varphi}{B_\perp} + \frac{B_{SO-}+B_{SO3}}{B} + a^\dagger a + \frac{1}{2} - \tilde{\mathcal{E}} & -i\sqrt{\frac{B_{SO-}}{2B_\perp}}(a - a^\dagger) \\ \frac{B_{SO-}+B_{SO3}}{2B_\perp} & -i\sqrt{\frac{B_{SO-}}{2B_\perp}}(a - a^\dagger) & \frac{B_\varphi}{B_\perp} + \frac{B_{SO+}}{B_\perp} + \frac{B_{SO-}+3B_{SO3}}{2B_\perp} \\ & & +a^\dagger a + \frac{1}{2} + \sqrt{\frac{B_{SO+}}{B_\perp}}(a + a^\dagger) - \tilde{\mathcal{E}} \end{vmatrix} = 0 , \tag{4.54}$$

where $\tilde{\mathcal{E}} = \mathcal{E}/(4DeB_\perp/\hbar)$.

In the limit where the two linear SOI constants are almost equal, $B_{SO-} \ll B_{SO+}$ and $B_{SO3} \ll B_{SO+}$, we can justifiably drop all off-diagonal terms proportional with B_{SO-} or $B_{SO-} + B_{SO3}$ in Eq. (4.54). This regime corresponds to a decreased coupling between the triplet modes within the same Landau level as the scattering processes do not involve spin flip. The original orientation of the incident particle is preserved as the electron population becomes polarized by the effective field B_{SO+} along the $\hat{z}$ axis. As a further simplification, we perform another canonical transformations on the operators $a, a^\dagger$ in

order to incorporate the additional translation proportional to Q_+,

$$\begin{aligned} -i\nabla_z &= \sqrt{\tfrac{2eB_\perp}{\hbar}}\tfrac{(a-a^\dagger)}{i\sqrt{2}} \ , \\ z + z_0 \mp \frac{\hbar Q_+}{2eB_\perp} &= \tfrac{1}{\sqrt{\frac{2eB_\perp}{\hbar}}}\tfrac{(a+a^\dagger)}{\sqrt{2}} \ , \end{aligned} \tag{4.55}$$

where $\mp$ correspond to $J_z = \pm 1$, respectively.

The diagonalization of Eq. (4.54) can be done separately for each spin mode straightforwardly as the determinant is diagonal. We find

$$\tilde{\mathcal{E}}_{n,1} = \tilde{\mathcal{E}}_{n,2} = n + \tfrac{1}{2} + \tfrac{B_\varphi}{B_\perp} + \tfrac{B_{SO-}+3B_{SO3}}{2B_\perp}, \tag{4.56}$$

$$\tilde{\mathcal{E}}_{n,3} = n + \tfrac{1}{2} + \tfrac{B_\varphi}{B_\perp} + \tfrac{B_{SO-}+B_{SO3}}{B_\perp} \ , \tag{4.57}$$

where for convenience we have indexed the eigenvalues as $\tilde{\mathcal{E}}_{n,1}$, $i = 1, 2, 3$ corresponding to the triplets with $J_z = 1, -1, 0$.

To calculate the corrections to the conductivity associated with Landau level diagonal modes we have to replace the integral over $\mathbf{q}$ in Eq. 4.32 by a discrete sum over the occupied Landau levels, i.e.,

$$\frac{1}{2\pi}\int_0^{q_{max}} q dq \to \frac{1}{4\pi}\frac{4eB_\perp}{\hbar}\sum_{n=0}^{n_m} \ , \tag{4.58}$$

where we have used $q^2 = \frac{4eB_\perp}{\hbar}\left(n + \frac{1}{2}\right)$ (q^2 is quantized) thus leading to $2qdq = \frac{4eB_\perp}{\hbar}\Delta n = \frac{4eB_\perp}{\hbar}$, since $\Delta n = 1$ (the minimum variation in the sum over n). n_m is given from the condition $q_{max}^2 = \frac{4eB_\perp}{\hbar} n_m = (D\tau_1)^{-1}$, which is the maximum momentum exchanged allowed given by the transport time in the diffusion approximation. This gives $n_m = \hbar/(4eB_\perp D\tau_1) = B_{tr}/B_\perp$. Following the angular integration of Eq. (4.39), by using

Eqs. (4.53) and (4.56), we obtain

$$\Delta\sigma \sim \sum_{n=0}^{n_m} \sum_{i=0,3} \quad \frac{1}{\tilde{\mathcal{E}}_{n,i}} = \sum_{n=0}^{n_m} \left\{ \frac{2}{n+\frac{1}{2}+\frac{B_\varphi}{B_\perp}+\frac{B_{SO-}+3B_{SO3}}{2B_\perp}} + \frac{1}{n+\frac{1}{2}+\frac{B_\varphi}{B_\perp}+\frac{B_{SO-}+B_{SO3}}{B_\perp}} + \frac{1}{n+\frac{1}{2}+\frac{B_\varphi}{B_\perp}} \right\} . \tag{4.59}$$

Since we consider $n_m \gg 1$, we can manipulate the sums over n in the following way. For properly defined a's, the sums in Eq. (4.59) have the generic form

$$\begin{aligned} \sum_{n=0}^{n_m} \frac{1}{n+a} &= \sum_{n=0}^{n_m} \frac{1}{n+a} - \sum_{n=1}^{n_m} \frac{1}{n} + \sum_{n=1}^{n_m} \frac{1}{n} \\ &= -\sum_{n=1}^{n_m} \frac{a-1}{n(n+a-1)} + C + \ln n_m \\ &= -\Psi(a) + \ln n_m \ , \end{aligned} \tag{4.60}$$

where we have used the definition of the Euler constant C,

$$C = \lim_{n\to\infty} \left(\sum_{k=1}^{n} \frac{1}{k} - \ln n \right) \ , \tag{4.61}$$

and of the Digamma function,

$$\Psi(a+1) = -C + \sum_{n=1}^{\infty} \frac{a}{n(n+a)} \ . \tag{4.62}$$

Final formula for the weak localization corrections. Following the algorithm outlined above, we obtain the corrections to the conductivity as

$$\begin{aligned} \Delta\sigma(B_\perp) = -\frac{e^2}{4\pi^2\hbar} \Bigg[&\Psi\left(\frac{1}{2}+\frac{B_\varphi}{B_\perp}\right) + 2\ln\frac{B_{\rm tr}}{B_\perp} - 2\Psi\left(\frac{1}{2}+\frac{B_\varphi}{B_\perp}+\frac{B_{SO-}+3B_{SO3}}{2B_\perp}\right) \\ &-\Psi\left(\frac{1}{2}+\frac{B_\varphi}{B_\perp}+\frac{B_{SO-}+B_{SO3}}{B_\perp}\right)\Bigg] . \end{aligned} \tag{4.63}$$

The closed-form formula in Eq. (4.63) (same as Eq. (4.5) in the main text) is the main theoretical result of this paper. It plays a crucial role in the two-stage fitting procedure we have used to accurately extract all the SO parameters from our thorough weak (anti)

localization measurements. We note that (4.63) accounts not only for the linear Rashba and Dresselhaus contributions but also for the cubic Dresselhaus term.

4.7.3 Full Account of Data

Summary of extracted data

We first summarize the extracted values of the SO parameters α_0, α_1 and γ, the scattering time ratio τ_3/τ_1 and the effective distances d_T and d_B for each sample. The values of d_T and d_B are extracted from fits to the density map over the same range of gate voltages, where the contours of constant density are linear. We note that the value of d_B in measurement #5 & #6 is smaller, because measurement #5 corresponds to a different cooldown and measurement #6 to a different sample and wafer. The epitaxial values of d_T and d_B are 75 nm and 1210 nm. The significantly smaller value of d_B is due to the low temperature grown GaAs buffer layer of 600 nm.

Table 4: All relevant extracted data for the different samples.

Measurement #	Sample	α_0 [meVÅ]	α_1 [eÅ^2]	γ [eVÅ^3]	τ_3/τ_1	d_T [nm]	d_B [nm]
1	11 nm - I	1.7±0.6	9.3±0.3	13.4±1.2	0.21	107	750
2	11 nm - II	1.3±1.0	9.4±0.3	12.3±2.0	0.24	101	765
3	11 nm - I	0.9±0.7	9.8±0.2	10.2±1.4	0.37	107	750
4	11 nm - II	0.4±1.3	9.9±0.4	8.6±2.4	0.47	101	765
5	11 nm - II	1.6±1.4	8.4±0.3	12.8±2.7	0.23	102	736
6	9.3 nm - III	5.5±0.4	9.0±0.1	15.3±0.7	0.16	100	710

The following figures are organized as follows: The density map is shown in panel (a), with the contours indicating the respective value of the density (in multiples of $10^{15}\,\mathrm{m}^{-2}$). The markers correspond to the manually determined symmetry points, the line in the same color corresponds to the expected symmetry points from the extracted SO parameters and the broken blue line corresponds to the expected symmetry points using the average

of the extracted SO parameters. Panel (b) shows the contours of constant mobility with its values indicated in m^2/Vs. Panel (c) shows the fits to the WAL traces at $\alpha \approx \beta$ for all measured densities. Panel (d) shows the extracted values of B_{SO3}, B_φ, τ_3/τ_1 and τ_φ for the measured densities. Panel (e) and (f) show the extracted values of B_{SO-} (green markers) and its fit (blue line) for each density, indicated in multiples of $10^{15}\,m^{-2}$.

Dataset 1.

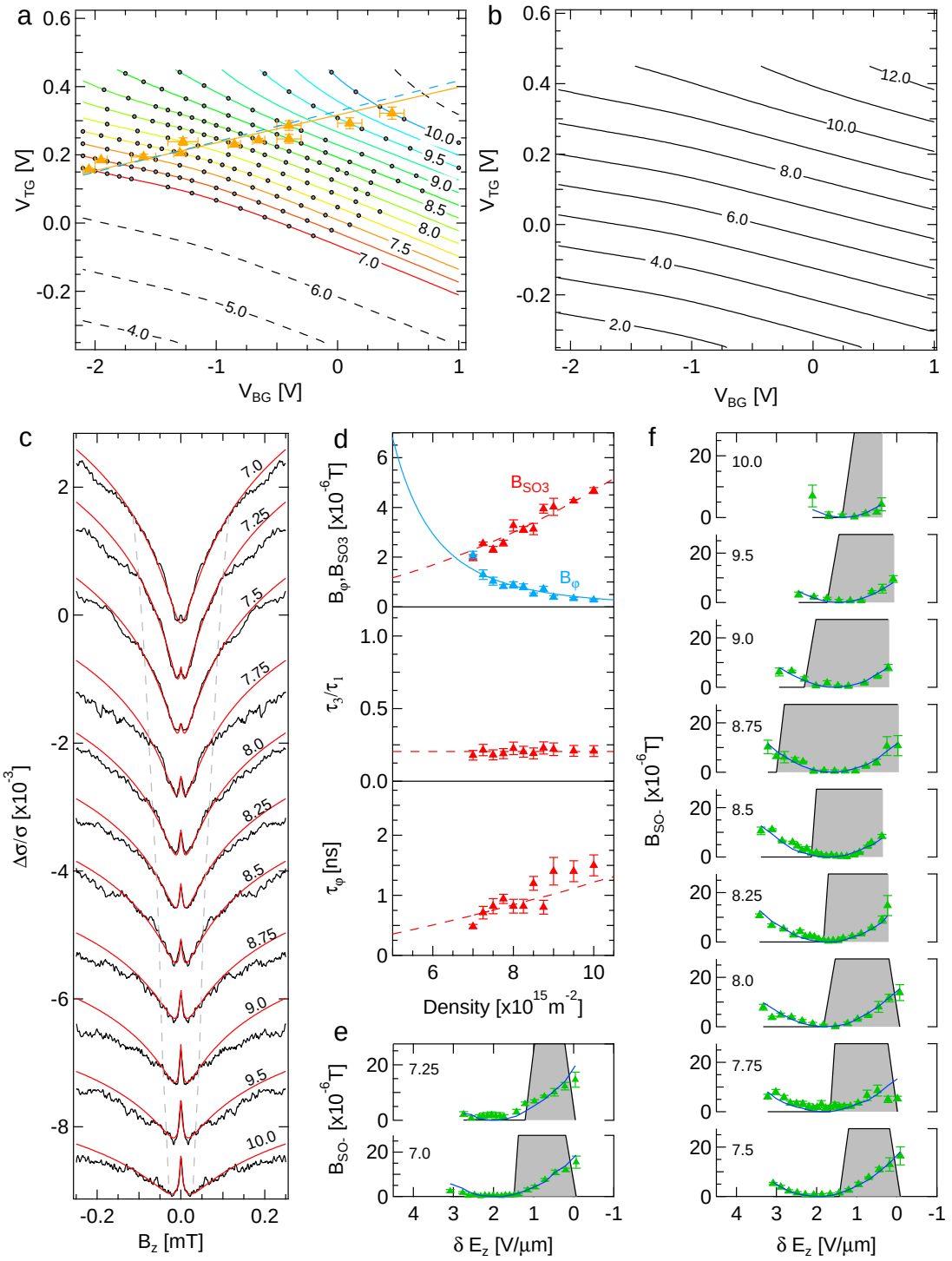

Figure 4.7: First measurement on sample I. Gate configurations were measured not in a particular order and their spacing in back gate voltage is not equidistant, because at this stage the method how to aquire data most reliably, was still in development.

Dataset 2.

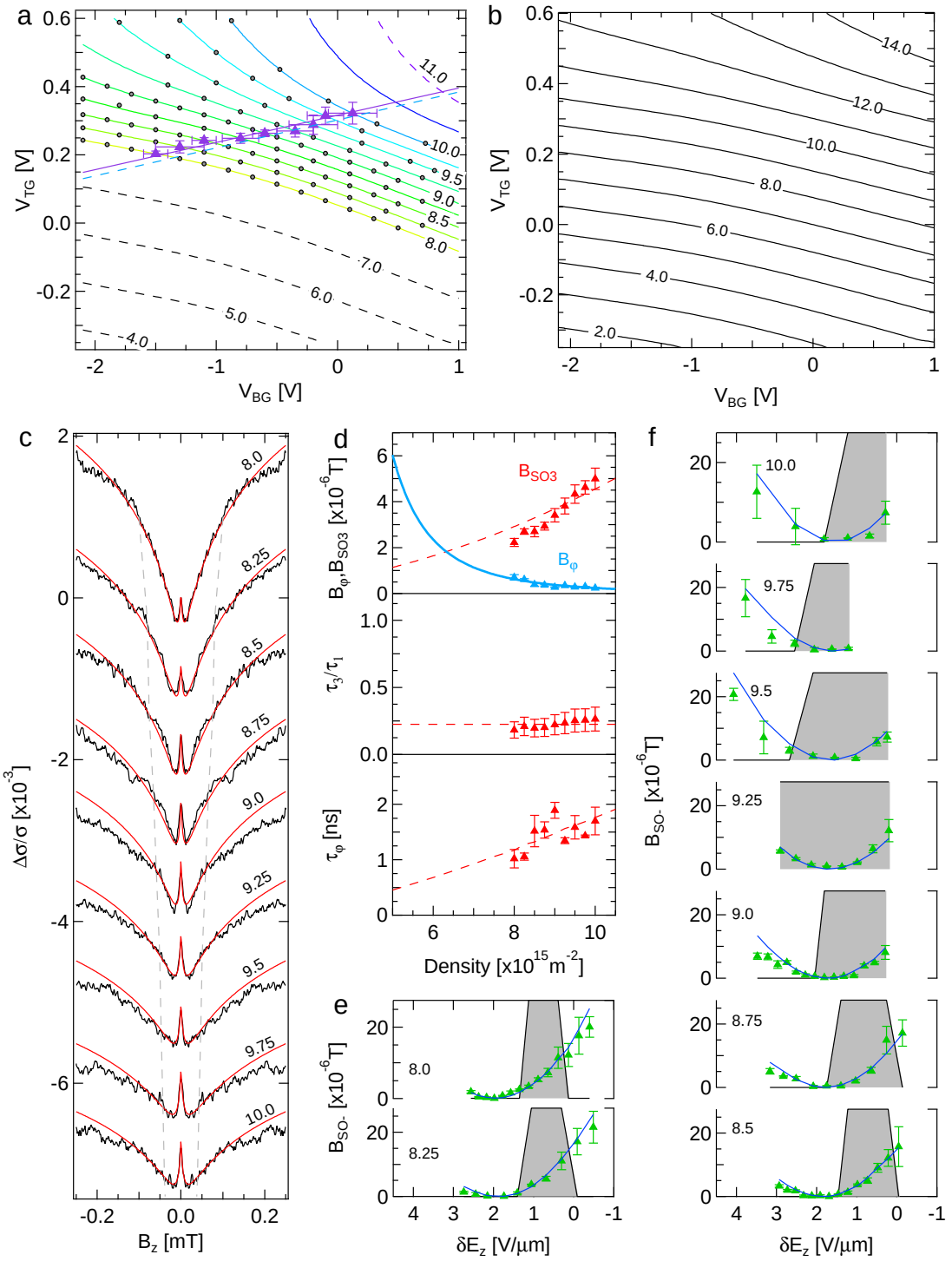

Figure 4.8: First measurement on sample II. The mobility is slightly higher as in sample I. Data are taken sequentially and back gate voltage spacing is chosen to be the same for each density.

Dataset 3.

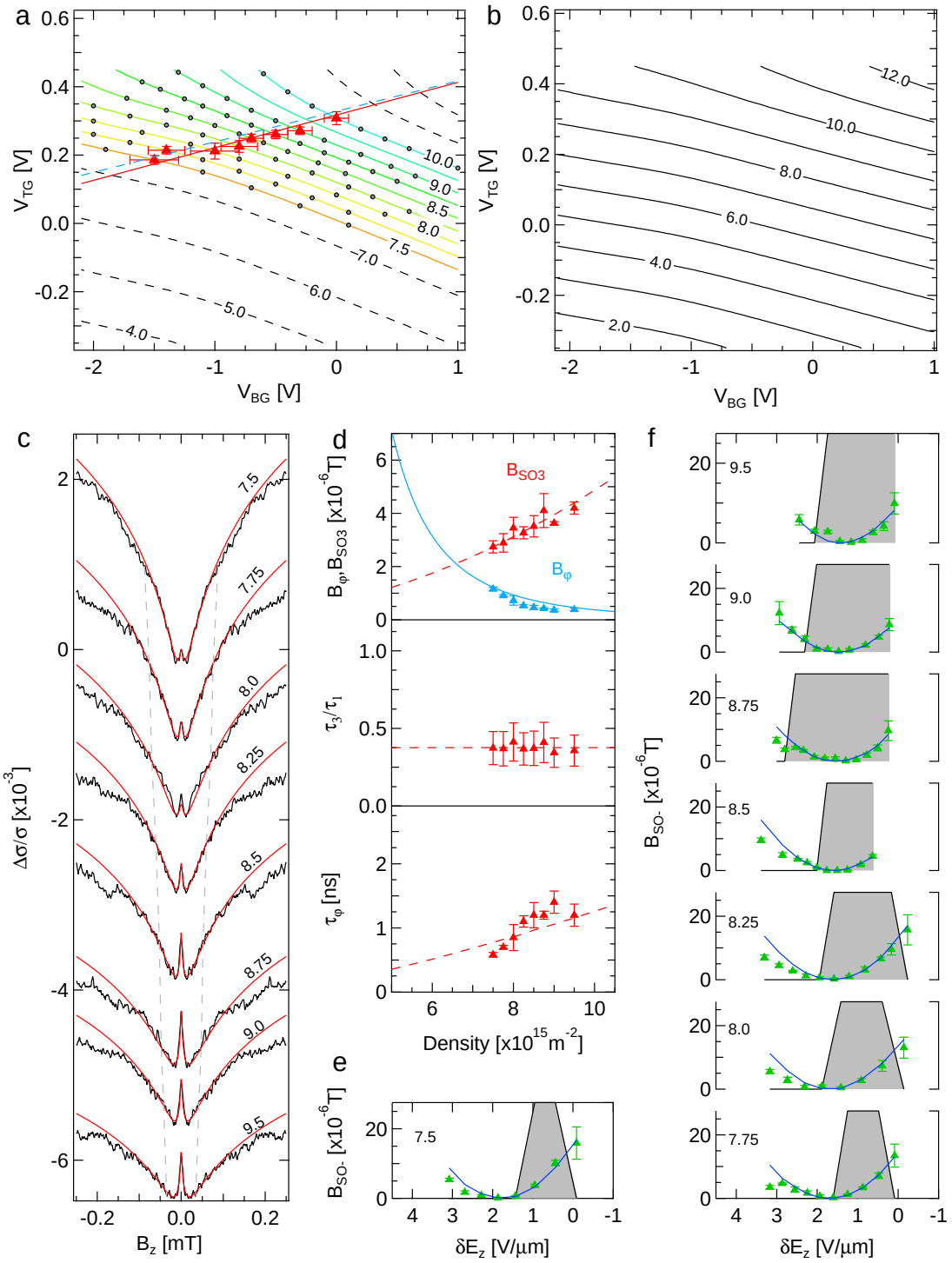

Figure 4.9: Second measurement on sample I, the data are aquired here as in the case of dataset 2. The spacing between the gate configurations is the same for each density.

Dataset 4.

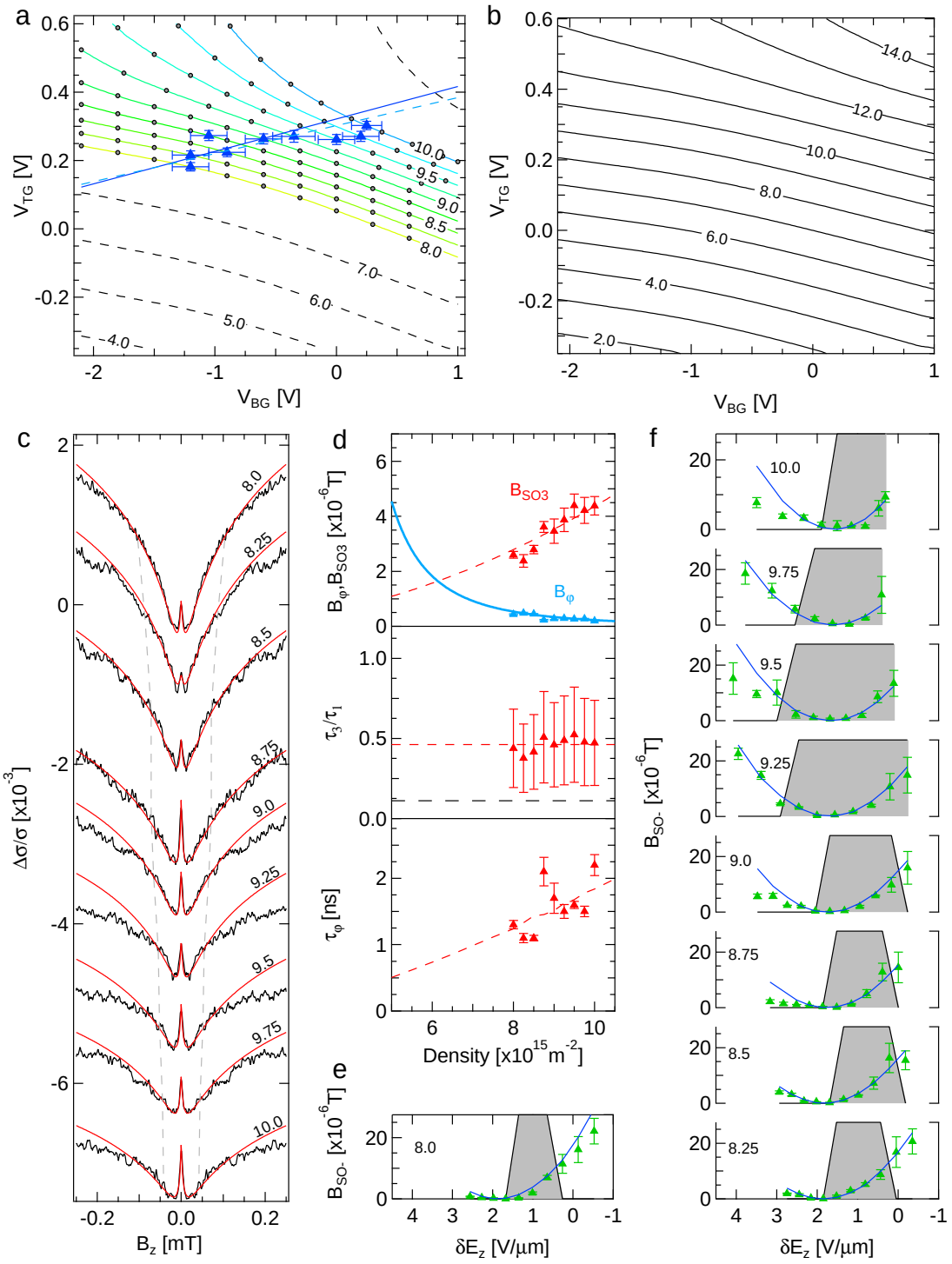

Figure 4.10: Second measurement on sample II, as in the previous measurements. Panel (d) middle: The error bars on τ_3/τ_1 are so large because of the low value of $\gamma \sim 8.6$ eVÅ^3. The black dashed line corresponds to the theoretical minimum of τ_3/τ_1.

Dataset 5.

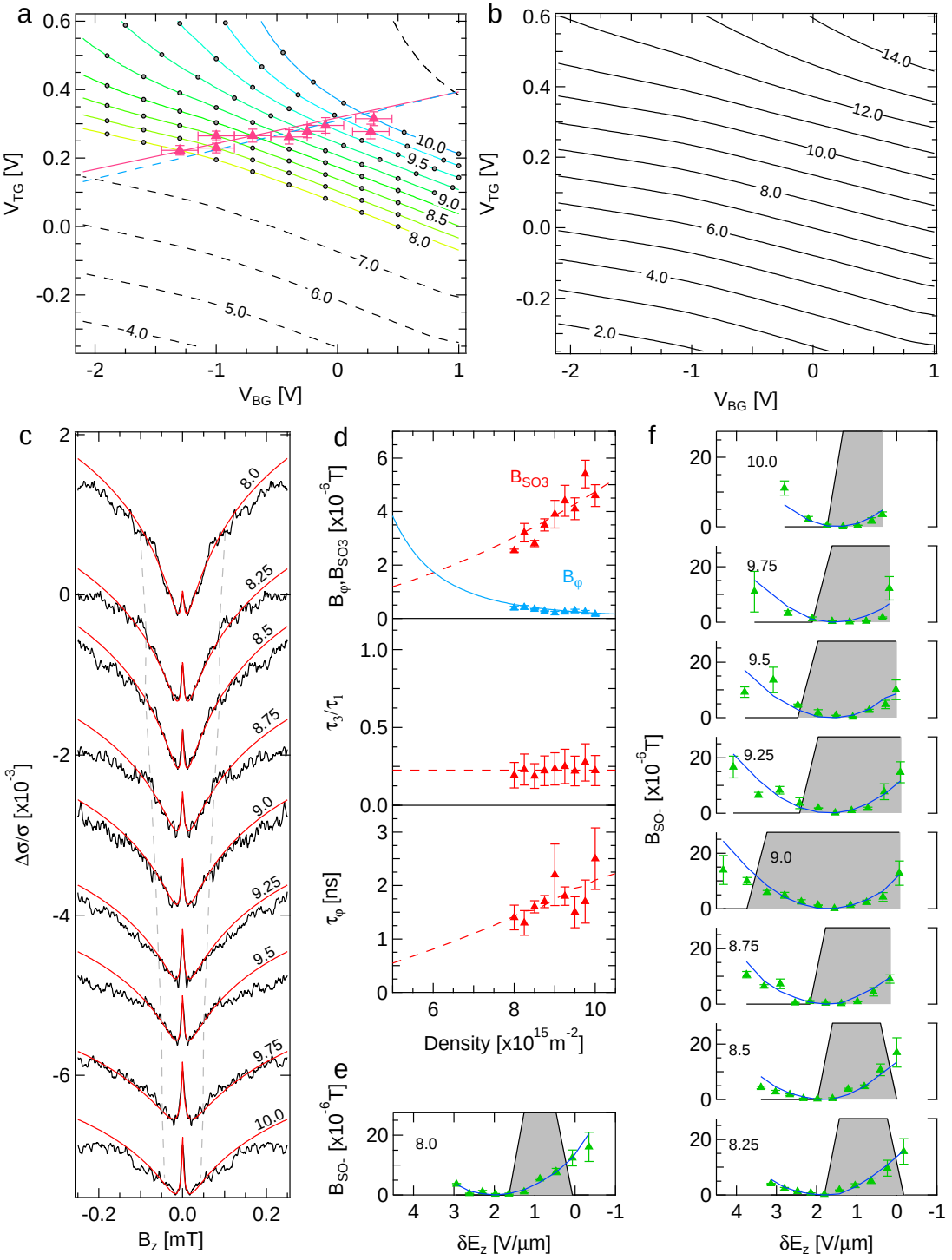

Figure 4.11: Third measurement on sample II in another cooldown.

Dataset 6. Data from another wafer, which is doped asymmetrically and has a 9.3 nm thick QW. The densities are much lower in this wafer resulting in a full suppression of WAL at $\alpha \approx \beta$. The extracted SO values are within the range of the expected values for this wafer, except the value of γ, which is larger than expected and we do not understand it fully at this point.

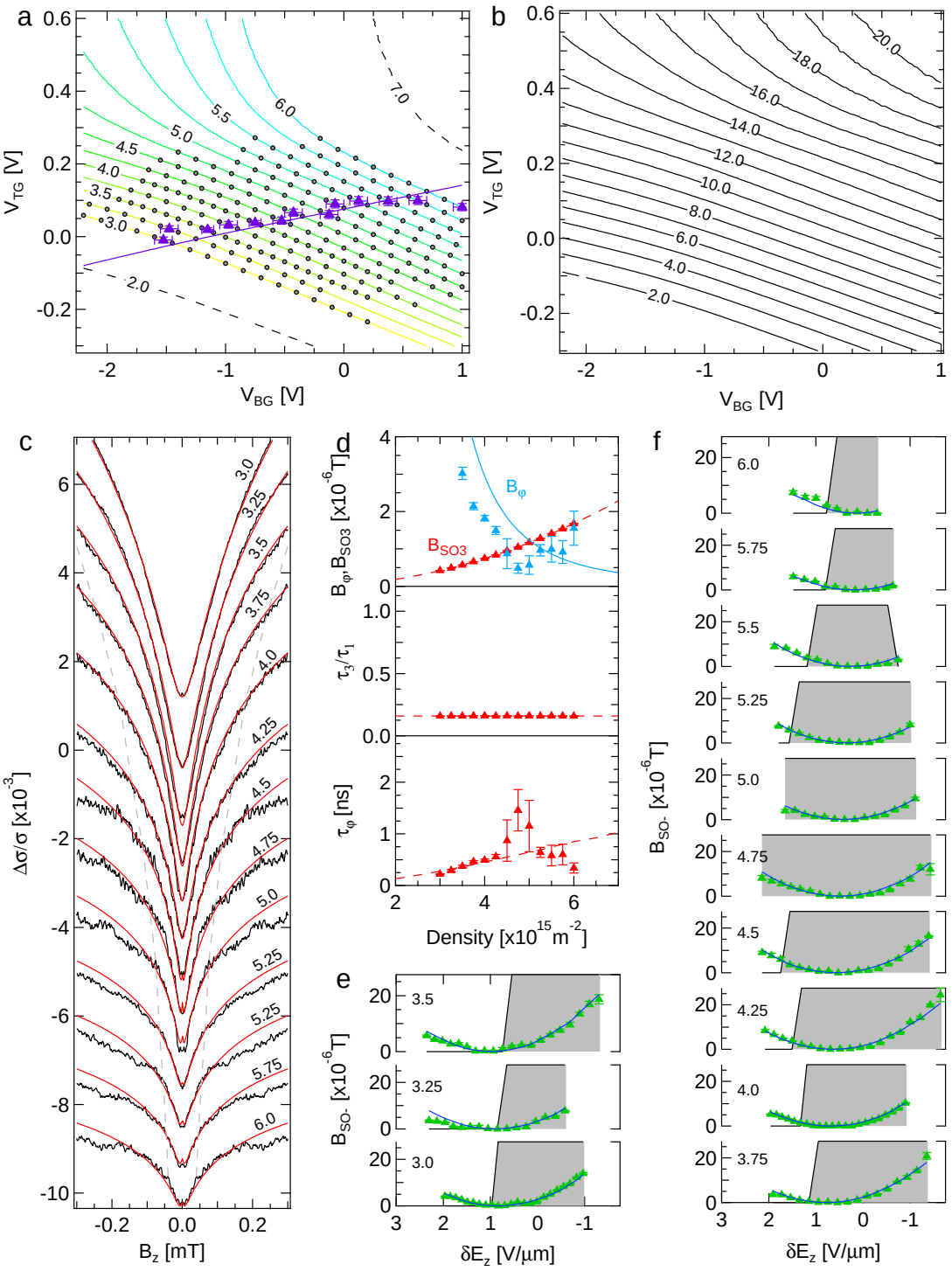

Figure 4.12: First measurement on sample III (9.3 nm quantum well, asymmetrically doped).

4.7.4 Details on evaluating B_{SO-} and B_{SO3}

Symmetry point determination and value of B_{SO3}

Here, we show how the value of B_{SO3} and the position of the symmetry point are determined from the WAL traces. The data presented is from measurement 3 at a density of $8.25 \times 10^{15}\,\mathrm{m}^{-2}$. Figure 4.13(a) shows the measured magnetoconductance traces along a contour of constant density. We can clearly see how the WAL peak gets smaller with more positive gate voltage and then starts to increase again. As described in the main text we fit the expression for the quantum corrections and extract an *effective* SO value called B^*_{SO3} for each gate configuration, which will have a minimum around $\alpha \approx \beta$, see Fig. 4.13(b), as the difference of between α and β should be very small and only the cubic term remains. To obtain a value of B_{SO3}, we perform fits to the WAL trace at the minimum and ± 1 trace from it, using Eq. (4.63), where $B_{\mathrm{SO}-}$ is set to zero, see Fig. 4.13(c)-(e). The final value for B_{SO3} and τ_φ is obtained by taking the average of the three respective values.

Validity of the theory

With the known values of B_{SO3} and τ_φ the value of B_{SO-} can be extracted from each WAL trace. Here we show all measured magnetoconductivity traces with their respective fits to the data of dataset 3. We can see that these fits give in general very good agreement within the allowed fit range, given by $B_{\mathrm{SO}-}, B_{\mathrm{SO3}} \ll B_{\mathrm{tr}}$ the gray dashed line in each graph corresponds to $B_\perp = 0.5 B_{\mathrm{tr}}$. For WAL traces measured at more positive back gate voltage, the fit no longer captures the full WAL trace, especially at low densities ($n = 7.5 - 8.25 \times 10^{15}\mathrm{m}^{-2}$), the extracted values of B_{SO-} from these curves are then disregarded. The respective traces are colored in gray.

The exclusion of the results from the fits to these traces also serves as a validity check of the new theory. Equation (4.63) is obtained in the limit of $B_{\mathrm{SO}-} \ll B_{SO+}$. Using the expressions for $B_{\mathrm{SO}\pm}$ we can rewrite the condition and obtain in terms of α and β:

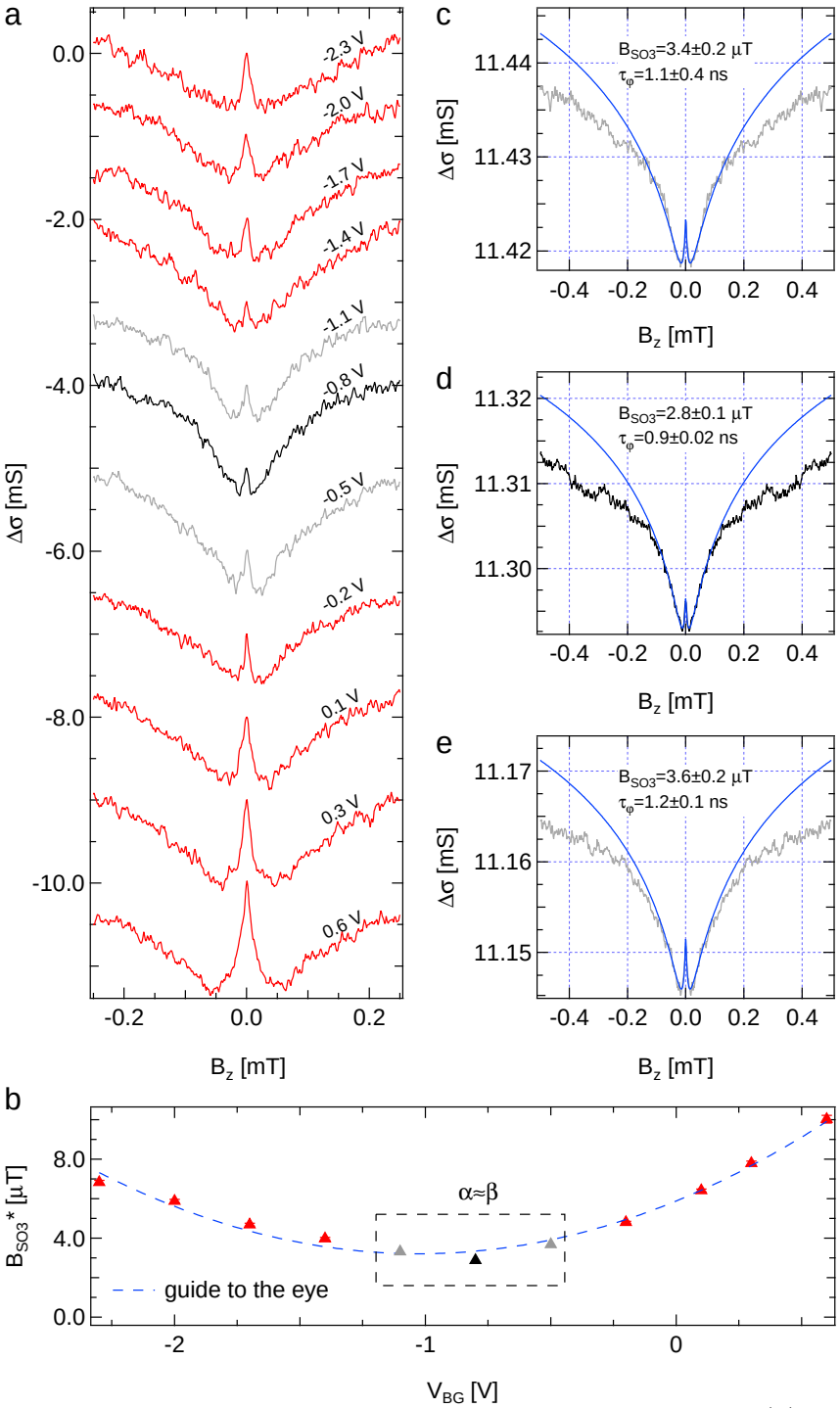

Figure 4.13: Determination of $\alpha \approx \beta$ for measurement 3. Panel (a) shows the WAL traces with their gate voltage indicated. In (b) the obtained values of B^*_{SO3} are shown as a function of back gate, showing a minimum at around -0.7 V. The blue dashed curve is a guide to the eye. Panels (c) to (e) show fits to the corresponding WAL traces around the minimum. The black trace is where the WAL peak is almost suppressed. This is the point, where $\alpha \approx \beta$.

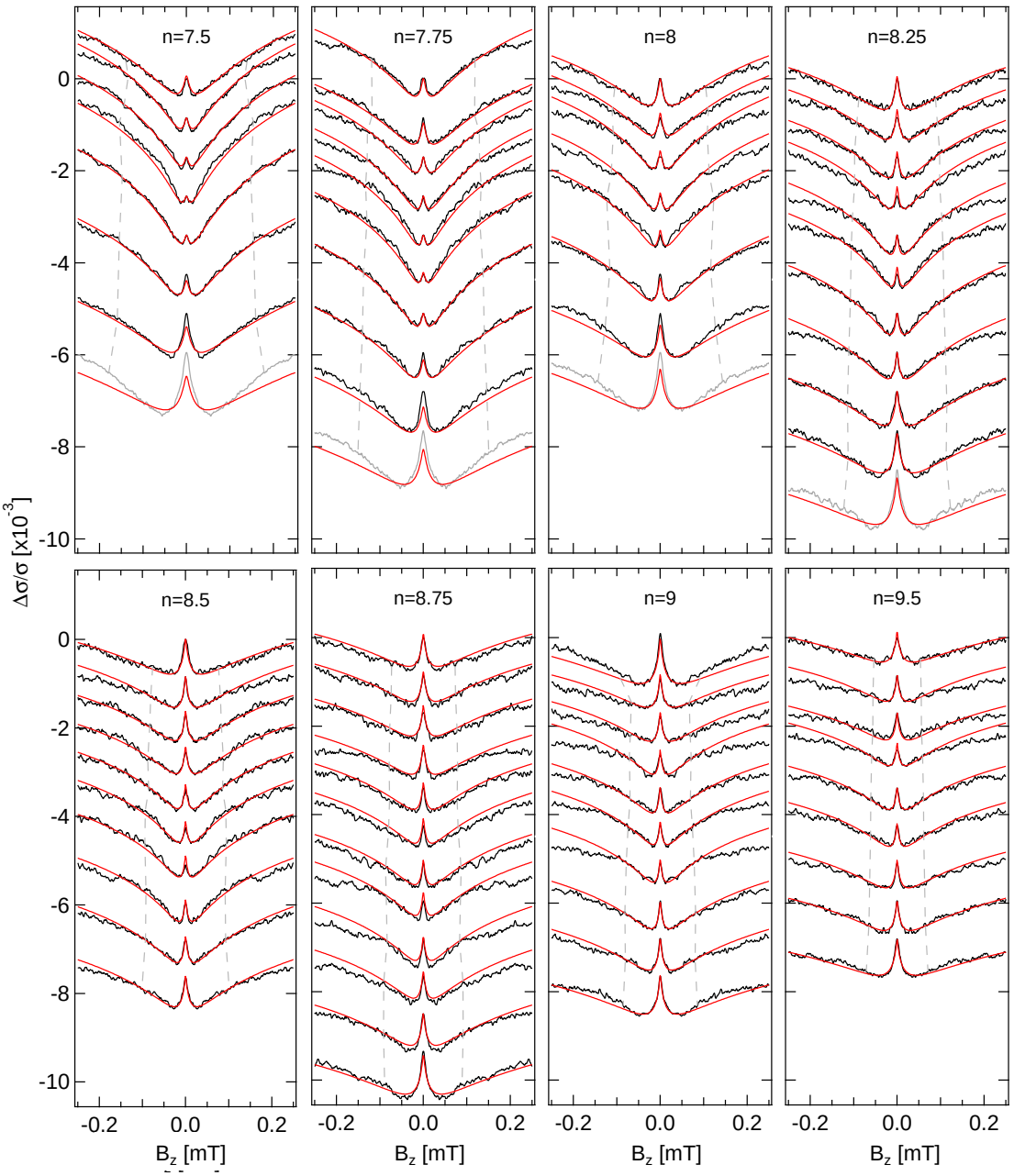

Figure 4.14: Fits to WAL traces with only B_{SO-} as a fit parameter for dataset 3. Each panel corresponds to one density and the magnetoconductivity traces are organized from top to bottom with increasing backgate voltage from negative to positive. The gray dashed line sets an upper bound to the allowed fit range for each individual trace, given by $B_\perp = 0.5B_{\mathrm{tr}}$

$$r \equiv \left| \frac{\alpha - \beta}{\alpha + \beta} \right| \ll 1, \tag{4.64}$$

which sets the range of the applicability of Eq. (4.63) of the main text. By setting $r \sim 0.4$, a validity range can be defined in terms of top and back gate voltages. This range has to be compared with the gate configurations measured and agrees well with the manually excluded gate configurations.

5 Conclusion and Outlook

In this thesis we have investigated the PSH in quantum transport measurements. We first identified the parameters that define the PSH state and allow to control its pitch. Contrary to previous experiments we explicitly included the cubic Dresselhaus term, which renormalizes the linear Dresselhaus term and makes it controllable with the density. This added an additional knob in experiments, which we realized in a GaAs QW, with a top and back gate. This allowed us to independently tune the Rashba and Dresselhaus SO parameters and introduce a new concept, the stretchable persistent spin helix. A concept that allows to vary the length λ_{PSH} (see Eq. (2.17)) while maintaining the PSH state. This enables coherent spin manipulations as well as transferring spin polarizations over distances of up to 25 μm and is only limited by the cubic Dresselhaus term, which can be tuned by density.

In the second part of this thesis we used explicitly the cubic Dresselhaus term to break the PSH symmetry in a controlled way. For this, we performed quantum transport measurements in a symmetrically doped QW, where the density is high and the cubic term can no longer be neglected. As in the previous experiment we employed the crossover from WAL to WL to detect the PSH, however WAL does not vanish completely at $\alpha = \beta$, due to the stronger cubic term. In the regime around the PSH symmetry, we derived a closed form expression for the quantum corrections to conductivity, which includes linear and cubic Dresselhaus terms, as well as the Rashba term, thereby solving an issue that has remained in the field for more than two decades. Employing this theory in the broken PSH regime allows us to systematically extract the Dresselhaus coefficient γ and Rashba parameter α. The obtained results are in excellent agreement with self-consistent simulations.

The observation of WAL at $\alpha = \beta$ is necessary to be able to apply a fit to the magneto-conductance data. In fact, we show that a reasonable value for B_{SO3} can only be obtained, if $B_{\mathrm{SO3}} > B_{\varphi}$. By going to even lower electron temperatures, which is $\sim 100\,\mathrm{mK}$ in the presented experiment, the coherence time τ_{φ} could be increased, allowing to observe WAL

at even lower densities and also allow a more precise determination of the PSH symmetry. As a result a more precise determination of the SO parameters becomes possible. Furthermore the ability to independently tune the Rashba and Dresselhaus parameters allows us to enter the regime, where $\alpha = 0$. Therein an analysis of the Dresselhaus parameter as a function of confinement would allow to shed more light onto the true value of the Dresselhaus coefficient and would explain if there is a dependence on the confinement, which has been observed in optical experiments [151, 168]. A deeper understanding and more precise values of the SO parameters facilitate work of research groups, designing and simulating custom tailored SO wafer materials.

One of the longstanding quests in the field of semiconductor spintronics is a working SFET beyond its functional demonstration [169, 170] to become a viable technology [171]. Independent control of SO coupling extends the toolbox for researchers in the field of spintronics. Coherent control of the spin polarization could allow to switch between parallel and anti-parallel alignment of spins, giving larger on-off ratios in an SFET.

Spin qubits in quantum dots are very promising contenders as the basic building block for future quantum computation technologies [145]. A long spin relaxation time T_1 and spin coherence time T_2 are crucial for coherent spin operations. While the T_2 depends on hyperfine interaction and can be prolonged with spin echo techniques, the spin relaxation is mediated by SO coupling at large external magnetic fields [172–174]. In fact the interplay of the Rashba and Dresselhaus SO coupling gives rise to an anisotropy in the spin relaxation time [175]. Top and back gated quantum dots with universally controllable SO coupling ultimately allow to tune into the regime of $\alpha = \beta$ and extend the spin relaxation time such that only the hyperfine interaction dominates.

In recent years InAs/GaSb double QWs have meet renewed interest due to the possibility of creating a topologically insulating state [143]. By applying an electric field or varying the QW thickness the InAs conduction band crosses with the valence band of GaSb and a hybridization gap at finite momentum opens. This results in helical edge modes, which would carry only one conductance quantum and can be detected with a four point

measurement [144]. Recent transport measurements on this kind of systems observed a fully SO polarized state [176]. Another work recently investigated SO parameters from transport measurements [177], extracting Rashba and Dresselhaus parameters. However, the obtained results are still preliminary and suggest a Dresselhaus coefficient $\gamma = 0$. Transport measurements in this regime were done so far by employing Shubnikov de-Haas measurements, which are still lacking a full theoretical description with all the SO parameters. Our model would allow to gain further insight into the SO coupling in this new material system.

Other recent proposals predict a persistent skyrmion lattice [178] in double GaAs QWs with two occupied sub bands resulting from two crossed persistent spin helices. This kind of system still remains to be demonstrated, but holds the potential to observe other topological phenomena in 2DEGs.

Bibliography

[1] K. v. Klitzing, G. Dorda, and M. Pepper. *New Method for High-Accuracy Determination of the Fine-Structure Constant Based on Quantized Hall Resistance*. Physical Review Letters **45**, 494 (1980).

[2] B. J. van Wees, H. van Houten, C. W. J. Beenakker, J. G. Williamson, L. P. Kouwenhoven, D. van der Marel, and C. T. Foxon. *Quantized conductance of point contacts in a two-dimensional electron gas*. Physical Review Letters **60**, 848 (1988).

[3] D. A. Wharam, T. J. Thornton, R. Newbury, M. Pepper, H. Ahmed, J. E. F. Frost, D. G. Hasko, D. C. Peacock, D. A. Ritchie, and G. A. C. Jones. *One-dimensional transport and the quantisation of the ballistic resistance*. Journal of Physics C: Solid State Physics **21**, L209 (1988).

[4] T. A. Fulton and G. J. Dolan. *Observation of single-electron charging effects in small tunnel junctions*. Physical Review Letters **59**, 109 (1987).

[5] J. H. F. Scott-Thomas, S. B. Field, M. A. Kastner, H. I. Smith, and D. A. Antoniadis. *Conductance Oscillations Periodic in the Density of a One-Dimensional Electron Gas*. Physical Review Letters **62**, 583 (1989).

[6] S. Tarucha, D. G. Austing, T. Honda, R. J. van der Hage, and L. P. Kouwenhoven. *Shell Filling and Spin Effects in a Few Electron Quantum Dot*. Physical Review Letters **77**, 3613 (1996).

[7] L. Gor'kov, A. Larkin, and D. Khmel'nitskii. *Particle conductivity in a two-dimensional random potential*. JETP Letters **30**, 228 (1979).

[8] Y. Kawaguchi and S. Kawaji. *Negative Magnetoresistance in Silicon (100) MOS Inversion Layers*. Journal of the Physical Society of Japan **48**, 699 (1980).

[9] S. Hikami, A. I. Larkin, and Y. Nagaoka. *Spin-Orbit Interaction and Magnetoresistance in the Two Dimensional Random System*. Progress of Theoretical Physics **63**, 707 (1980).

[10] G. Bergmann. *Influence of Spin-Orbit Coupling on Weak Localization*. Physical Review Letters **48**, 1046 (1982).

[11] W. Gerlach and O. Stern. *Der experimentelle Nachweis der Richtungsquantelung im Magnetfeld*. Zeitschrift für Physik **9**, 349 (1922).

[12] H. Welker. *Neue Halbleitende Verbindungen II*. Z. Naturforschg. **8a**, 248 (1953).

[13] G. Dresselhaus. *Spin-Orbit Coupling Effects in Zinc Blende Structures*. Physical Review **100**, 580 (1955).

[14] Y. Bychkov and E. Rashba. *Properties of a 2D electron gas with lifted spectral density*. JETP Letters **39**, 78 (1984).

[15] S. Datta and B. Das. *Electronic analog of the electro-optic modulator*. Applied Physics Letters **56**, 665 (1990).

[16] M. I. D'yakonov and V. I. Perel'. *Spin Orientation of Electrons Associated with the Interband Absorption of Light in Semiconductors.* JETP **33**, 1053 (1971).

[17] M. I. Dyakonov and V. I. Perel. *Current-induced spin orientation of electrons in semiconductors.* Physics Letters A **35**, 459 (1971).

[18] Y. K. Kato, R. C. Myers, A. C. Gossard, and D. D. Awschalom. *Observation of the Spin Hall Effect in Semiconductors.* Science **306**, 1910 (2004).

[19] B. A. Bernevig, T. L. Hughes, and S.-C. Zhang. *Quantum Spin Hall Effect and Topological Phase Transition in HgTe Quantum Wells.* Science **314**, 1757 (2006).

[20] Y. Oreg, G. Refael, and F. von Oppen. *Helical Liquids and Majorana Bound States in Quantum Wires.* Physical Review Letters **105**, 177002 (2010).

[21] R. M. Lutchyn, J. D. Sau, and S. Das Sarma. *Majorana Fermions and a Topological Phase Transition in Semiconductor-Superconductor Heterostructures.* Physical Review Letters **105**, 077001 (2010).

[22] D. Awschalom, N. Samarth, and D. Loss. *Semiconductor spintronics and quantum computation* (Springer, Berlin; London, 2011).

[23] J. Schliemann, J. C. Egues, and D. Loss. *Nonballistic Spin-Field-Effect Transistor.* Physical Review Letters **90**, 146801 (2003).

[24] B. A. Bernevig, J. Orenstein, and S.-C. Zhang. *Exact SU(2) Symmetry and Persistent Spin Helix in a Spin-Orbit Coupled System.* Physical Review Letters **97**, 236601 (2006).

[25] J. D. Koralek, C. P. Weber, J. Orenstein, B. A. Bernevig, S.-C. Zhang, S. Mack, and D. D. Awschalom. *Emergence of the persistent spin helix in semiconductor quantum wells.* Nature **458**, 610 (2009).

[26] M. P. Walser, C. Reichl, W. Wegscheider, and G. Salis. *Direct mapping of the formation of a persistent spin helix.* Nature Physics **8**, 757 (2012).

[27] K. C. Hall, W. H. Lau, K. Gündoğdu, M. E. Flatté, and T. F. Boggess. *Nonmagnetic semiconductor spin transistor.* Applied Physics Letters **83**, 2937 (2003).

[28] Y. Kunihashi, M. Kohda, H. Sanada, H. Gotoh, T. Sogawa, and J. Nitta. *Proposal of spin complementary field effect transistor.* Applied Physics Letters **100**, 113502 (2012).

[29] M. Kohda, V. Lechner, Y. Kunihashi, T. Dollinger, P. Olbrich, C. Schönhuber, I. Caspers, V. V. Bel'kov, L. E. Golub, D. Weiss, K. Richter, J. Nitta, and S. D. Ganichev. *Gate-controlled persistent spin helix state in (In,Ga)As quantum wells.* Physical Review B **86**, 081306 (2012).

[30] R. Dingle, H. L. Störmer, A. C. Gossard, and W. Wiegmann. *Electron mobilities in modulation-doped semiconductor heterojunction superlattices.* Applied Physics Letters **33**, 665 (1978).

[31] R. Willett, J. P. Eisenstein, H. L. Störmer, D. C. Tsui, A. C. Gossard, and J. H. English. *Observation of an even-denominator quantum number in the fractional quantum Hall effect.* Physical Review Letters **59**, 1776 (1987).

[32] B. L. Al'tshuler. *Fluctuations in the extrinsic conductivity of disordered conductors.* JETP Letters **41**, 648 (1985).

[33] P. A. Lee and A. D. Stone. *Universal Conductance Fluctuations in Metals.* Physical Review Letters **55**, 1622 (1985).

[34] M. Cahay, M. McLennan, and S. Datta. *Conductance of an array of elastic scatterers: A scattering-matrix approach.* Physical Review B **37**, 10125 (1988).

[35] R. P. Taylor, M. L. Leadbeater, G. P. Whittington, P. C. Main, L. Eaves, S. P. Beaumont, I. McIntyre, S. Thoms, and C. D. W. Wilkinson. *Universal conductance fluctuations in the magnetoresistance of submicron-size n^+-GaAs wires and laterally confined n^--GaAs/(AlGa)As heterostructures.* Surface Science **196**, 52 (1988).

[36] P. W. Anderson. *Absence of Diffusion in Certain Random Lattices.* Physical Review **109**, 1492 (1958).

[37] B. L. Al'tshuler and A. Aronov. *Electron-Electron Interaction In Disordered Conductors.* In *Modern Problems in Condensed Matter Sciences*, volume 10, 1–153 (Elsevier, 1985).

[38] J. J. Sakurai. *Advanced Quantum Mechanics.* Addison-Wesley series in advanced physics (Addison-Wesley, Reading, Mass., 1998).

[39] R. H. Parmenter. *Symmetry Properties of the Energy Bands of the Zinc Blende Structure.* Physical Review **100**, 573 (1955).

[40] P. Altmann, F. G. G. Hernandez, G. J. Ferreira, M. Kohda, C. Reichl, W. Wegscheider, and G. Salis. *Current-Controlled Spin Precession of Quasistationary Electrons in a Cubic Spin-Orbit Field.* Physical Review Letters **116**, 196802 (2016).

[41] T. Ando, A. B. Fowler, and F. Stern. *Electronic properties of two-dimensional systems.* Reviews of Modern Physics **54**, 437 (1982).

[42] W. Zawadzki and P. Pfeffer. *Spin splitting of subband energies due to inversion asymmetry in semiconductor heterostructures.* Semiconductor Science and Technology **19**, R1 (2004).

[43] R. Winkler. *Spin-Orbit Coupling Effects in Two-Dimensional Electron and Hole Systems* (Springer, 2003).

[44] J. Fabian, A. Matos-Abiague, C. Ertler, P. Stano, and I. Žutić. *Semiconductor Spintronics.* acta physica slovaca **57**, 565 (2007).

[45] W. Zawadzki and P. Pfeffer. *Average forces in bound and resonant quantum states.* Physical Review B **64**, 235313 (2001).

[46] R. Lassnig. ***k·p*** *theory, effective-mass approach, and spin splitting for two-dimensional electrons in GaAs-GaAlAs heterostructures.* Physical Review B **31**, 8076 (1985).

[47] U. Rössler and J. Kainz. *Microscopic interface asymmetry and spin-splitting of electron subbands in semiconductor quantum structures.* Solid State Communications **121**, 313 (2002).

[48] E. Y. Sherman. *Random spin-orbit coupling and spin relaxation in symmetric quantum wells.* Applied Physics Letters **82**, 209 (2003).

[49] J. R. Bindel, M. Pezzotta, J. Ulrich, M. Liebmann, E. Y. Sherman, and M. Morgenstern. *Probing variations of the Rashba spin-orbit coupling at the nanometre scale.* Nature Physics **12**, 920 (2016).

[50] F. G. Pikus and G. E. Pikus. *Conduction-band spin splitting and negative magnetoresistance in A3B5 heterostructures.* Physical Review B **51**, 16928 (1995).

[51] A. Sasaki, S. Nonaka, Y. Kunihashi, M. Kohda, T. Bauernfeind, T. Dollinger, K. Richter, and J. Nitta. *Direct determination of spin-orbit interaction coefficients and realization of the persistent spin helix symmetry.* Nature Nanotechnology **9**, 703 (2014).

[52] M. Scheid, M. Kohda, Y. Kunihashi, K. Richter, and J. Nitta. *All-Electrical Detection of the Relative Strength of Rashba and Dresselhaus Spin-Orbit Interaction in Quantum Wires.* Physical Review Letters **101**, 266401 (2008).

[53] I. Žutić, J. Fabian, and S. Das Sarma. *Spintronics: Fundamentals and applications.* Reviews of Modern Physics **76**, 323 (2004).

[54] R. J. Elliott. *Theory of the Effect of Spin-Orbit Coupling on Magnetic Resonance in Some Semiconductors.* Physical Review **96**, 266 (1954).

[55] Y. Yafet. *g Factors and Spin-Lattice Relaxation of Conduction Electrons.* Solid State Physics **14**, 1 (1963).

[56] M. D'yakonov, V. Marushchal, V. Perel', and A. Titkov. *The effect of strain on the spin relaxation of conduction electrons in III-V semiconductors.* JETP Letters **63**, 655 (1986).

[57] J. N. Chazalviel. *Spin Relaxation of Conduction Electrons in n-type InSb at Low Temperature.* Physical Review B **11**, 1555 (1975).

[58] F. Herling, C. Morrison, C. S. Knox, S. Zhang, O. Newell, M. Myronov, E. H. Linfield, and C. H. Marrows. *Spin-orbit Interaction in InAs/GaSb Heterostructures Quantified by Weak Antilocalization.* Physical Review B **95**, 155307 (2017).

[59] N. S. Averkiev and L. E. Golub. *Giant spin relaxation anisotropy in zinc-blende heterostructures.* Physical Review B **60**, 15582 (1999).

[60] N. S. Averkiev, L. E. Golub, and M. Willander. *Spin relaxation anisotropy in two-dimensional semiconductor systems.* Journal of Physics: Condensed Matter **14**, R271 (2002).

[61] G. L. Bir, A. G. Aronov, and G. E. Pikus. *Spin relaxation of electrons due to scattering by holes.* JETP **42**, 705 (1975).

[62] A. W. Overhauser. *Paramagnetic Relaxation in Metals.* Physical Review **89**, 689 (1953).

[63] J. J. Krich and B. I. Halperin. *Cubic Dresselhaus Spin-Orbit Coupling in 2D Electron Quantum Dots.* Physical Review Letters **98**, 226802 (2007).

[64] J. Nitta, T. Akazaki, H. Takayanagi, and T. Enoki. *Gate Control of Spin-Orbit Interaction in an Inverted* $In_{0.53}Ga_{0.47}As/In_{0.52}Al_{0.48}As$ *Heterostructure.* Physical Review Letters **78**, 1335 (1997).

[65] G. Engels, J. Lange, T. Schäpers, and H. Lüth. *Experimental and theoretical approach to spin splitting in modulation-doped* $In_xGa_{(1-x)}As/InP$ *quantum wells for* $B \to 0$. Physical Review B **55**, R1958 (1997).

[66] D. Grundler. *Large Rashba Splitting in InAs Quantum Wells due to Electron Wave Function Penetration into the Barrier Layers.* Physical Review Letters **84**, 6074 (2000).

[67] R. S. Calsaverini, E. Bernardes, J. C. Egues, and D. Loss. *Intersubband-induced spin-orbit interaction in quantum wells.* Physical Review B **78**, 155313 (2008).

[68] V. K. Kalevich and V. Korenev. *Effect of electric field on the optical orientation of 2D electrons.* JETP Letters **52**, 230 (1990).

[69] L. Meier, G. Salis, I. Shorubalko, E. Gini, S. Schön, and K. Ensslin. *Measurement of Rashba and Dresselhaus Spin-Orbit Magnetic Fields.* Nature Physics **3**, 650 (2007).

[70] Y. Kunihashi, H. Sanada, H. Gotoh, K. Onomitsu, M. Kohda, J. Nitta, and T. Sogawa. *Drift transport of helical spin coherence with tailored spin-orbit interactions.* Nature Communications **7**, 10722 (2016).

[71] E. Abrahams, P. W. Anderson, D. C. Licciardello, and T. V. Ramakrishnan. *Scaling Theory of Localization: Absence of Quantum Diffusion in Two Dimensions.* Physical Review Letters **42**, 673 (1979).

[72] G. Bergmann. *Weak localization in thin films: a time-of-flight experiment with conduction electrons.* Physics Reports **107**, 1 (1984).

[73] J. Rammer. *Quantum Transport Theory.* Number 99 in Frontiers in Physics (Perseus Books, 1998).

[74] G. J. Dolan and D. D. Osheroff. *Nonmetallic Conduction in Thin Metal Films at Low Temperatures.* Physical Review Letters **43**, 721 (1979).

[75] D. J. Bishop, D. C. Tsui, and R. C. Dynes. *Nonmetallic Conduction in Electron Inversion Layers at Low Temperatures.* Physical Review Letters **44**, 1153 (1980).

[76] D. A. Poole, M. Pepper, and A. Hughes. *Spin-orbit coupling and weak localisation in the 2D inversion layer of indium phosphide.* Journal of Physics C: Solid State Physics **15**, L1137 (1982).

[77] S. Kawaji, K. Kuboki, T. Nambu, J. Wakabayashi, J. Yoshino, and H. Sakaki. *Inelastic Scattering and Spin-Orbit Scattering in 2D Systems Of GaAs/AlGaAs Heterostructures.* In *Proceedings of the 17th International Conference on the Physics of Semiconductors*, 413 (Springer-Verlag New York 1985, San Francisco, California, 1984).

[78] G. E. Pikus and A. N. Titkov. *Spin Relaxation under Optical Orientation in Semiconductors.* Modern Problems in Condensed Matter Sciences **8**, 73 (1984).

[79] B. L. Al'tshuler, A. G. Aronov, A. I. Larkin, and D. E. Khmel'nitskii. *Anomalous magnetoresistance in semiconductors.* Journal of Experimental and Theoretical Physics **54**, 411 (1981).

[80] S. Iordanskii, Y. Lyanda-Geller, and G. Pikus. *Weak Localization in Quantum Wells with Spin-Orbit Interaction.* JETP Letters **60**, 199 (1994).

[81] S. Maekawa and H. Fukuyama. *Magnetoresistance in Two-Dimensional Disordered Systems: Effects of Zeeman Splitting and Spin-Orbit Scattering.* Journal of the Physical Society of Japan **50**, 2516 (1981).

[82] F. Komori, S.-i. Kobayashi, Y. Ootuka, and W. Sasaki. *Experimental Study of Electron Localization in a Two-Dimensional Metal.* Journal of the Physical Society of Japan **50**, 1051 (1981).

[83] N. S. Averkiev, L. E. Golub, and G. E. Pikus. *Weak localization in semiconductor structures with strong spin-orbit coupling.* Journal of Experimental and Theoretical Physics **86**, 780 (1998).

[84] N. S. Averkiev, L. E. Golub, and G. E. Pikus. *Weak localization in p-type quantum wells.* Semiconductors **32**, 1087 (1998).

[85] N. S. Averkiev, L. E. Golub, S. A. Tarasenko, and M. Willander. *Effect of intersubband scattering on weak localization in two-dimensional systems.* Physical Review B **64**, 045405 (2001).

[86] A. Punnoose. *Magnetoconductivity in the Presence of Bychkov-Rashba Spin-Orbit Interaction.* Applied Physics Letters **88**, 252113 (2006).

[87] K. K. Choi, D. C. Tsui, and K. Alavi. *Dephasing Time and One-Dimensional Localization of Two-Dimensional Electrons in GaAs/$Al_xGa_{1-x}As$ Heterostructures.* Physical Review B **36**, 7751 (1987).

[88] R.-P. Klett, J. Schönle, A. Becker, D. Dyck, K. Rott, J. Haskenhoff, J. Krieft, T. Hübner, O. Reimer, C. Shekhar, J.-M. Schmalhorst, A. Hütten, C. Felser, W. Wernsdorfer, and G. Reiss. *Proximity-induced Superconductivity and Quantum Interference in Topological Crystalline Insulator SnTe Thin Film Devices.* arXiv:1706.10164 [cond-mat] (2017).

[89] P. D. Dresselhaus, C. M. A. Papavassiliou, R. G. Wheeler, and R. N. Sacks. *Observation of spin precession in GaAs inversion layers using antilocalization.* Physical Review Letters **68**, 106 (1992).

[90] J. E. Hansen, R. Taboryski, and P. E. Lindelof. *Weak localization in a GaAs heterostructure close to population of the second subband.* Physical Review B **47**, 16040 (1993).

[91] T. Hassenkam, S. Pedersen, K. Baklanov, A. Kristensen, C. B. Sorensen, P. E. Lindelof, F. G. Pikus, and G. E. Pikus. *Spin splitting and weak localization in (110) $GaAs/Al_xGa_{1-x}As$ quantum wells.* Physical Review B **55**, 9298 (1997).

[92] T. Koga, J. Nitta, T. Akazaki, and H. Takayanagi. *Rashba Spin-Orbit Coupling Probed by the Weak Antilocalization Analysis in $InAlAs/InGaAs/InAlAs$ Quantum Wells as a Function of Quantum Well Asymmetry.* Physical Review Letters **89**, 046801 (2002).

[93] W. Knap, C. Skierbiszewski, A. Zduniak, E. Litwin-Staszewska, D. Bertho, F. Kobbi, J. L. Robert, G. E. Pikus, F. G. Pikus, S. V. Iordanskii, V. Mosser, K. Zekentes, and Y. B. Lyanda-Geller. *Weak antilocalization and spin precession in quantum wells.* Physical Review B **53**, 3912 (1996).

[94] S. Pedersen, C. B. Sørensen, A. Kristensen, P. E. Lindelof, L. E. Golub, and N. S. Averkiev. *Weak Localization in $Al_{0.5}Ga_{0.5}As/GaAs$ p-type Quantum Wells.* Physical Review B **60**, 4880 (1999).

[95] A. Kawabata. *On the Field Dependence of Magnetoresistance in Two-Dimensional Systems.* Journal of the Physical Society of Japan **53**, 3540 (1984).

[96] A. Kawabata. *Theory of Negative Magnetoresistance I. Application to Heavily Doped Semiconductors.* Journal of the Physical Society of Japan **49**, 628 (1980).

[97] H.-P. Wittmann and A. Schmid. *Anomalous Magnetoconductance Beyond the Diffusion Limit.* Journal of Low Temperature Physics **69**, 131 (1987).

[98] M. Dyakonov. *Magnetoconductance due to Weak Localization Beyond the Diffusion Approximation: The High-Field Limit.* Solid State Communications **92**, 711 (1994).

[99] A. Zduniak, M. I. Dyakonov, and W. Knap. *Universal behavior of magnetoconductance due to weak localization in two dimensions.* Physical Review B **56**, 1996 (1997).

[100] A. P. Dmitriev, V. Y. Kachorovskii, and I. V. Gornyi. *Nonbackscattering Contribution to Weak Localization.* Physical Review B **56**, 9910 (1997).

[101] J. B. Miller, D. M. Zumbühl, C. M. Marcus, Y. B. Lyanda-Geller, D. Goldhaber-Gordon, K. Campman, and A. C. Gossard. *Gate-Controlled Spin-Orbit Quantum Interference Effects in Lateral Transport.* Physical Review Letters **90**, 076807 (2003).

[102] Y. Lyanda-Geller. *Quantum Interference and Electron-Electron Interactions at Strong Spin-Orbit Coupling in Disordered Systems.* Physical Review Letters **80**, 4273 (1998).

[103] L. E. Golub. *Weak antilocalization in high-mobility two-dimensional systems.* Physical Review B **71**, 235310 (2005).

[104] M. M. Glazov and L. E. Golub. *Nondiffusive Weak Localization in Two-Dimensional Systems with Spin-Orbit Splitting of the Spectrum.* Semiconductors **40**, 1209 (2006).

[105] F. V. Porubaev and L. E. Golub. *Weak Localization in Low-Symmetry Quantum Wells.* Physical Review B **90**, 085314 (2014).

[106] A. Sawada and T. Koga. *Universal Modeling of Weak Antilocalization Corrections in Quasi-Two-Dimensional Electron Systems using Predetermined Return Orbitals.* Physical Review E **95**, 023309 (2017).

[107] S. A. Studenikin, P. T. Coleridge, G. Yu, and P. J. Poole. *Electron Spin-Orbit Splitting in a InGaAs/InP Quantum Well Studied by Means of the Weak-Antilocalization and Spin-Zero Effects in Tilted Magnetic Fields.* Semiconductor Science and Technology **20**, 1103 (2005).

[108] V. A. Guzenko, T. Schäpers, and H. Hardtdegen. *Weak antilocalization in high mobility $Ga_xAs_{1-x}As/InP$ two-dimensional electron gases with strong spin-orbit coupling.* Physical Review B **76**, 165301 (2007).

[109] Y. M. Zhou, G. Yu, L. M. Wei, K. H. Gao, W. Z. Zhou, T. Lin, L. Y. Shang, S. L. Guo, J. H. Chu, N. Dai, and D. G. Austing. *Experimental Approaches to Zero-Field Spin Splitting in a Gated High-Mobility $In_{0.53}Ga_{0.47}As/InP$ Quantum Well Structure: Weak Antilocalization and Beating Pattern.* Journal of Applied Physics **107**, 053708 (2010).

[110] D. Spirito, L. Di Gaspare, F. Evangelisti, A. Di Gaspare, E. Giovine, and A. Notargiacomo. *Weak antilocalization and spin-orbit interaction in a two-dimensional electron gas.* Physical Review B **85**, 235314 (2012).

[111] J. Sinova, S. O. Valenzuela, J. Wunderlich, C. H. Back, and T. Jungwirth. *Spin Hall effects.* Reviews of Modern Physics **87**, 1213 (2015).

[112] V. Mourik, K. Zuo, S. M. Frolov, S. R. Plissard, E. P. a. M. Bakkers, and L. P. Kouwenhoven. *Signatures of Majorana Fermions in Hybrid Superconductor-Semiconductor Nanowire Devices.* Science **336**, 1003 (2012).

[113] X. Wan, A. M. Turner, A. Vishwanath, and S. Y. Savrasov. *Topological semimetal and Fermi-arc surface states in the electronic structure of pyrochlore iridates.* Physical Review B **83**, 205101 (2011).

[114] P. Chuang, S.-C. Ho, L. W. Smith, F. Sfigakis, M. Pepper, C.-H. Chen, J.-C. Fan, J. P. Griffiths, I. Farrer, H. E. Beere, G. a. C. Jones, D. A. Ritchie, and T.-M. Chen. *All-electric all-semiconductor spin field-effect transistors.* Nature Nanotechnology **10**, 35 (2015).

[115] H. Sanada, Y. Kunihashi, H. Gotoh, K. Onomitsu, M. Kohda, J. Nitta, P. V. Santos, and T. Sogawa. *Manipulation of mobile spin coherence using magnetic-field-free electron spin resonance.* Nature Physics **9**, 280 (2013).

[116] S. J. Papadakis, E. P. D. Poortere, H. C. Manoharan, M. Shayegan, and R. Winkler. *The Effect of Spin Splitting on the Metallic Behavior of a Two-Dimensional System.* Science **283**, 2056 (1999).

[117] M. M. Glazov and E. Y. Sherman. *Nonexponential spin relaxation in magnetic fields in quantum wells with random spin-orbit coupling.* Physical Review B **71**, 241312 (2005).

[118] E. Y. Sherman and J. Sinova. *Physical limits of the ballistic and nonballistic spin-field-effect transistor: Spin dynamics in remote-doped structures.* Physical Review B **72**, 075318 (2005).

[119] J. Luo, H. Munekata, F. F. Fang, and P. J. Stiles. *Effects of inversion asymmetry on electron energy band structures in GaSb/InAs/GaSb quantum wells.* Physical Review B **41**, 7685 (1990).

[120] W. Wang and J. Y. Fu. *Temperature dependence of the Rashba and Dresselhaus spin-orbit interactions in GaAs wells.* Physica B: Condensed Matter **482**, 14 (2016).

[121] M. P. Walser, U. Siegenthaler, V. Lechner, D. Schuh, S. D. Ganichev, W. Wegscheider, and G. Salis. *Dependence of the Dresselhaus spin-orbit interaction on the quantum well width.* Physical Review B **86**, 195309 (2012).

[122] K. Yoshizumi, A. Sasaki, M. Kohda, and J. Nitta. *Gate-controlled switching between persistent and inverse persistent spin helix states.* Applied Physics Letters **108**, 132402 (2016).

[123] J. Fu and J. C. Egues. *Spin-orbit interaction in GaAs wells: From one to two subbands.* Physical Review B **91**, 075408 (2015).

[124] K. D. Maranowski, J. P. Ibbetson, K. L. Campman, and A. C. Gossard. *Interface between low-temperature grown GaAs and undoped GaAs as a conduction barrier for back gates.* Applied Physics Letters **66**, 3459 (1995).

[125] J.-M. Jancu, R. Scholz, E. de Andrada e Silva, and G. La Rocca. *Atomistic spin-orbit coupling and k.p parameters in III-V semiconductors.* Physical Review B **72** (2005).

[126] W. Yi, V. Narayanamurti, H. Lu, M. A. Scarpulla, A. C. Gossard, Y. Huang, J.-H. Ryou, and R. D. Dupuis. *Bandgap and band offsets determination of semiconductor heterostructures using three-terminal ballistic carrier spectroscopy.* Applied Physics Letters **95**, 112102 (2009).

[127] I. Vurgaftman, J. R. Meyer, and L. R. Ram-Mohan. *Band parameters for III-V compound semiconductors and their alloys.* Journal of Applied Physics **89**, 5815 (2001).

[128] H. Mayer and U. Rössler. *Spin splitting and anisotropy of cyclotron resonance in the conduction band of GaAs.* Physical Review B **44**, 9048 (1991).

[129] The split-off hole offset is written as, $\delta_\Delta = \Delta_b + \delta_v - \Delta_w$. Based on the parameters listed in Table 3, we have, δ_Δ=(0.3287±0.006) eV + (0.171 ± 0.003) eV - (0.341 ± 0.001) eV = (0.1587 ± 0.01) eV.

[130] C. Hermann and C. Weisbuch. $\vec{k} \cdot \vec{p}$ *pertubation theory in III-V compounds and alloys: a reexamination.* Physical Review B **15**, 823 (1977).

[131] M. Cardona, N. E. Christensen, and G. Fasol. *Relativistic band structure and spin-orbit splitting of zinc-blende-type semiconductors.* Physical Review B **38**, 1806 (1988).

[132] M. M. Glazov, E. Y. Sherman, and V. K. Dugaev. *Two-dimensional electron gas with spin-orbit coupling disorder.* Physica E: Low-dimensional Systems and Nanostructures **42**, 2157 (2010).

[133] Here γ_b is expected to be smaller than γ_w, due to a larger band gap in the barrier ($Al_{0.3}Ga_{0.7}As$) layer than that in the well (GaAs) layer.

[134] In our self-consistent calculation, we take m(GaAs)=$0.067m_0$ and $m(Al_{0.3}Ga_{0.7}As)$=$0.092m_0$, where $m(Al_{0.3}Ga_{0.7}As)$ is obtained from a linear interpolation of the GaAs and AlAl values with m(AlAs)=$0.15m_0$[43] and m_0 is the bare electron mass.

[135] J. Nitta. *Spin-orbit coupling: Ready for a close-up.* Nature Physics **12**, 898 (2016).

[136] M. M. Glazov and L. E. Golub. *Spin-orbit interaction and weak localization in heterostructures.* Semiconductor Science and Technology **24**, 064007 (2009).

[137] F. Reif. *Fundamentals of Statistical and Thermal Physics.* McGraw-Hill series in fundamentals of physics (McGraw-Hill, Tokyo, 1965).

[138] B. Das, D. C. Miller, S. Datta, R. Reifenberger, W. P. Hong, P. K. Bhattacharya, J. Singh, and M. Jaffe. *Evidence for spin splitting in* $In_xGa_{1-x}As/In_{0.52}Al_{0.48}As$ *heterostructures as* $B \to 0$. Physical Review B **39**, 1411 (1989).

[139] J. Schliemann. *Colloquium: Persistent Spin Textures in Semiconductor Nanostructures.* Reviews of Modern Physics **89**, 011001 (2017).

[140] M. Kohda and G. Salis. *Physics and Application of Persistent Spin Helix State in Semiconductor Heterostructures.* Semiconductor Science and Technology **32**, 073002 (2017).

[141] J. Sinova, D. Culcer, Q. Niu, N. A. Sinitsyn, T. Jungwirth, and A. H. MacDonald. *Universal Intrinsic Spin Hall Effect.* Physical Review Letters **92**, 126603 (2004).

[142] M. König, S. Wiedmann, C. Brüne, A. Roth, H. Buhmann, L. W. Molenkamp, X.-L. Qi, and S.-C. Zhang. *Quantum Spin Hall Insulator State in HgTe Quantum Wells.* Science **318**, 766 (2007).

[143] C. Liu, T. L. Hughes, X.-L. Qi, K. Wang, and S.-C. Zhang. *Quantum Spin Hall Effect in Inverted Type-II Semiconductors.* Physical Review Letters **100**, 236601 (2008).

[144] I. Knez, R.-R. Du, and G. Sullivan. *Evidence for Helical Edge Modes in Inverted InAs /GaSb Quantum Wells.* Physical Review Letters **107**, 136603 (2011).

[145] D. Loss and D. P. DiVincenzo. *Quantum computation with quantum dots.* Physical Review A **57**, 120 (1998).

[146] R. Hanson, L. P. Kouwenhoven, J. R. Petta, S. Tarucha, and L. M. K. Vandersypen. *Spins in few-electron quantum dots.* Reviews of Modern Physics **79**, 1217 (2007).

[147] C. Kloeffel and D. Loss. *Prospects for Spin-Based Quantum Computing in Quantum Dots.* Annual Review of Condensed Matter Physics **4**, 51 (2013).

[148] F. Dettwiler, J. Fu, S. Mack, P. J. Weigele, J. C. Egues, D. D. Awschalom, and D. M. Zumbühl. *Stretchable Persistent Spin Helices in GaAs Quantum Wells.* Physical Review X **7**, 031010 (2017).

[149] Y. Kato, R. C. Myers, A. C. Gossard, and D. D. Awschalom. *Coherent spin manipulation without magnetic fields in strained semiconductors.* Nature **427**, 50 (2004).

[150] M. Studer, G. Salis, K. Ensslin, D. C. Driscoll, and A. C. Gossard. *Gate-Controlled Spin-Orbit Interaction in a Parabolic GaAs/AlGaAs Quantum Well.* Physical Review Letters **103**, 027201 (2009).

[151] P. S. Eldridge, J. Hübner, S. Oertel, R. T. Harley, M. Henini, and M. Oestreich. *Spin-orbit fields in asymmetric (001)-oriented GaAs/$Al_xGa_{1-x}As$ quantum wells.* Physical Review B **83**, 041301 (2011).

[152] J. Ishihara, Y. Ohno, and H. Ohno. *Direct imaging of gate-controlled persistent spin helix state in a modulation-doped GaAs/AlGaAs quantum well.* Applied Physics Express **7**, 013001 (2013).

[153] B. L. Al'tshuler, D. Khmel'nitzkii, A. I. Larkin, and P. A. Lee. *Magnetoresistance and Hall effect in a disordered two-dimensional electron gas.* Physical Review B **22**, 5142 (1980).

[154] D. J. English, J. Hübner, P. S. Eldridge, D. Taylor, M. Henini, R. T. Harley, and M. Oestreich. *Effect of symmetry reduction on the spin dynamics of (001)-oriented GaAs quantum wells.* Physical Review B **87**, 075304 (2013).

[155] S. Das Sarma and F. Stern. *Single-particle relaxation time versus scattering time in an impure electron gas.* Physical Review B **32**, 8442 (1985).

[156] P. T. Coleridge. *Small-angle scattering in two-dimensional electron gases.* Physical Review B **44**, 3793 (1991).

[157] D. Zumbühl, J. Miller, C. Marcus, K. Campman, and A. Gossard. *Spin-Orbit Coupling, Antilocalization, and Parallel Magnetic Fields in Quantum Dots.* Physical Review Letters **89** (2002).

[158] D. Zumbühl, J. Miller, C. Marcus, V. Fal'ko, T. Jungwirth, and J. Harris. *Orbital effects of in-plane magnetic fields probed by mesoscopic conductance fluctuations.* Physical Review B **69** (2004).

[159] D. M. Zumbühl, J. B. Miller, C. M. Marcus, D. Goldhaber-Gordon, J. S. Harris, K. Campman, and A. C. Gossard. *Conductance Fluctuations and Partially Broken Spin Symmetries in Quantum Dots.* Physical Review B **72**, 081305 (2005).

[160] L. Casparis, M. Meschke, D. Maradan, A. C. Clark, C. P. Scheller, K. K. Schwarzwälder, J. P. Pekola, and D. M. Zumbühl. *Metallic Coulomb blockade thermometry down to 10 mK and below.* Review of Scientific Instruments **83**, 083903 (2012).

[161] D. Maradan, L. Casparis, T.-M. Liu, D. E. F. Biesinger, C. P. Scheller, D. M. Zumbühl, J. D. Zimmerman, and A. C. Gossard. *GaAs Quantum Dot Thermometry Using Direct Transport and Charge Sensing.* Journal of Low Temperature Physics **175**, 784 (2014).

[162] A. G. Huibers, M. Switkes, C. M. Marcus, K. Campman, and A. C. Gossard. *Dephasing in Open Quantum Dots.* Physical Review Letters **81**, 200 (1998).

[163] A. G. Huibers, J. A. Folk, S. R. Patel, C. M. Marcus, C. I. Duruöz, and J. S. Harris. *Low-Temperature Saturation of the Dephasing Time and Effects of Microwave Radiation on Open Quantum Dots.* Physical Review Letters **83**, 5090 (1999).

[164] S. Faniel, T. Matsuura, S. Mineshige, Y. Sekine, and T. Koga. *Determination of spin-orbit coefficients in semiconductor quantum wells.* Physical Review B **83**, 115309 (2011).

[165] A. N. Chantis, M. van Schilfgaarde, and T. Kotani. *Ab Initio.* Physical Review Letters **96**, 086405 (2006).

[166] M. Gmitra and J. Fabian. *First-principles studies of orbital and spin-orbit properties of GaAs, GaSb, InAs, and InSb zinc-blende and wurtzite semiconductors.* Physical Review B **94**, 165202 (2016).

[167] D. C. Marinescu. *Cubic Dresselhaus interaction parameter from quantum corrections to the conductivity in the presence of an in-plane magnetic field.* Physical Review B **96**, 115109 (2017).

[168] W. J. H. Leyland, R. T. Harley, M. Henini, A. J. Shields, I. Farrer, and D. A. Ritchie. *Oscillatory Dyakonov-Perel spin dynamics in two-dimensional electron gases.* Physical Review B **76**, 195305 (2007).

[169] H. C. Koo, J. H. Kwon, J. Eom, J. Chang, S. H. Han, and M. Johnson. *Control of Spin Precession in a Spin-Injected Field Effect Transistor.* Science **325**, 1515 (2009).

[170] J. Wunderlich, B.-G. Park, A. C. Irvine, L. P. Zârbo, E. Rozkotová, P. Nemec, V. Novák, J. Sinova, and T. Jungwirth. *Spin Hall Effect Transistor.* Science **330**, 1801 (2010).

[171] D. D. Awschalom and M. E. Flatté. *Challenges for semiconductor spintronics.* Nature Physics **3**, 153 (2007).

[172] V. N. Golovach, A. Khaetskii, and D. Loss. *Phonon-Induced Decay of the Electron Spin in Quantum Dots.* Physical Review Letters **93**, 016601 (2004).

[173] P. Stano and J. Fabian. *Orbital and spin relaxation in single and coupled quantum dots.* Physical Review B **74**, 045320 (2006).

[174] S. Amasha, K. MacLean, I. P. Radu, D. M. Zumbühl, M. A. Kastner, M. P. Hanson, and A. C. Gossard. *Electrical Control of Spin Relaxation in a Quantum Dot.* Physical Review Letters **100**, 046803 (2008).

[175] P. Scarlino, E. Kawakami, P. Stano, M. Shafiei, C. Reichl, W. Wegscheider, and L. M. K. Vandersypen. *Spin-Relaxation Anisotropy in a GaAs Quantum Dot.* Physical Review Letters **113**, 256802 (2014).

[176] F. Nichele, M. Kjaergaard, H. J. Suominen, R. Skolasinski, M. Wimmer, B.-M. Nguyen, A. A. Kiselev, W. Yi, M. Sokolich, M. J. Manfra, F. Qu, A. J. A. Beukman, L. P. Kouwenhoven, and C. M. Marcus. *Giant Spin-Orbit Splitting in Inverted InAs/GaSb Double Quantum Wells.* Physical Review Letters **118**, 016801 (2017).

[177] A. J. A. Beukman, F. K. de Vries, J. van Veen, R. Skolasinski, M. Wimmer, F. Qu, D. T. de Vries, B.-M. Nguyen, W. Yi, A. A. Kiselev, M. Sokolich, M. J. Manfra, F. Nichele, C. M. Marcus, and L. P. Kouwenhoven. *Spin-orbit interaction in a dual gated InAs/GaSb quantum well.* arXiv:1704.03482 [cond-mat] (2017).

[178] J. Fu, P. H. Penteado, M. O. Hachiya, D. Loss, and J. C. Egues. *Persistent Skyrmion Lattice of Noninteracting Electrons with Spin-Orbit Coupling.* Physical Review Letters **117**, 226401 (2016).

Curriculum Vitae

Pirmin Weigele, Germany

2005	Abitur, Pestalozzi Gymnasium, Biberach an der Riss
2005 - 2006	Civil service
2006	Master and Bachelor studies of Physics at Swiss Federal Institute of Technology (ETH), Zürich
Sept. 2011 - Apr. 2012	Semester project & master thesis at IBM Research, Rüschlikon
Apr. 2012 - Jun. 2012	Temporary research employee at IBM Research, Rüschlikon
Sept. 2012 - Jan. 2013	Intern at Sensirion AG, Stäfa
Mar. 2013 - Oct. 2017	PhD at University of Basel

Publications

- Martin Friedl, Kris Cerveny, Pirmin Weigele, Gözde Tütüncüoğlu, Sara Martí-Sánchez, Chunyi Huang, Taras Patlatiuk, Heidi Potts, Zhiyuan Sun, Megan Olivia Hill, Vladimir G. Dubrovskii, Jordi Arbiol, Lincoln J. Lauhon, Dominik Zumbühl, Anna Fontcuberta i Morral, *Template-Assisted Nanowire Networks Pointing to Scalable Topological Quantum Computing Schemes*, in preparation for publication.

- Pirmin J. Weigele*, D. C. Marinescu*, Florian Dettwiler, Jiyong Fu, Shawn Mack, J. Carlos Egues, David D. Awschalom and Dominik M. Zumbühl, *Symmetry Breaking of the Persistent Spin Helix in Quantum Transport*, submitted to Physical Review X

- Florian Dettwiler, Jiyong Fu, Shawn Mack, Pirmin J. Weigele, J. Carlos Egues, David D. Awschalom and Dominik M. Zumbühl, *Stretchable Persistent Spin Helices in GaAs Quantum Wells*, PRX **7**, 031010 (2017)

- C. Rossel, P. Weigele, L. Czornomaz, N. Daix, D. Caimi, M. Sousa, J. Fompeyrine, *Strain Effects on n-InGaAs Heterostructure-On-Insulator Made by Direct Wafer Bonding*, Solid-State Electronics **98**, 88 (2014)